Department of Physics and Astronomy

University of Heidelberg

Master Thesis

in Physics

submitted by

Alexander Magunia,

born in Recklinghausen

December 20th, 2018

Doubly-Excited Helium Strongly Driven with Short and Long Wavelength Pulses

This master thesis has been carried out by

Alexander Magunia

at the

Max-Planck-Institut

für Kernphysik

under the supervision of

Prof. Dr Thomas Pfeifer

and

Priv.-Doz. Dr Robert Moshammer

Doppelt Angeregte Heliumzustände in Wechselwirkung mit Laserpulsen Kurzer und Langer Wellenlängen:

In dieser Arbeit wird die Elektronendynamik in autoionisierenden, doppelt angeregten Zuständen des Heliumatoms untersucht. Dafür werden diese Zustände mit starken Lichtfeldern zweier verschiedener Spektralbereiche, dem infraroten und dem extrem-ultravioletten Bereich, gekoppelt. Es wurde ein Lasersystem installiert, welches erlaubt, die zentrale Wellenlänge seiner ultrakurzen Ausgangspulse zu variieren. Der zeitliche Verlauf dieser Pulse wird mit dem FROG Messverfahren charakterisiert. Zudem werden hohe Harmonische dieser Pulse erzeugt und untersucht. Erste intensitätsabhängige und zeitlich aufgelöste Experimente in Helium mit diesem Lasersystem werden präsentiert und an Hand von Simulationen diskutiert. Dabei wird der Übergang von einem ungestörten, Licht induzierten Zustand, welcher von dem $2p4p$ Zustand ausgeht, zu einer resonanten Autler-Townes Aufspaltung des $sp_{2,3+}$ Zustandes beobachtet. Darüber hinaus werden Starkfeld-Kopplungen des Helium Grundzustandes mit einem Zweielektronenzustand für extrem-ultraviolette Felder untersucht. Mit Simulationen werden Rabi-artige Kopplungen und lichtinduzierte Energieverschiebungen (Stark Effekt) für ultrakurze Laserpulse betrachtet, welche die Absorptionslinienform der Resonanz verändern. Ebenso werden autoionisierende Zustände untersucht. Diese theoretischen Betrachtungen werden verwendet, um die die Änderung der Linienform der $2s2p$ Helium Resonanz zu erklären, welche experimentell mit Hilfe eines Freie Elektronen Lasers (FEL) untersucht wurde.

Doubly-Excited Helium Strongly Driven with Short and Long Wavelength Pulses:

Within this work, electron dynamics of autoionizing, doubly excited states in helium are investigated. Therefore, strong field couplings of these states are studied in two spectral regimes: in the infrared and in the extreme ultraviolet. A laser system capable of tuning its output-pulses' central wavelength within the infrared spectral regime is installed and characterized by a FROG setup. Furthermore, high harmonics of these output pulses are generated and discussed. First intensity dependent and time resolved experiments in helium with this laser system are presented and supported by numerical calculations. The transition from an unperturbed light induced state, which is generated from the $2p4p$ state, to a resonant Autler-Townes splitting of the $sp_{2,3+}$ state is observed. Furthermore, strong field couplings between the ground and a doubly-excited state are studied in the extreme ultraviolet only regime. With the help of simulations Rabi-like couplings and Stark shifts for ultrashort pulses leading to a manipulated absorption line shape are investigated. The same study is carried out for autoionizing states. This theory part is used to explain experimentally measured line-shape changes of the $2s2p$ resonance in helium interacting with FEL pulses.

Contents

Introduction

Matter, light and time are all fundamental properties of nature. But how are the building blocks of matter interacting with each other? How is light interacting with matter – is it possible to use light to control matter? And, how are these interactions evolving in time?

These questions have been – and still are – among the central scientific questions when investigating the microscopic world of matter. It is built of atoms: nuclei surrounded by electrons, as well as molecules and solid structures: atoms forming bigger structures through couplings of their electrons. The understanding of this world is relevant for chemistry, biology, medicine and technology. A fundamental basis for understanding this microscopic world was set with the introduction of quantum mechanics, showing that matter and light can be treated in probabilistic manners.
One of the most established tools for studying quantum phenomena has been the laser (*light amplification by stimulated emission of radiation*), as its coherent light can be used for manipulating and investigating a system at the same time. With its help, many discoveries in the atomic and chemical world were made in past decades.
But all of them have been measured without a detailed understanding of the temporal evolution of the underlying processes, as they have been too fast for any human-made device to resolve them – comparable to a blurred image of a moving object taken with a long exposure time. The advent of ultrashort laser pulses changed this. The key idea for producing these pulses is simple, yet leads to two major improvements of laser sources: To achieve the shortest pulse durations possible, the light of a continuous wave (cw) laser is compressed within a short time window, intrinsically leading to ultrashort, and -intense laser pulses. They are short enough in time to allow to resolve processes on the natural time scales of atoms and molecules, which are in the femtoseconds (10^{-15} s) regime, and even electrons, for which attosecond resolution (10^{-18} s) might be necessary. Additionally, the laser pulses can be further amplified to high intensities to manipulate, control and even move quantum particles in an unseen extent.
Essential for achieving these degrees of control is the utilized laser's 'colour', its central frequency. It is connected to the energy of a single quantum light particle, the photon. As different processes in any kind of atoms and molecules take place at a wide range of energies, the right choice of the laser's frequency

is crucial to trigger certain events, and leave other parts of the manipulated atom or molecule unchanged.

Hence, one main part of this thesis goal has been the installation and characterization of a commercial laser system capable of producing ultrashort and -intense laser pulses, tunable from the visible to the near infrared frequency regime with the help of an optical parametric amplifier (OPA). A frequency-resolved optical gating (FROG) setup for characterizing these pulses' properties was built as well. The process for up-converting the light's frequency to the extreme ultraviolet (XUV) regime, called high harmonic generation (HHG), was additionally put into operation.
The intense OPA pulses – of long wavelengths – are combined with their high harmonics to perform strong field spectroscopy (SFS) investigating in a frequency resolved manner the light's interaction with atoms and molecules, which manifests in the studied absorption lines. The capabilities of the installed laser system are tested with first measurements of the benchmark system for electron-electron-correlations, helium. The two-electron correlations and light-matter interaction are studied observing doubly-excited states: At this resonances, a single photon can excite both electrons into a mutual state, which leaves an unique spectroscopic finger-print translating the internal correlations and interactions into a measurable quantity.
Furthermore, numerical calculations are implemented to model the system's quantum dynamics, as analytical descriptions are barely available even for the simple system of helium. The simulations help to understand the fundamental physics encoded in the experimentally observed dynamics. Additionally, the numerical analysis includes studies of the helium atom interacting with a single intense pulse in the XUV – the short wavelength – regime. This scenario is chosen to match experimental conditions at free-electron laser facilities, but is treated mainly numerically within this thesis.

This thesis is structured as follows: The first chapter (1) introduces into the main physical principles relevant for this thesis. For example, processes as the frequency-resolved optical gating (FROG) for laser pulse characterization and high-harmonic generation (HHG) for the up-conversion of the laser frequency are explained.
Afterwards, the installed laser system is presented in chapter (2) and an overview of the experimental vacuum setup for HHG and XUV experiments is given. Subsequently, the results of the FROG pulse-characterization are shown in chapter (3).
In the (4)th chapter the utilized numerical framework is explained. Furthermore, simulation results of a strongly driven doubly-excited state, the 2s2p resonance in helium, are presented. The laser pulses of short wavelengths are capable of exciting the resonance directly from the ground state as well as

manipulating it. The case of driving free-electron laser pulses referring to experiments performed at the free-electron laser in Hamburg is included as well. The first experimental results of SFS measurements with the long wavelength pulses of the recently installed laser system are discussed in chapter (5). Different HHG spectra for different driving pulses are shown as well as the intensity-dependent and time-resolved studies of the doubly-excited states in helium. They are compared to simulation results to obtain first insight into the measured electron dynamics.

1. Theoretical Background

This chapter presents the theoretical and mathematical foundation of this thesis. The sections are sorted from the main physical tools of this scientific work (ultrashort laser pulses) over to the subject of interest (electron correlation dynamics in helium), to the technique for combining and investigation them (absorption spectroscopy):

Sub-chapter (1.1) introduces the mathematical description of ultrashort laser pulses, which is followed by an overview of a pulse measurement and characterization technique called frequency-resolved optical gating (FROG) in (1.2). In addition, sub-chapter (1.3) presents a short summary of high harmonic generation (HHG), the method used to up-convert laser frequencies into the extreme ultraviolet (XUV) regime.

The next section (1.4) describes a selection of quantum mechanical phenomena necessary for this thesis: A short recap about the framework of quantum mechanics in (1.4.1) is meant to set the foundations for the later numerical simulations in chapter (4). As the helium atom is the primer subject of study in this thesis, its level scheme, evolving from the electron-electron correlation, is shown in (1.4.2) and some of the resulting properties, in form of autoionization manifesting in so called Fano resonances, are discussed in (1.4.3). Afterwards, the regime of light-matter interaction is investigated by looking at light-induced states and Rabi coupling in (1.4.4).

Finally, section (1.5) combines all of the aforementioned aspects within the experimental method involved for these quantum-dynamical investigations called strong field (absorption) spectroscopy.

1.1. Ultrashort Pulses

In the following, an introduction into ultrashort laser pulses is given. For the purpose of this thesis, a laser pulse is seen as a semiclassical electromagnetic wave packet, following descriptions given in text books like [1].
First, the definition of 'ultrashort' shall be explained: Pulse durations in the order of picoseconds (ps = 10^{-12} s), femtoseconds (fs = 10^{-15} s) and attoseconds (as = 10^{-18} s) belong to this regime. Yet, the following treatment is

primary meant to describe fs-pulses as introduced in the following chapter 2.

A complex representation of the electric-field amplitude is the convenient choice for describing the pulses. A common simplification is the reduction of ths spatio-temporal treatment to the temporal domain: $E(x, y, z, t) = E(t)$. One of the important mathematical concepts used through the whole thesis, is the Fourier-transformation $[\mathcal{F}\{\cdot\}]$, described e.g. in [2]. With the help of the Fourier-transformation and starting with a real temporal electric field, a complex description of the corresponding spectral electric field can be formulated:

$$\tilde{E}(\omega) = \mathcal{F}\{E(t)\} \equiv \int_{-\infty}^{+\infty} E(t) \cdot e^{-i\omega t} dt = |\tilde{E}(\omega)| \cdot e^{i\tilde{\Phi}(\omega)} \ , \tag{1.1}$$

where $|\tilde{E}(\omega)|$ represents the spectral amplitude and $\tilde{\phi}(\omega)$ is the spectral phase. From there, one can go back to the temporal domain by employing the complex inverse Fourier-transformation $[\mathcal{F}^{-1}\{\cdot\}]$:

$$E(t) = \mathcal{F}^{-1}\{\tilde{E}(\omega)\} \equiv \frac{1}{2\pi} \int_{-\infty}^{+\infty} \tilde{E}(\omega) \cdot e^{i\omega t} dt \ . \tag{1.2}$$

At this point, the temporal representation is real, whereas the spectral one is complex and includes negative, physical meaningless, frequencies. To solve for both inconveniences, a complex temporal electric field is defined only for the positive frequencies:

$$E^{+}(t) = \frac{1}{2\pi} \int_{0}^{+\infty} \tilde{E}(\omega) \cdot e^{i\omega t} dt \ , \tag{1.3}$$

leading to a consequential definition of the spectral representation:

$$\tilde{E}^{+}(\omega) = \begin{cases} \tilde{E}(\omega) & \text{for } \omega \ \geq \ 0 \\ 0 & \text{for } \omega \ < \ 0 \ . \end{cases} \tag{1.4}$$

These two complex quantities are related by the complex Fouriertransforamtion similar as in equations (1.1) and (1.2):

$$E^{+}(t) = \frac{1}{2\pi} \int_{-\infty}^{+\infty} \tilde{E}(\omega) \cdot e^{i\omega t} dt \equiv \mathcal{E}(t) \cdot e^{i\phi(t)} \tag{1.5}$$

$$\tilde{E}^{+}(\omega) = \int_{-\infty}^{+\infty} E(t) \cdot e^{-i\omega t} dt \ \equiv \tilde{\mathcal{E}}(\omega) \cdot e^{i\tilde{\phi}(\omega)} \ . \tag{1.6}$$

Equations (1.5) and (1.6) introduce a convenient formalism, that allows to switch from temporal to spectral domain in complex representation. Furthermore, in equations (1.5) and (1.6) the quantities $\mathcal{E}(t)$ and $\tilde{\mathcal{E}}(\omega)$ are defined as

amplitudes, and $\phi(t)$ and $\tilde{\phi}(\omega)$ depict the temporal and spectral phase, respectively. Note, that the amplitudes are in principle experimentally measurable in form of the autocorrelation ($A(\tau) \equiv \int_{-\infty}^{+\infty} |E^+(t)|^2 \cdot |E^+(t-\tau)|^2 dt$) and the power spectrum ($\tilde{S}(\omega) \equiv |\tilde{E}^+(\omega)|^2$), whereas the phases are not directly accessible.

For simplification one can assume the temporal electric-field amplitude $\mathcal{E}(t)$ to be Gaussian, what leads to a Gaussian form of $\tilde{\mathcal{E}}(\omega)$ as well. The uncertainty principle leads to a correlation of the widths in the temporal and spectral domain, referred to as the time-bandwith product (TBP) [1]:

$$\Delta t \cdot \Delta\omega \geq \text{constant} \ , \tag{1.7}$$

where the (intensity) full widths at half maximum (FWHM) Δt, $\Delta\omega$ are connected to the standard deviations $\sigma_{(t,\omega)}$ of a Gaussian distribution via:

$$(\Delta t, \ \Delta\omega) \equiv 2\sqrt{2\ln 2 \cdot \sigma_{(t,\omega)}} \ . \tag{1.8}$$

The constant in eq. (1.7) depends on the chosen envelope. In case of a Gaussian envelope, a value of 0.441 holds. Notably, the equal sign in eq.(1.7) is only valid for *Fourier-transform-limited* pulses, which is the case for a constant or linear phase. To understand which role the spectral phase plays for the value of the TBP, a Taylor-expansion of the spectral phase around the central frequency of the spectrum, the *carrier-frequency* ω_c, is employed:

$$\tilde{\phi}(\omega) = \sum_{k=0}^{+\infty} \frac{d^k \tilde{\phi}(\omega-\omega_c)}{d\omega^k} \frac{(\omega-\omega_c)^k}{k!} \tag{1.9}$$

$$= \phi_0 + \tau_{GD} \cdot (\omega-\omega_c) + \chi_{GDD} \cdot (\omega-\omega_c)^2 + \chi_{TOD} \cdot (\omega-\omega_c)^3 + \dots \ . \tag{1.10}$$

A treatment of the temporal phase is analogue to that. From this mathematical formulation, one can extract useful information as in general only few of the leading terms (up to third order) play a significant role in experimental measurements. They are defined in table (1.1).
The impacts of these spectral quantities on the temporal domain can be understood with a Fourier analysis. In summary: The carrier-envelope phase is only relevant for few-cycle pulses. As this regime is not reached within this thesis, it will not play a significant role and thus will not be explained further. The group delay (GD) shifts all spectral components by the same amount, leading to a temporal offset of the whole pulse. The group delay dispersion (GDD) introduces a linear chirp, which causes different spectral components to arrive at different times. As a consequence, the pulse becomes longer and does not

minimize the uncertainty in eq. (1.7) any more:

$$\sigma_{chirped} = \sqrt{\sigma_0^2 + \left(\frac{\text{const.} \cdot \chi_{GDD}}{\sigma_0}\right)^2} \,. \tag{1.11}$$

Furthermore, a non-zero third-order dispersion (TOD) leads to a quadratic chirp. Frequencies equally smaller and larger than the carrier-frequency are shifted in time by the same amount and into the same direction (as a quadratic dependence is symmetric around ω_c, whereas a linear one is not). Theses pair of frequencies interfere with each other in form of a beating. In total, this beating in the temporal domain can lead to pre- and post pulses around the main pulse located at τ_{GD}.

The description of ultrashort pulses via reduction of their spectral phase expansion to only the first terms, holds in most cases for well defined pulse generations, e.g. table-top laser systems, as the one presented in section (2.1). On the other hand, there are laser pulses with such a complex phase behaviour, that they cannot be Taylor-expanded even up to very high orders. An example for such pulses are pulses generated by free-electron lasers (FELs). The pulses presented in chapter (4.1.2) are of such nature. They originate from the process of *self-amplified spontaneous emission* (SASE) of light from relativistic electron bunches. The reader is referred to [2] for further information. As a result of this process, the pulses are only partially coherent, due to a discontinuous, nearly random phase, which can be Tayor-expanded only piecewise. Their temporal amplitude contains lots of substructure compared to a Gaussian envelope. See section (4.1.2) for a plot of a partially coherent pulse (fig.(4.2)).

symbol	name	impact on the time domain
ϕ_0	carrier-envelop phase	wave position to envelope position shift
τ_{GD}	group delay	temporal shift of the envelope by τ_{GD}
χ_{GDD}	group delay dispersion	linear chirp, longer pulse duration
χ_{TOD}	third-order dispersion	quadratic chirp, pre- & post-pulses

Table 1.1.: Coefficients of the Taylor-expanded spectral phase

1.2. Principle of Frequency-Resolved Optical Gating

Ultrashort laser pulses, as described in the previous chapter, are the fastest synthetic events, humans can create and control. Thus, measuring such pulses is not trivial, as they are in general too fast for any electronic device [3]. Nonetheless, several pulse characterization methods have been developed in recent years, exploiting non-linear optics and based on the idea of using the pulses themselves, or another ultrashort pulse, for building a measuring device. The first method, autocorrelation, was introduced in 1967 by [4], which is capable of measuring the temporal amplitude (under certain asumptions), but not the phase properties. For a full pulse characterization the measurement of the phase is essential. Therefore, the *frequency-resolved optical gating (FROG)* method in 1993 [5–7], the *spectral phase interferometry for direct electric-field reconstruction (SPIDER)* method in 1998 [8, 9] or the *dispersion scan (D-scan)* method in 2012 [10], to name only a few, have been developed. In this thesis, a FROG setup has been built to characterize the pulses generated by the laser system described in section (2.1). This chapter deals with the theoretical background of FROG, whereas chapter (3) describes and discusses the experimental setup and measured pulse structures.

The basic idea of the FROG technique is the measurement of a two-dimensional data set in time and frequency domain, from which the the full temporal pulse characterization can be derived with the help of an iterative algorithm. For that purpose, the spectrogram $S(\omega, \tau)$ of a non-linear signal is recorded depending on an intrinsic time delay τ between the laser pulse and a non-linear gating function $g(t-\tau)$:

$$S(\omega, \tau) = \left| \int_{-\infty}^{+\infty} E(t)\ g(t-\tau)\ e^{-i\omega t}\ dt \right|^2 . \tag{1.12}$$

Thus, it can be seen as a spectrally resolved autocorrelation trace. The non-linearity in the signal is based on altering the polarization of a dielectric medium with the pulse's electric field $E(t)$ and thus introducing a time dependent polarization $P(t)$. As in [11], its spectrum can be Taylor-expanded:

$$P(\omega) = \epsilon_0 \left[\underbrace{\chi^{(1)} E(\omega)}_{P_{linear}} + \underbrace{\chi^{(2)} E^2(\omega) + \chi^{(3)} E^3(\omega) + ...}_{P_{non-linear}} \right] . \tag{1.13}$$

Different FROG techniques use different non-linear processes, which translates to different $g(t, \tau)$. The most used FROG types are: *Polarization gating (PG)*,

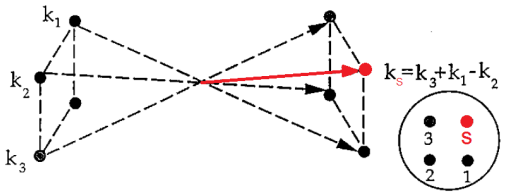

Figure 1.1.: **BOXCARS geometry of the TG-FROG**
The fourth signal beam (S, red) in a TG-FROG setup is emitted into the direction of the missing corner of a square spanned by the three incoming beams. Fig. adapted from [5].

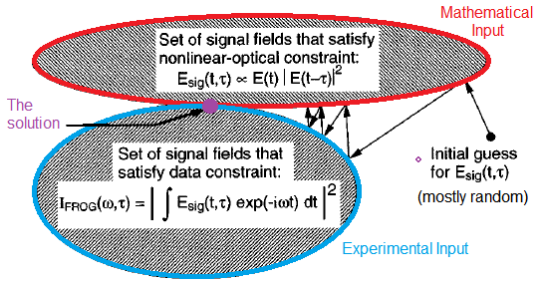

Figure 1.2.: **Retrieval algorithm**
The iteration between the experimental data $S(\omega, \tau)$ and the mathematical description of it's generation converges to the desired pulse characterization. Fig. adapted from [5].

self-diffraction (SD), *transient-grating (TG)* and *second- and third-harmonic generation (SHG, THG)*. In this thesis, a TG-FROG was build and described in section (3.1). In that setup, two of three incoming beams in the so called *BOXCARS*-geometry (see. fig. (1.1)), generate a grating from which the third incoming beam diffracts. This generates the fourth signal beam propagating into a direction according to momentum conversation. The configuration is chosen in a way, that the third beam is delayed in time with respect to the other ones. The gating function of this χ^3 non-linear process is equivalent to the one of the PG-FROG (with reversed sign of τ):

$$g(t, \tau) = |E(t + \tau)|^2. \tag{1.14}$$

One can extract the phase information from the tempo-spectral amplitude measurement $S(\omega, \tau)$ via the iterative algorithm, called *General Projection (GP)* algorithm. As fig.(1.2) shows, the retrieval needs the mathematical non-linear dependency as a counterpart to the experimental measured $S(\omega, \tau)$ to be able to converge iteratively to the desired pulse characterization. For that, a temporal pulse is guessed initially and the corresponding signal $S(\omega, \tau)$ is calculated and compared to the measurement. In the next step, the difference between calculated and measured signal is minimized by varying the spectral phase initiated by an arbitrary guess.
The aim is the full characterization of a pulse, described by either temporal or spectral amplitude and phase. As each consists of N data-points, the $N \times N$ data set contains more information than the necessary minimum, which in

general leads to a good convergence of the retrieval.
Furthermore, measured FROG spectrograms $S(\omega, \tau)$ can be linked to the corresponding spectral phase coefficients introduced before in tab.(1.1) (compare to fig.(1.3)).

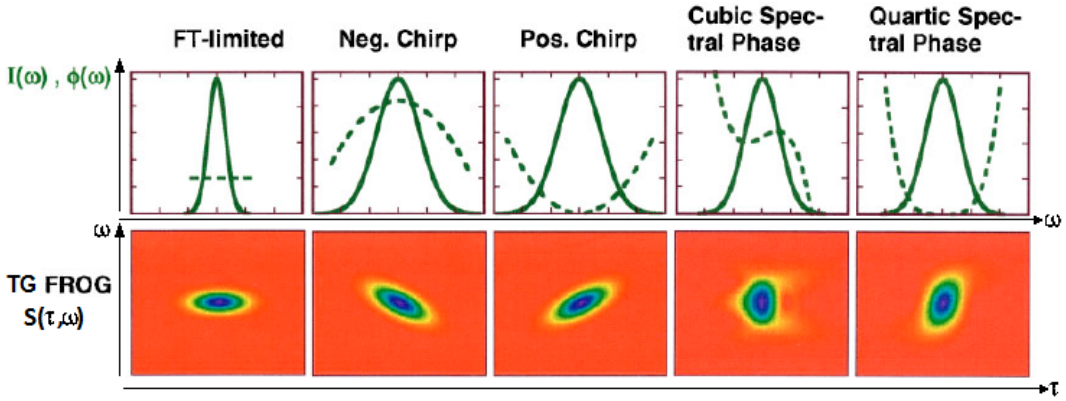

Figure 1.3.: **TG-FROG spectrograms for different spectral phases**
The variation of the spectral phase of a otherwise identical Gaussian pulse creates different outcomes for the spectrograms $S(\omega, \tau)$. Linear and quadratic chirps differ by a different type of symmetry of the spectrogram compared to each other and to the FT-limited case. Therefore, the measurement of the spectrogram combined with the GP algorithm can determine not only the intensity but also the phase behaviour of a pulse. Fig. adapted from [5].

1.3. High Harmonic Generation

This section will introduce the highly non-linear process (in the sense of eq.(1.13)), known as high harmonic generation (HHG). This method is key to generate light pulses even shorter than the ones presented in section (1.1), in the attosecond regime, and with photon energies in the extreme ultraviolet (XUV) to soft X-ray region ($\sim$ (10 eV - 1 keV)). Both properties are excellent for studying the dynamics of electrons, as they are bound to atoms or molecules with energies accessible within the HHG spectrum as well as the natural time scale of autoionizing doubly-excited states (in helium) is in the order of fs (see section (1.4.3) for more details).
Since HHG is a process, in which an electron gets ionized by a strong laser field and afterwards interacts with this light field and it's parent nucleus, a short introduction into strong-field theory is required first: Whenever a single photon is not enough for ionizing an atom, several strong-field ionization processes can still take place. They can be characterized into three different

regimes using the 1965 established Keldysh parameter γ [12]:

$$\gamma = \sqrt{\frac{I_p}{2U_p}}, \tag{1.15}$$

where I_p is the ionization potential of the atom and U_p is the ponderomotive energy:

$$U_p = \frac{e^2 \mathscr{E}_0^2}{4 m_e \omega^2}. \tag{1.16}$$

U_p is the mean kinetic energy of a free electron (with mass m_e and charge e) that can be accumulated by an acceleration due to the interacting with a monochromatic light field $E(t) = \mathscr{E}_0 cos(\omega t)$:

$$a(t) = -\frac{e}{m_e} E(t). \tag{1.17}$$

In principle, the Keldysh parameter in eq.(1.15) compares the impact of the light field on an electron (in form of U_p) to its binding energy (in form of I_p). The following three strong-field ionization types can be defined:

name	γ	interpretation
multi-photon ionization (MPI)	$\gamma \gg 1$	light field leaves potential undisturbed, absorption of several photons necessary
tunneling ionization	$\gamma \leq 1$	laser field bends atomic Coulomb potential, electron can tunnel out through barrier
barrier-suppression ionization (BSI)	$\gamma \ll 1$	strong distortion of Coulomb potential, states are not bound any more

Table 1.2.: strong-field ionization types

The different ionization types are also sketched in fig.(1.4): For $\gamma \gg 1$, the light field oscillates too fast to affect the atomic potential, but is intense enough for multiple photons to be absorbed non-sequentially, hence ionizing the atom. For higher intensities and slower oscillating fields, resulting in a decreasing γ following eq.(1.15), the field can be assumed to be static. As the acceleration of (and therefore the force on) the electron by the light field in eq.(1.17) is spatially constant, the laser potential can be approximated to be linear in space (compare fig.(1.4) b), c)). The combination of laser and atomic potential leads to a total potential, which allows the electron to tunnel out in case of b) and even leave unhindered for strong enough light fields, depicted in c). A more detailed summary of the Keldysh theory of ionization can be found in [13].

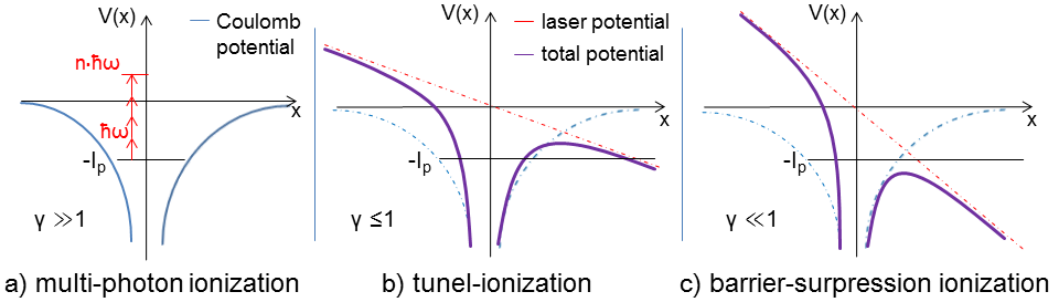

Figure 1.4.: **Strong-field ionization**
For different regimes of the Keldysh-parameter γ a specific strong-field ionization process is dominant. In a) non-sequential multi-photon absorption leads to ionization for $\gamma \gg 1$. In b) a quasi-static laser potential bends the Coulomb potential, so that an electron can leave the atom via tunnelling, as $\gamma \leq 1$. For even smaller values of $\gamma \ll 1$, the effect in b) is amplified, which leaves the total potential unable to contain a bound state, leading to a unhindered ionization in c).

The semiclassical description of the HHG process, which has become famous under the name *three-step model* after first theoretical descriptions [14] and experimental proof [15], starts with tunneling ionization as the first step (see fig.(1.5)). Secondly, the ionized electron interacts with the laser field, thus is accelerated and gains kinetic energy. After half a period of the light field, the sign of the field's amplitude changes, thus the electron is driven back to the nucleus. Finally, it can recombine with the atom and give away its energy in form of a single high-energy photon:

$$\hbar\omega_{HHG} = E_{kin}^{(r)} + I_p. \tag{1.18}$$

There exist two classical electron trajectories for the same kinetic energy at recombination $E_{kin}^{(r)}$ within one cycle of the driving laser field, known as short and long trajectory. Not only do both of them interfere, but also, as this three-step process has an half laser-cycle periodicity, the light emitted at this half-cycle events interferes as well. In total, the interference leads to a photon-energy spectrum containing harmonics $(n \cdot \omega)$ of the driving field (ω) with 2ω-spacing due to the half-cycle periodicity of the process. The spectral intensity of the harmonics decreases rapidly for low energies before changing to a plateau-like behaviour for most of the harmonics. At highest photon energies it vanishes after a sharp cutoff.
This cutoff can be most precisely predicted by a full quantum treatment of the HHG process [16]. There, the electron wave packet is partly ionized by the driving field. During the interaction of the the ionized wave packet with the

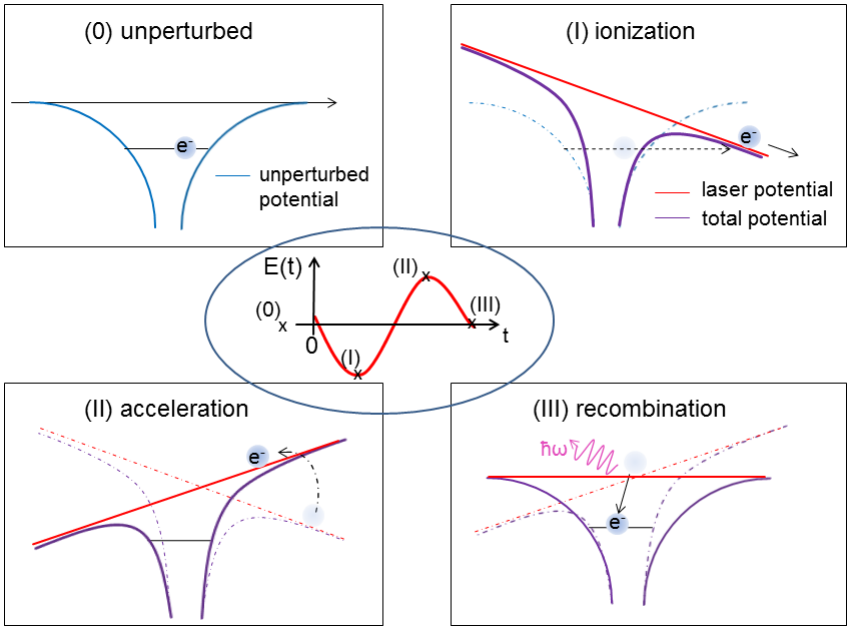

Figure 1.5.: **Three step model of the high-harmonic generation** The unperturbed potential in (0) is bent by the laser potential as in fig.(1.4) for tunneling ionization to occur in (I). As marked in the inset in the centre, the electric field is nearly extremal there. An half cycle later, the field's amplitude is at the other extreme (see inset) and has changed it's sign, thus the potential is now bended into the other direction, driving the electron back to it's parent atom in (II). When the field is nearly at a root, the electron recombines with the atom in (III), emitting a high-energy photon.

light field, the atomic influence is neglected. The recombination takes place by quantum interference of the back-driven wave packet with the one, that remained bound to the nucleus. The resulting dipole emission of this process contains the harmonic spectrum, similar to, but more precisely described than the aforementioned three-step model. As one of the outcomes, the maximal kinetic energy, the electron can gain by interacting with the laser field, can be written with help of the ponderomotive energy introduced in eq.(1.16):

$$E^{(r)}_{max.\ kin} = 3.17\ U_p, \tag{1.19}$$

leading to a cutoff frequency of the harmonic spectrum of:

$$\hbar\omega_{cutoff} = 3.17U_p + I_p. \tag{1.20}$$

Therefore, higher harmonic photon energies are reachable in atoms with high ionization potential as well as with intense and long-wavelength lasers. But

the efficiency for too large intensities drops again rapidly, when too much ionization events and thus plasma generation occur.
As a consequence, the so called *phase-matching condition* has to be considered, which has to be met for optimized HHG conversion output. For that, it is necessary to switch from the presented microscopic (single atom) perspective to a macroscopic perspective, e.g. an ensemble of gas atoms. For a single atom, the harmonic spectrum can be seen as a probability function of emitting a photon with a given energy, whereas for an ensemble of atoms this probability translates to a measurable spectral intensity. So for optimized HHG intensity, the macroscopic behaviour has to be considered. Not every atom and every harmonic photon energy can be optimized at once, but in average the phase-mismatch Δk between all harmonics and the driving field has to be minimized:

$$\Delta k = \Delta k_{dispersion} + \Delta k_{plasma} + \Delta k_{dipole} + \Delta k_{Gouy}. \tag{1.21}$$

It contains several terms, which depend on the in- and outgoing light's frequency and intensity, thus varying with the harmonic order and within a macroscopic target gas volume
The first term $\Delta k_{dispersion}$ contributes to the normal dispersion of the gas medium, whereas the second term Δk_{plasma} describes the dispersion in a plasma, which is produced during the HHG process. The third term Δk_{dipole} accumulates all quantum-mechanical interference effects of the previously described theoretical, microscopic dipole-emission. The last term Δk_{Gouy} stands for all focussing effects due to curvature of the wave front. If the driving laser is assumed to be Gaussian, it can be described by the Gouy phase. The topic will be further discussed from a practical/experimental perspective in chapter (5.1).

1.4. Quantum Dynamics

It is well known, that the Schrödinger equation (SEQ) is suitable for describing the non-relativistic quantum world [17]. A brief introduction into the mathematical description of quantum mechanics is given in (1.4.1). Unfortunately, the SEQ is analytically solvable only for the simplest of all atoms, hydrogen. Starting from helium to larger atoms with more electrons, the electron correlations denies an analytical description. This can be regarded as general motivation to investigate electron-electron correlations within the simplest system, helium. An overview of how the electrons arrange into approximated states is shown in (1.4.2). These first two sub-sections set the foundation, on which the numerical framework presented in chapter (4) is based on.
As a consequence of the electron correlation, the process of *autoionization* occurs. It becomes visible in form of asymmetric *Fano line shapes*, which is

explained in (1.4.3). To further investigate those correlations, intense light fields in the so called strong-field regime are used. Their light-matter interaction is introduced in the last subsection (1.4.4) by taking the example of Rabi-coupling using *light-induced states* (LIS), which are also known as dressed states.

1.4.1. General Description of Quantum Mechanics

In quantum mechanics, states $|\Psi(x,t)\rangle$ are introduced to model the probabilistic (non-deterministic) dynamics of particles and wave-packets. As in most other fields of physics, energy plays a central role in parametrizing these dynamics, where in quantum mechanics the Hamilton-operator $\mathscr{H}$ is introduced for that purpose. It can be used to formulate the Schrödinger equation (SEQ), the equation of motion for non-relativistic quantum particles:

$$i\hbar\frac{\partial}{\partial t}|\Psi(x,t)\rangle = \mathscr{H}|\Psi(x,t)\rangle. \tag{1.22}$$

For the *stationary* case, this partial differential equation becomes a less complicated eigenvalue equation. Its solution is a set of N normalized eigenstates $|\Psi_n(x)\rangle$ and their corresponding eigenvalues E_n to the operator $\mathscr{H}$, which hence can be written as an N×N-matrix in the *matrix-formalism* of the SEQ. Note, that N can be infinity, and the eigenstates do not have to be discrete.
The physical problem to be solved by the SEQ is encoded in the choice of an adequate $\mathscr{H}$-operator. For example, the Hamiltonian can be chosen to be the sum of kinetic energy and a bound electrostatic potential, which is basically the description of one electron in an atom. There, the discrete solutions are called bound states. Their time propagation is described as a phase evolution:

$$|\Psi_n(x,t)\rangle = e^{-iE_nt/\hbar}|\Psi_n(x)\rangle. \tag{1.23}$$

The resulting system of stationary states is an orthonormal system, sorted by its increasing eigenenergies E_0 (ground state) $< E_1 < ... < E_N$ (excited states). In general, every state, which is a solution of the corresponding SEQ, can be written as a superposition of these eigenstates:

$$|\Psi(x,t)\rangle = \sum_n c_n\ |\Psi_n(x,t)\rangle. \tag{1.24}$$

Here, the coefficients $c_n(x,t) = \langle\Psi(x,t)|\Psi_n(x,t=0)\rangle$ quantify the probability to be in the eigenstate n by taking the squared absolute value: $P_n = |c_n|^2$, if the normalization condition $\sum_n P_n = 1$ is met. As mentioned before, an analytical description of a set of eigenstates $|\Psi_n(x,t)\rangle$ exist for neutral hydrogen and hydrogen-like ions.

For atoms with two or more electrons, one has to include a term for the (electrostatic) electron-electron interaction into $\mathscr{H}$. Furthermore, there exist more than one ionization continua, which are described by so-called free states. It is convenient to treat them as wave packets consisting of a continuum of waves parametrized by their momentum $p' = \hbar k$:

$$\Psi_{p'}(x) = \frac{1}{\sqrt{2\pi\hbar}} e^{ip'x/\hbar}, \tag{1.25}$$

with continuous eigenenergies $E' = \frac{p'^2}{2m}$. A general state of a quasi-free electron can be described by these new eigenfunctions, as the superposition principle still holds. For this purpose, the sum in eq.(1.24) has to be exchanged by an integral over E' and the probability coefficients will be defined as $b_{E'}$:

$$|\Psi_{E'}\rangle = \int dE' \; b_{E'} |\Psi_{E'}\rangle. \tag{1.26}$$

As presented in the following section (1.4.2), for two-electron systems, there can be bound, *doubly-excited* states, that coincide energetically with the one-electron ionization continuum. A general state for such electrons is represented by an admixture of bound states and free states (compare sec. (1.4.3)):

$$|\Psi\rangle = \sum_n c_n \; |\Psi_n\rangle + \int dE' \; b_{E'} |\Psi_{E'}\rangle. \tag{1.27}$$

1.4.2. Electron-Correlation and Level Scheme of Helium

To investigate the electron-electron-correlation in helium, considered the two electrons in helium are indistinguishable fermions, a two-electron wave-function has to be formulated with certain symmetry properties:

$$\Psi = \psi\left(\vec{r_1},\ \vec{r_2}\right) \cdot \chi\left(s_1,\ s_2\right), \tag{1.28}$$

where ψ represents the spatial wave function of the electrons located at $\vec{r}_{1,2}$ and χ accounts for the spin contribution of the two spins $s_{1,2}$. The spectroscopic notation of such states reads as follows: ${}^{2S+1}L^{o,e}$. Here, L stands for the total angular momentum quantum number (note, that L is given as (S,P,D,..) instead of (0,1,2,..) for historic reasons) and S is the total spin quantum number. The indices: (o, e) indicate odd (o) or even(e) parity of the state.
The spin contribution to the observed dynamics can be neglected in the rest of this thesis, as only singlet states with an asymmetric χ leading to a total spin of $S = 0$ are taken into account for spectroscopic investigations. This also leads to the condition that ψ has to be symmetric due to Pauli's principle for fermions, stating that Ψ hast to be antisymmetric.

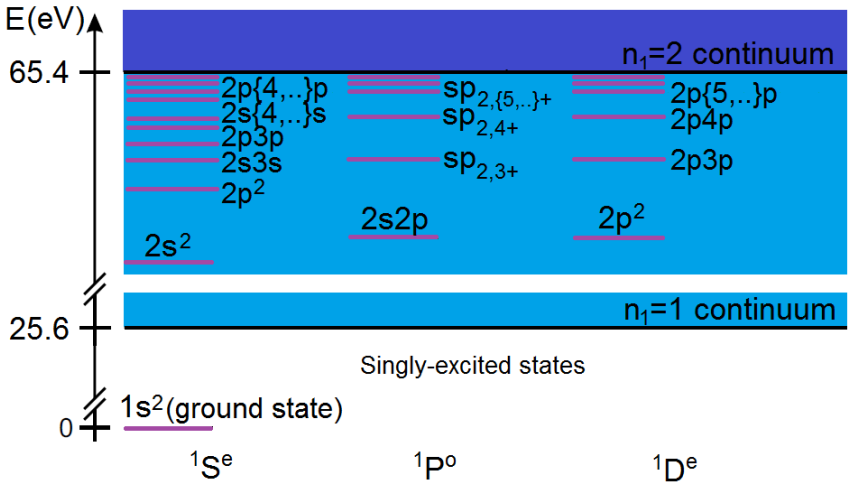

Figure 1.6.: **Level scheme of doubly-excited states in helium**
The resonances of the doubly-excited states are taken from [21–24]. Only the '+' states of the overlapping states defined in the text are shown for simplicity. States, which belong to the ${}^1S^e$ and ${}^1D^e$ symmetries are spectroscopically not visible.

Furthermore, transitions between those states due to laser interaction are treated in the dipole approximation for the rest of this thesis. Thus, a single-photon transition demands $\Delta L = \pm 1$ and a change of parity. In general, a two-electron wave function cannot be described as a product of two single-orbital electron wave functions, as electron-electron correlations take place via Coulomb interaction:

$$\Psi^{(2)}\left(\vec{r_1},\ \vec{r_2}\right) \neq \Psi^{(1)}\left(\vec{r_1}\right) \cdot \Psi^{(1)}\left(\vec{r_2}\right). \tag{1.29}$$

There exist plenty of analytical approximations, e.g. the Hartree-Fock method [18], starting from uncorrelated single-electron wave-functions and iteratively converging to more precise states, or group-theoretical approaches as described in [19]. Alternatively, numerical models, for example based on *ab-initio* calculations, can also simulate few- to multi-electron correlations [20].
For the purpose of this thesis, only the energy-eigenvalues of the doubly-excited states (DES) are needed, which can be taken from experimental XUV spectroscopy [25]. These resonances correspond to excitations from the ground state, ${}^1S^e$, to doubly-excited states. For simplicity, they are classified in terms of single-electron quantum numbers: $|n_1 l_1, n_2 l_2\rangle$, where $n_{1,2}$ stand for the principle quantum numbers and $l_{1,2}$ for the angular momentum quantum numbers. This classification is valid for low enough values of $n_{1,2}$, to what the context of this thesis will be restricted to. Three different configuration series ($|2s, n_2 p\rangle$,

$|2p, n_2 s\rangle$, $|2p, n_2 d\rangle$) contribute to the energetically lowest lying series ($n_1 = 2$) with the spectroscopic accessible ${}^1P^o$ symmetry. All three of them converge to the $n_1 = 2$ continuum threshold at 65.40 eV. The first two series cannot be distinguished energetically, thus they appear in form of linear combinations of overlapping states:

$$|sp_{2,n\pm}\rangle \equiv \frac{1}{\sqrt{2}} \left(|2s, n_2 p\rangle \pm |2p, n_2 s\rangle \right), \tag{1.30}$$

where historically the '+'-series appears to be the spectroscopically stronger one.
As fig.(1.6) shows, the states of this $n_1 = 2$ series are degenerate with the single-electron ionization continuum. This leads to a process known as autoionization, which will be discussed in the following subsection.

1.4.3. Autoionization and Fano Lines

The key feature for autoionization is the energy-wise embedding of the DESs in the one-electron ionization continuum, compare fig.(1.6) violet lines of DESs with blue continuum background. This degeneration is referred to as *configuration interaction* and allows the two electrons in a DES to undergo a process known as Auger decay, meaning that one of the electrons drops to an energetically lower lying state, giving its energy to the second electron, which then can leave the atom. As no external trigger, e.g. no laser interaction, is necessary, this ionization process is called autoionization. Typical lifetimes of autoionizing states are on the order of tenths to hundredths of fs, corresponding to spectral line widths of $\Gamma \propto$ 1 - 10s of meV, which is much faster compared to singly-excited states spontaneously decaying within nanoseconds.
Since the helium atom can also be ionized directly with a laser field of the appropriate frequency, there exist two different pathways for the helium atom to be singly-ionized from the ground state, see fig.(1.7). These two quantum pathways give rise to an interference manifesting in the absorption line shape. The first mathematical description of the configuration interaction of DESs was given by U. Fano in 1961 [26]. As one of the main results, the asymmetric line shape of a autoionizing resonance is now known as Fano line, which is characterized by its asymmetry q-parameter:

$$\sigma(\epsilon)_{Fano} \propto \frac{(q+\epsilon)^2}{1+\epsilon^2} \ , \tag{1.31}$$

where ϵ is defined as photon-energy relative to the resonance position E_r:

$$\epsilon \equiv \frac{E_{photon} - E_r}{\Gamma/2} \ . \tag{1.32}$$

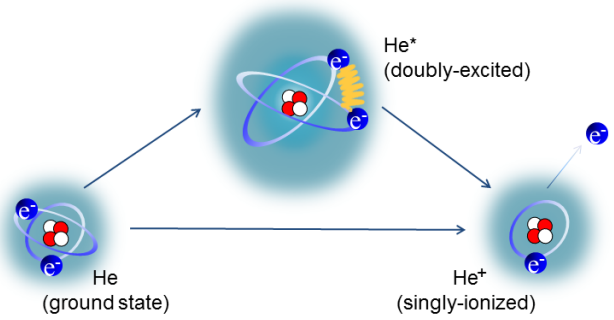

Figure 1.7.: **Direct- and autoionizaion of the helium atom**
The configuration interaction of the DES with the ionization continuum allows for autoionization to occur (upper path) besides the direct ionization (lower path). The interference of these two paths lead to so called Fano line shapes.

The above mentioned interference effect manifests in a maximum and minimum of the line-shape. Their relative strength is controlled by the q-parameter (see fig.(1.8)).
A recapitulation of the resonance position, line widths and q-parameters of the DES $n_1 = 2$ series is presented in table (1.3).

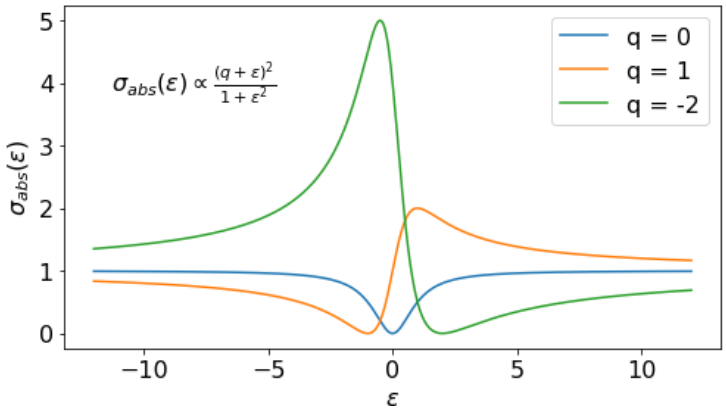

Figure 1.8.: **Fano line shapes**
The absorption cross sections σ_{abs} for Fano resonances with different q-parameters is plotted vs. the relative energy position defined in eq.(1.32). A change of sign of q leads to a mirrored symmetry. For lim q $\to \pm\infty$, the line-shape becomes Lorentzian.

state	energy (eV)	line width (Γ in meV)	q-parameter	
$2s^2$	58.00	123.6	-	$^1S^e$
$2s3s$	62.96	37.1	-	
$2s4s$	64.19	13.4	-	
$2s5s$	64.68	5.9	-	
$2s6s$	64.93	3.1	-	
$2p^2$	62.09	5.9	-	
$2p3p$	64.10	2.0	-	
$2p4p$	64.65	1.3	-	
$2p5p$	64.92	0.8	-	
$2p^2$	59.96	70.6	-	$^1D^e$
$2p3p$	63.64	16.8	-	
$2p4p$	64.42	7.1	-	
$2s2p$	60.15	37.4	-2.75	$^1P^o$
$sp_{2,3-}$	62.76	0.1	-4.25	
$sp_{2,3+}$	63.66	8.2	-2.58	
$sp_{2,4-}$	64.14	0.1	-3.32	
$sp_{2,4+}$	64.47	3.5	-2.55	
$sp_{2,5-}$	64.67	<0.1	-3.31	
$sp_{2,5+}$	64.82	1.8	-2.54	
$sp_{2,6-}$	64.92	<0.1	-3.31	
$sp_{2,6+}$	65.00	1.0	-2.53	

Table 1.3.: Properties of the $n_1 = 2$ DES manifold
The presented data is taken from [21–24]. The positions of the resonances are sketched in fig.(1.6).

1.4.4. Light-Induced States and Rabi Coupling

The following content is about the light-matter interaction in the so called strong-field regime. The strong-field definition can vary depending on the physics to be described. For this thesis, we consider a two-level system driven by a light field strong enough, so that light-induced states (also known as dressed states) or Rabi coupling can occur. Both effects will be described in the following.

The electromagnetic wave is treated as monochromatic and therefore as a continuous wave (cw). It interacts with the two-level system: $|\phi_1\rangle$ & $|\phi_2\rangle$, via dipole-interaction. Thus, the Hamiltonian for this scenario reads as:

$$\hat{\mathscr{H}} = \hat{\mathscr{H}}_0 \; + \; \hat{d}_{12} \cdot \hat{E}\,(t)\,, \tag{1.33}$$

where $\hat{\mathscr{H}_0}$ represents the unperturbed Hamilton operator and $\hat{d_{12}}$ is the dipole operator describing transitions between the states ϕ_1, ϕ_2. $\hat{E}(t)$ introduces an operator for the electromagnetic field. Its eigenstates are described by the photon number states (Fock states) $|n\rangle$, which lead to an infinite amount of eigenstates for the interaction term $\hat{d}\cdot\hat{E}$. The new eigenstates of the perturbed two-level system can be written for a first notation as combinations of the two-level states and the Fock states:

$$|\{\phi_1, \phi_2\},\ \{0,\ ...,\ n-1,\ n,\ n+1,\ ...\infty\}\rangle \tag{1.34}$$

For a frequency of the electromagnetic wave ω_l near the transition frequency ω_{12} the description can be reduced to manifolds $\mathscr{M}_n$ consisting of only the absorption of a photon from the lower state $|\phi_1\rangle$ and an emission of a photon from the upper one $|\phi_2\rangle$ leading to the relevant set of (uncoupled) eigenstates:

$$|\phi_1,\ n\rangle,\ |\phi_1,\ n+1\rangle,\ |\phi_2,\ n-1\rangle,\ |\phi_2,\ n\rangle. \tag{1.35}$$

The states including an absorption or emission of a photon ($n \pm 1$) are referred to as light-induced states. The reader is referred to [27] for a more detailed description.
The quantum mechanical description of the electromagnetic wave in form of an operator was necessary to introduce these dressed states. After the reduction to the above mentioned manifolds, a semiclassical representation, where the light field is described by its complex, time-dependent electric field, is sufficient:

$$\mathscr{E}(t) = \frac{\mathcal{E}_0}{2} \cdot \left[e^{i\omega_l t} + e^{-i\omega_l t}\right], \tag{1.36}$$

where $\mathcal{E}_0$ is connected to the field's amplitude and ω_l is its frequency. Furthermore, for energetically (nearly) degenerate states, which holds for these pairs of states: ($|\phi_1,\ n\rangle$, $|\phi_2,\ n-1\rangle$) and ($|\phi_1,\ n+1\rangle$, $|\phi_2,\ n\rangle$), the laser field introduces a coupling between those. Both pairs undergo the same coupling mechanism first described by Rabi in 1931 [28]. For that, the lower lying state of one of theses pairs is defined as $|\phi_m\rangle$ (with energy E_m) and the upper one as $|\phi_n\rangle$ (with energy E_n), respectively. They are separated in energy by the detuning of the laser field $\Delta \equiv (\omega_n - \omega_m) = (\omega_1 - \omega_2) - \omega_l$, where the mapping of the states depends on the sign of Δ. A general superposition state follows eq.(1.24):

$$|\Psi(t)\rangle = c_n(t)\ |\phi_n\rangle + c_m(t)\ |\phi_m\rangle. \tag{1.37}$$

The Hamiltonian of the two-level system, including the off-diagonal dipole-interaction term $d_{nm} \cdot \mathscr{E}(t)$ (with $d_{nm} = d_{12}$) can be written in the matrix-

formalism as:

$$\hat{\mathscr{H}}_{2level} = \begin{pmatrix} E_n & d_{nm} \cdot \mathscr{E}(t) \\ d_{nm} \cdot \mathscr{E}(t) & E_m \end{pmatrix}.$$

To solve the SEQ, eq.(1.22), of $\hat{\mathscr{H}}_{2level}$ analytically, the rotating-wave approximation (RWA) is applied on the time-dependent coefficients, defined as:

$$c_n(t) = \tilde{c}_n(t) \cdot e^{-i(\omega_n - \Delta/2)t}, \tag{1.38}$$

$$c_m(t) = \tilde{c}_m(t) \cdot e^{-i(\omega_m + \Delta/2)t}, \tag{1.39}$$

by neglecting the fast oscillation term $(\omega_n - \omega_m) + \omega_l$. The Hamiltonian acting on the coefficients $\tilde{c}_{n,m}(t)$ in the RWA is simplified to:

$$\hat{\mathscr{H}}^{RWA}_{2level} = \begin{pmatrix} \Delta & \Omega_R^{'} \\ \Omega_R^{'} & -\Delta \end{pmatrix},$$

where $\Omega_R^{'} = d_{nm}\mathcal{E}_0/\hbar$ accounts for the Rabi frequency. The eigenvalues of this matrix can be defined by introducing the generalized Rabi frequency Ω_R:

$$\lambda_{\pm} = \pm\frac{\hbar}{2}|\Omega_R| \equiv \pm\frac{\hbar}{2}\sqrt{\Delta^2 + |\Omega_R^{'}|^2}. \tag{1.40}$$

These eigenvalues can be used to characterize the new energy levels of the states E_n, E_m interacting with the monochromatic electromagnetic wave:

$$E_{n,m} \rightarrow E_{\pm} = \frac{E_m - E_n}{2} \pm \frac{\hbar}{2}\sqrt{\Delta^2 + |\Omega_R^{'}|^2}. \tag{1.41}$$

Going even one step further back to the definition of the manifolds $\mathscr{M}_n$, the four (approximated) states in eq.(1.35) are now precisely described by these coupled states, defined by their eigenenergies:

$$E_{|\phi_1,n\rangle},\ E_{|\phi_2,n-1\rangle} \rightarrow E_1^{\pm} = E_1 - \frac{\hbar\Delta}{2} \pm \frac{\hbar}{2}\sqrt{\Delta^2 + |\Omega_R^{'}|^2}\ , \tag{1.42}$$

$$E_{|\phi_2,n\rangle},\ E_{|\phi_1,n+1\rangle} \rightarrow E_2^{\pm} = E_2 + \frac{\hbar\Delta}{2} \pm \frac{\hbar}{2}\sqrt{\Delta^2 + |\Omega_R^{'}|^2}\ . \tag{1.43}$$

As shown in fig.(1.9), each pair of energies $E_{1,2}^{\pm}$ contains repulsive energy levels. The repulsion is known as Autler Towns or AC-Stark splitting [29] and increases with the laser fields intensity up to the limit $|\Omega_R| \ll |\Delta|$, where it increases linearly with the Rabi-frequency $\Omega_R^{'} \approx \Omega_R$ and therefore with the field's amplitude $\mathscr{E}_0$. This can be seen as dotted lines in fig.(1.9).

After clarifying the notation of the laser-coupled system's eigenenergies, a brief summary of the time-dependent population dynamics shall be added:
Per definition, eigenstates of the Hamiltonian are time-independent, their co-

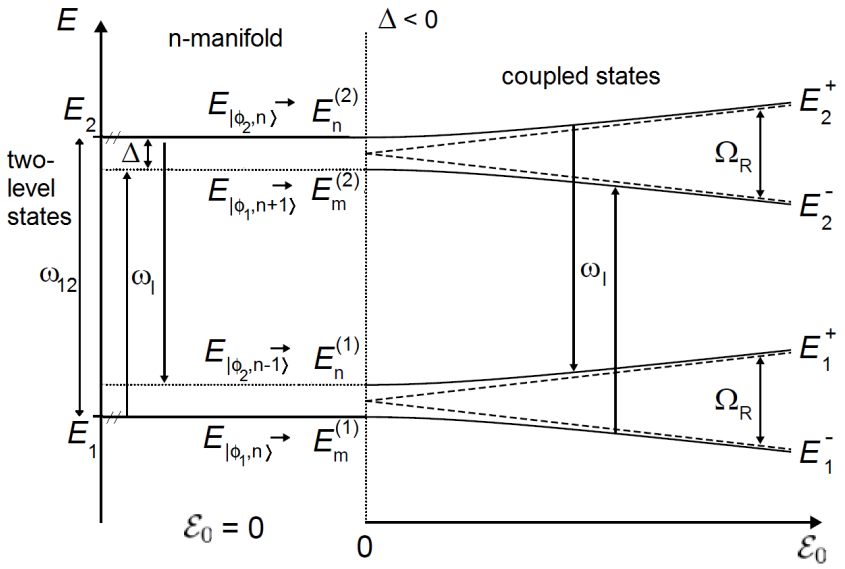

Figure 1.9.: **Rabi-coupling**
The interaction of a ligth field with a two-level system (unperturbed energy levels marked left from the energy axis) leads to creation of light-induced states. The states of the uncoupled case of $\mathscr{M}_n$ (in the weak-field limit) are shown in the middle panel, whereas the coupled states $E^{\pm}_{1,2}$ are plotted vs. the laser-fields's amplitude $\mathcal{E}_0$ right from the vertical dotted line. Fig. is adapted from [30].

efficents $c_{\pm}$ are constant in time. Thus, the dynamics are encoded into the population coefficients $\tilde{c}_{n,m}(t)$ of the non-diagonalized states in the RWA. The derivation will not be presented here, but follows the ideas in [31]. Their temporal evolution for the initial condition that only the ground state is populated ($\tilde{c}_m(0) = 1$, $\tilde{c}_n(0) = 0$) is characterized by the following two equations:

$$\tilde{c}_n(t) = -i\frac{\Omega_R'}{\Omega_R} \cdot \sin\left(\frac{\Omega_R t}{2}\right), \tag{1.44}$$

$$\tilde{c}_m(t) = \cos\left(\frac{\Omega_R t}{2}\right) + i\frac{\Delta}{\Omega_R} \cdot \sin\left(\frac{\Omega_R t}{2}\right). \tag{1.45}$$

One can find, that the population probabilities $|\tilde{c}_n(t)|^2$, $|\tilde{c}_m(t)|^2$ are oscillating in time between the two levels with the generalized Rabi-frequency Ω_R. For the resonant case, the excited state $\tilde{c}_n(t)$ can be even fully populated after half a cycle, before being completely depopulated again at the end of a cycle for $t = 2\pi/\Omega_R$. For non-zero detunings, the excited state never reaches complete population, but therefore the generalized Rabi frequency (following

eq.(1.40)) becomes larger. In any case, this behaviour differs greatly from any perturbation theory result, where usually the ground state is not that heavily depopulated. Only for detunings large enough, so that even the reduction to the manifolds in eq. (1.35) is not reasonable any more, the coupling of the states becomes negligible (as in the weak-field case) and the states in eq. (1.34) become the correct description of the light-matter-interacting system.

This section should be concluded with the remark, that large enough intensities for theses processes are experimentally reachable with laser pulses as introduced in chapter (2.1). On the other hand, the theoretical description in this chapter breaks down regarding the fact, that those laser pulses are short in time and hence not monochromatic. Although it is in general possible to describe this scenario analytically as well, e.g. with a time-dependent Rabi frequency, the treatment of this case is postponed to the numerical analysis presented in chapter (4).

1.5. Absorption Spectroscopy

In this final theory chapter the fundamentals of absorption and its consequences for spectroscopic investigations will be presented. The spectral absorption $[A(\omega)]$ of a medium is linked to its transmission $[T(\omega)]$ via:

$$A(\omega) = 1 - T(\omega) \ . \tag{1.46}$$

An incoming electromagnetic wave with intensity profile $I_{in}(\omega)$ interacting with the medium, e.g. a gas, will lead to an output signal $I_{out}(\omega)$, so that:

$$T(\omega) = \frac{I_{out}(\omega)}{I_{in}(\omega)} \ . \tag{1.47}$$

The output signal contains all of the interactions of the light field with the medium. They are encoded into the macroscopic polarization P, which is related to the dipole response d of a single atom via:

$$P(\omega) = \rho_N d(\omega), \tag{1.48}$$

where ρ_N is the atomic number density. For a dilute gas, propagation effects are negligible, so that P depends linearly on the driving electric field $E(\omega)$:

$$P(\omega) = \epsilon_0 \chi(\omega) E(\omega). \tag{1.49}$$

Here, ϵ_0 stands for the electric vacuum permittivity and $\chi(\omega) = \chi'(\omega) + i\chi''(\omega)$ stands for the dielectric susceptibility, which is given in complex notation for complex notations of P and E. It is connected to the refractive index n of the

medium by the relation: $n(\omega) = \sqrt{1+\chi(\omega)}$. In general, higher orders of E can be included in eq.(1.49), for example as in eq.(1.13). The reader is referred to [11] for more detailed information.
With these notations, a definition of the absorption cross section $\sigma_{abs}(\omega)$ can be derived. For that purpose, the propagation (in z direction) is described by Lambert-Beer's law

$$I_{out}(\omega) = I_{in}(\omega) \cdot \exp\left(-\rho_N \sigma_{abs}(\omega) z\right), \tag{1.50}$$

and is compared to the linear propagation of the corresponding electromagnetic wave:

$$E(\omega, z) = E(\omega, 0) e^{ik(\omega)z}, \tag{1.51}$$

under the assumption of a dilute medium. In that case, the approximation $n(\omega) \approx 1 + \chi'(\omega)/2 + i\chi''(\omega)/2$ holds. With the definition of the wave vector $k(\omega) = n(\omega) \cdot \omega/c$, eq.(1.51) can be rewritten as:

$$E(\omega, z) = E(\omega, 0) \ \cdot \ e^{i\frac{\omega}{c}(1+\frac{\chi'(\omega)}{2})z} \ \cdot \ e^{-\frac{\omega}{c}\frac{\chi''(\omega)}{2}z}, \tag{1.52}$$

where the second term is related to the dispersion of the medium and the third one to its absorption. The comparison of eq.(1.50) and eq.(1.52) leads to the desired relation of the absorption cross section σ_{abs} to the dipole response d:

$$\exp\left(-\rho_N \sigma_{abs}(\omega) z\right) = \exp\left(-\omega \chi''(\omega) z/c\right) \tag{1.53}$$

$$\Leftrightarrow \sigma_{abs}(\omega) = \frac{\omega}{c}\frac{\chi''(\omega)}{\rho_N} = \frac{\omega}{c\epsilon_0}\mathrm{Im}\left\{\frac{d(\omega)}{E(\omega)}\right\}, \tag{1.54}$$

where in the last step equations (1.48) and (1.49) have been used. From here, the connection to the optical density (OD) can be found for a propagation over length l:

$$\mathrm{OD}(\omega) = \log_{10}\left(\frac{I_{sig}(\omega)}{I_{ref}(\omega)}\right) = \sigma_{abs}(\omega)\frac{\rho_N \ l}{\ln(10)}. \tag{1.55}$$

In a absorption spectroscopy (AS) experiment as presented in chapter (5), both quantities I_{ref} and I_{sig} are individually measurable, so that the OD can be calculated afterwards. There, I_{sig} refers to the superposition of the driving electric field and the induced emission based on the polarization. The exact formula can be derived from a microscopic time-domain perspective, which is consistent with the previous absorption-process frame. The reader is referred

to [32] for further information. As a result, the OD can be written in form of:

$$\mathrm{OD}(\omega) = \log_{10}\left(\frac{|E(\omega) + i\eta\ d(\omega)|^2}{|E(\omega)|^2}\right), \tag{1.56}$$

where η is connected to the number of atomic emitters and $\eta \ll 1$ is assumed to hold for a dilute medium. The formulation of the OD in eq.(1.56) has two benefits: First, to calculate the absorption by an atom for a given electric field only the dipole response has to be known. This fact will be used in chapter (4) for the numerical analysis.
Furthermore, equation (1.56) gives insight into the physics taking place in an absorption process: In an AS experiment, the incoming light wave and the dipole response of the target interfere with each other. Thus, the measured OD contains the superposition of the outgoing wave compared to the reference wave. This interferometric picture explains how absorption spectroscopy can extract phase information of the atom under investigation. This becomes even more important, when pulses in the strong field regime are utilized, which are capable of driving nonlinear processes, for example Rabi coupling (section (1.4.4)), or inducing a ponderomotive energy shift (equation (1.16)). These kind of absorption spectrosocopy will be referred to as strong field spectroscopy (SFS) in this thesis. An notable example is the relation between the phase shift $\Delta\phi$ of the temporal dipole moment $d(t)$ and the q-parameter of the corresponding spectral Fano-line profile introduced in section (1.4.3) [33]:

$$q(\Delta\phi) = -\cot\left(\frac{\Delta\Phi}{2}\right), \tag{1.57}$$

$$\Leftrightarrow \Delta\phi(q) = 2\ \arg(q - i). \tag{1.58}$$

With intense and short enough laser pulses, as introduced in section (1.1) and (1.3), the absorption profile of resonances can be manipulated as shown in fig.(1.10). There, after the excitation with a weak, delta-like (infinitely short) XUV pulse, the line-shape is changed with the help of an intense IR pulse, perturbating the decay of the dipole response. Note, that the IR pulse has to be short enough to be regarded as impulsive as well.

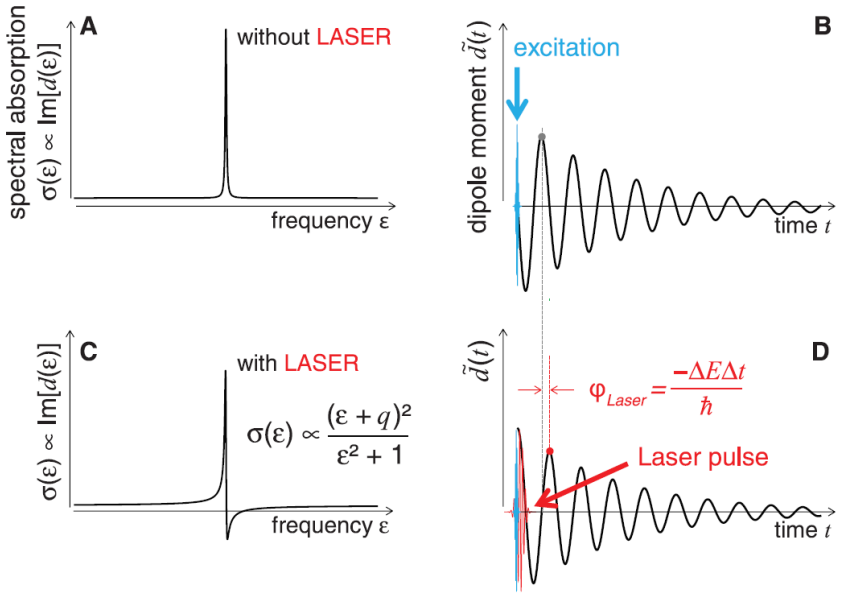

Figure 1.10.: **Dipole-phase control manipulating resonance line-shapes** The Lorentzian resonance line-shape in (**A**) emerges from a temporal oscillating and exponentially damped dipole moment (**B**). The process is initiated by a short and weak XUV pulse (blue), which can be generated for example in a HHG process. As the pulse duration is much smaller than the life time of the dipole response, the excitation can be regarded as instantaneous. Adding a short and intense IR pulse (red) leads to a phase shift of the dipole moment in the time domain (**D**). Following equation (1.58), the spectral line-shape will change to a Fano-profile as presented in (**C**).
Figure adapted from [33].

2. Experimental Apparatus

2.1. The Laser System

From the invention of the laser in 1960 [34, 35] to optical parametric amplification in 1965 [36, 37], chirped pulse amplification (CPA) in 1985 [38] and the first mode-locked Titan:Sapphire (Ti:Sa) laser in 1991 [39] as well as experimental HHG demonstration in 2001 [15], there is a long list of outstanding laser (pulse) developments, on which the here presented apparatus is based on. The heart of it is the commercial laser system, presented in this section, whereas the existing homebuilt vacuum setup for absorption spectroscopy, simply called 'beamline', will be shortly introduced in the next section.
As a first step within this thesis project, the *Coherent: Cryo SPA* [40] laser system was installed. It consists of a Ti:Sa oscillator with carrier-envelope phase (CEP) stabilization, a three-stage CPA amplifier (regenerative amplifier (*regen*), conventionally cooled single-pass amplifier (SPA) and cryogenic SPA (*cryo*)) and the *HE-TOPAS-Prime-Plus* optical parametric amplifier (OPA) delivered by *Light Conversion* [41]. A scheme of the laser system can be found in fig.(2.1), whereas a more detailed drawing containing the beam path is added in the appendix (fig.(A.1)). The single components are described below. Due to the multiple amplification stages, the system possesses several pulse outputs. The main ones are the two cryo outputs, depicted as high energy (HE) and low energy (LE) outputs, respectively, and the TOPAS outputs. The following table summarizes their key parameters:

pulse	λ_c	f_{rep}	E_{pulse}	τ_p	M^2
Cryo:	800 nm	1 kHz	<27 mJ		
HE	800 nm	1 kHz	<22 mJ	$\sim$ 27 fs	1.55
LE	800 nm	1 kHz	<10 mJ	$\sim$ 26 fs	1.24
OPA:	(1160-2600) nm	1 kHz	<6.7 mJ		
signal	(1160-1600) nm	1 kHz	<4.4 mJ	33-36 fs	-
idler	(1600-2600) nm	1 kHz	<2.3 mJ	< 50 fs	-

Table 2.1.: Properties of the laser system
λ_c stands for the central wavelength, f_{rep} for the repetition rate, E_{pulse} for the pulse energy, τ_p for the pulse duration and M^2 quantifies the beam quality.

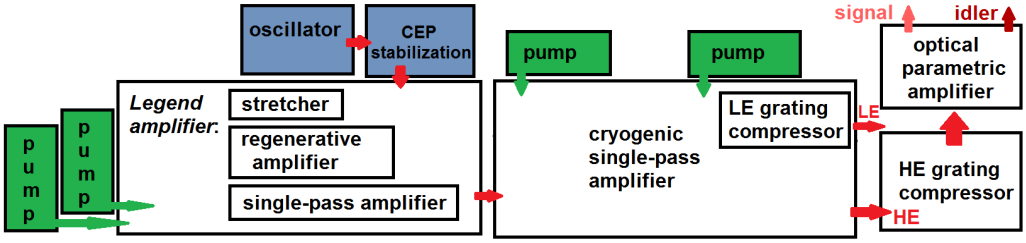

Figure 2.1.: **Laser system - scheme**
Oscillator and CEP stabilization are coloured in blue. The beam path is marked with red arrows for the output pulses and green ones for the pump lasers. The *Coherent: Legend Elite Duo HE+* amplifier (left black box) contains the initial stretcher for CPA and the two first amplification stages (regen and SPA). The third amplification takes place within the cryogenic SPA (right box), after which the pulse is split into the LE and HE output. The LE output is compressed within the cryo box, whereas the HE pulse is compressed afterwards externally. The TOPAS is driven by the HE pulse, generating signal (light red) and idler (dark red).

The pulse generating process starts within the oscillator. The Ti:Sa crystal is pumped optically generating many lasing modes. If *mode-locked* due to the nonlinear effect called Kerr-lensing, the coherent superposition of modes leads to a pulsed laser output, containing fs-pulses centred at $\sim$ 800 nm with a repetition rate of 80 MHz and $\sim$ 0.5 W optical output power. The reader is referred to [39, 42] for a more detailed description of mode-locking.
These output pulses are CEP stabilized before being amplified. The CEP stabilization is achieved by measuring a beat note, the carrier envelope offset frequency, which is back-looped with an AMO to the oscillator [43]. As it runs with a low intensity transmission of the laser, the system can also operate without active oscillator CEP stabilization in a CEP-averaged mode.
Afterwards, the pulses are amplified by the method of *chirped pulse amplification* [38] as presented in fig.(2.2): The seed pulse is linearly chirped by a pair of gratings and stretched in time following eq.(1.11) to upto 150 ps. Being dispersed in time and therefore reduced in peak intensity, it can be amplified within another Ti:Sa crystal by several orders of magnitude without exceeding the damage threshold of the involved optical elements. The first amplifier is a regenerative one, which means the pulses resonates several times through the crystal until it has accumulated the maximum possible amplification, leading to a pulse energy of $\sim$ 6.1 mJ at a reduced repetition rate of 1 kHz. Within the second stage, the pulse depopulates all the population inversion in the lasing medium within a single passage. The pulse energy can be more than doubled to $\sim$ 13.1 mJ. Further amplification requires enhanced cooling of the amplifi-

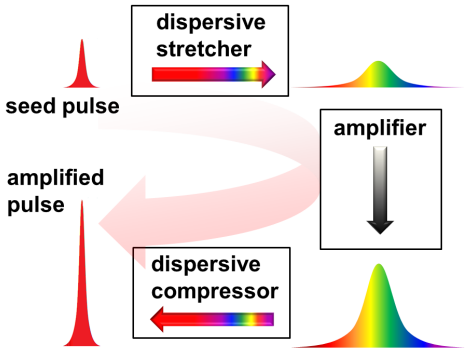

Figure 2.2.: **Chirped Pulse Amplification**
A chirped laser pulse is stretched in time and damped in intensity allowing for amplification before compression.

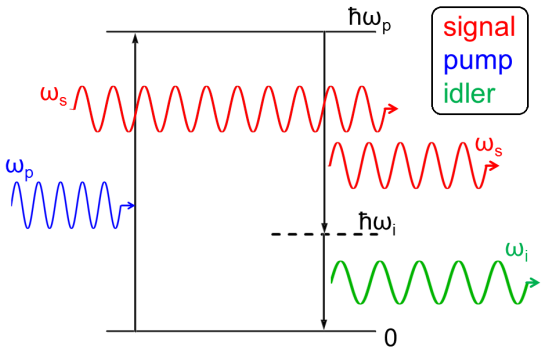

Figure 2.3.: **Optical Parametric Amplification**
The χ^2-process allows to generate two photons (signal and idler) out of the initial pump photon obeying eq.(2.1).

cation crystal, which is given in the third stage at a temperature T $\sim$ 110 K in a vacuum of p $\approx 3\ 10^{-8}$ mbar. In this third *cryo* amplifier the pulse energy is maximized reaching $\sim$ 26 mJ, before the pulse is split by a polarising beam splitter and an adjustable half-wave plate into the low (LE, $E_{pulse} \leq 10$ mJ) and high energy (HE, $E_{pulse} \leq 22$ mJ) output. Last, both pulses are compressed (the LE pulse within the third amplifier, whereas the HE in a separate external compressor) with a pair of gratings, respectively, removing the initially added chirp. The rotation of the gratings and their separating distance can be optimized for minimal GDD and TOD, respectively. Hence, the pulses are as close as possible to the FT-limit at the compressor exit or even can be pre-compensated for minimal pulse duration after a certain amount of beam path (in air, glass, etc.). Plots of the pulses' spectra are presented in the pulse characterization chapter (3).

Additionally, an optical parametric amplifier (OPA) [44] is used to shift the central wavelength of the HE pulses within the near infrared (NIR: 780 nm - 1400 nm) and to the short-wavelength infrared (SWIR: 1400 nm - 3000 nm) regime. A four wave-mixing process in a nonlinear BBO crystal as presented in fig.(2.3) is the basis of this χ^2-process: The HE pulse is exploited as pump pulse (blue) interacting non-collinearly with a signal photon (red) and decaying into an additional signal photon and a residual idler photon (green), obeying energy and momentum conservation:

$$\omega_p = \omega_s + \omega_i, \qquad \vec{k}_p = \vec{k}_s + \vec{k}_i. \tag{2.1}$$

The signal beam is a spectrally extremely broadened, low intensity copy of the pump pulse. A time-delay variation between signal and pump pulse changes the chirp-induced time-delay dependent spectral region of the signal pulse, with which the pump coincidences in time and hence determines the central frequency of the signal. The installed *TOPAS-PRIME-Plus* consists of three sequential OPA stages, in total reaching ~ 6.7 W combined signal and idler output power, if it is driven with the optimal pump power of 18 W (efficiency = 37.2%).
The SWIR wavelength regime as well as the central wavelength tunability promises more versatile experimental capabilities, but also implicates more complicated experimental issues, as the SWIR region demands technically more advanced and expensive characterization devices. For example, the beam profile in form of a M^2-measurement has not been feasible, thus the corresponding values are missing in tab.(2.1). The optical feedback of the beam mode due to THG in the BBO crystal is only partially reliable, but presents an inhomogeneous, yet to optimize profile. On the other hand, the temporal characterization of all, including the OPA pulses was carried out successfully with the FROG measurements presented in chapter (3).

2.2. The Beamline

The homebuilt 'beamline' for XUV SFS experiments in vacuum was build as part of the thesis projects [45–47] and has been improved several times since then. The setup is designed to be transportable and to be used with different laser sources, e.g. from the one presented in the previous section to larger facilities as free-electron lasers. Thus, the beamline is located outside of the laser laboratory leading to a long beam path ($\sim$ 10 m) of the pulses. For first experiments only the TOPAS signal beam is used, hence temporal pulse broadening due to the accumulated chirp in air is less pronounced compared to Ti:Sa pulses, because the GDD is smaller in the SWIR regime. As the beamline is essential for the AS experiments presented in chapter (5), it will be introduced briefly in the following (see fig.(2.4)):

- The first step is the HHG, as introduced in sec.(1.3). The OPA signal pulse is focused with an $f = 1$ m concave mirror into the HHG cell, where different rare gases are used at a backing pressure of several hundreds of mbar. The resulting HHG spectra are presented in section (5.1). The driving OPA pulse propagates collinearly with the generated XUV pulses and is reused as a perturbation pulse in the target cell (maintaining the design of [30]). With the subsequent aluminium filter set, the SWIR pulse can be blocked completely for alignment reasons or alternatively a half-moon aluminium filter blocks one vertical half of the pulse for pump-probe experiments.

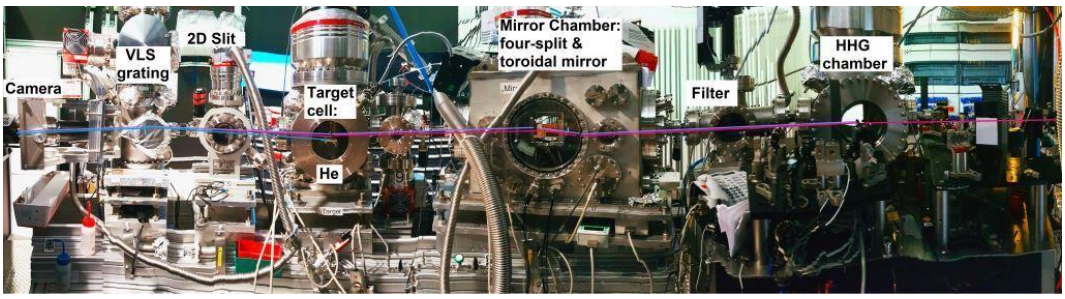

Figure 2.4.: **Picture of the Beamline**
The SWIR laser pulse (red arrows) enters the beamline from the right after being guided out of the laser laboratory. It is focused into the first chamber, generating high harmonics (violet). Both, SWIR and XUV pulses, are refocused with a toroidal mirror placed in the mirror chamber. Their time delay is controlled with a split mirror. In the target cell, helium gas interacts with the laser pulses emitting its dipole response as additional XUV light (blue). The spectrometer translates these temporal information into high-resolution spectra measured by the camera chip.

- Further downstream, the mirror chamber contains a toroidal mirror in $2f - 2f$ geometry focusing the beam with $2f = 1$ m under an angle of incidence of 8° followed up by a four-split-mirror for splitting the beam. In general, the four-split-and-delay mirror allows for four-wave mixing experiments and two-dimensional spectroscopy. Here, the complete beam mode is put on two mirrors only, delaying (half) the XUV pulse (lower half, where the SWIR is blocked beforehand) with respect to (half) the SWIR pulse (transmitted by the half-moon filter). The additional XUV pulse on the SWIR mirror cannot be blocked, though its influence on the target can be neglected [30]. The spatial overlap of the two refocused beams can be maintained over the whole travelling range (250 $\mu m \approx$ 200 fs) of the sub-μm/sub-fs precise *HERA* delay stage with help of *Piezo* actuators and a *tip-tilt* correction adjusting the angles of the two individual mirrors.

- The target cell is a nearly identical copy of the HHG ceramic cell, with a slightly larger entrance window (300 μm diameter instead of 150 μm). It is placed in the refocusing spot $2f = 1$ m after the toroidal mirror. The chamber is designed to allow for target-gas backing pressures p of up to 1 bar. For the in this thesis investigated target gas, helium, $p \sim 80$ mbar is used.

- For recording the transmitted absorption spectra, the XUV spectrometer, consisting of a variable line space (VLS) grating and a *Princeton Instru-*

ments PIXIS CCD camera [48], as described in [30, 33] is installed. The spectral resolution is in the order of $E/\Delta E \sim 1000$ and can be adjusted with a two-dimensional entrance slit in front of the VLS grating, balancing between maximized spectral resolution and XUV flux on the CCD chip. A 400 nm aluminium filter after the 2D slit prevents the SWIR pulses from damaging the camera chip.

3. Frequency-Resolved Optical Gating Measurements

3.1. FROG Setup

The laser pulses produced by the system described in the previous chapter (2.1) can be characterized with the FROG method introduced in section (1.2). Therefore, a portable TG-FROG, based on the implementation described in [49], was built as one of the main tasks of this thesis project and is presented in the following.

A picture of the FROG setup can be found in fig.(3.1): After aligning the input beam onto the two iris apertures, the beam is redirected onto the split-and-delay unit. There, two horizontally aligned D-mirrors split the beam into two parts. The upper mirror can be moved against the other one, controlled by a piezo-based stick-slip stage [50]. The sub-μm precision on a mm-scale traveling range give rise to very precise control of the resulting time delay between the two beams. Afterwards, the beams are separated by a four-hole mask into four identical beam copies, with each pair of them having the exact same time delay. An aperture between the second iris and the split-mirror is designed to block one of the four beams, if put in, or alternatively let that beam through as an alignment reference, if put out. The four-hole mask is mounted right in front of a focusing mirror with focal length $f = 20$ cm, focusing the beams into a fused silica glass plate of 100 μm thickness, in which the nonlinear signal-generating process is driven. Alternatively, a deflection mirror can be inserted before the glass plate, focussing the beams onto a camera chip for determination of the spatial and temporal overlaps before the measurement. After the target glass plate, the beams are redirected onto a collimating mirror. The generated signal beam is separated from the other three beams with help of an additional aperture. The signal/reference beam is coupled via a fibre into an *OceanOptics FX* spectrometer, exchangeable to other spectrometers depending on the wavelength region of the pulse to be measured.

The combination of a variable spectrometer choice, as the setup is not limited to a specific wavelength region by phase matching criteria and the fine time steps on a large total travelling range of the stages and split-mirrors, leads

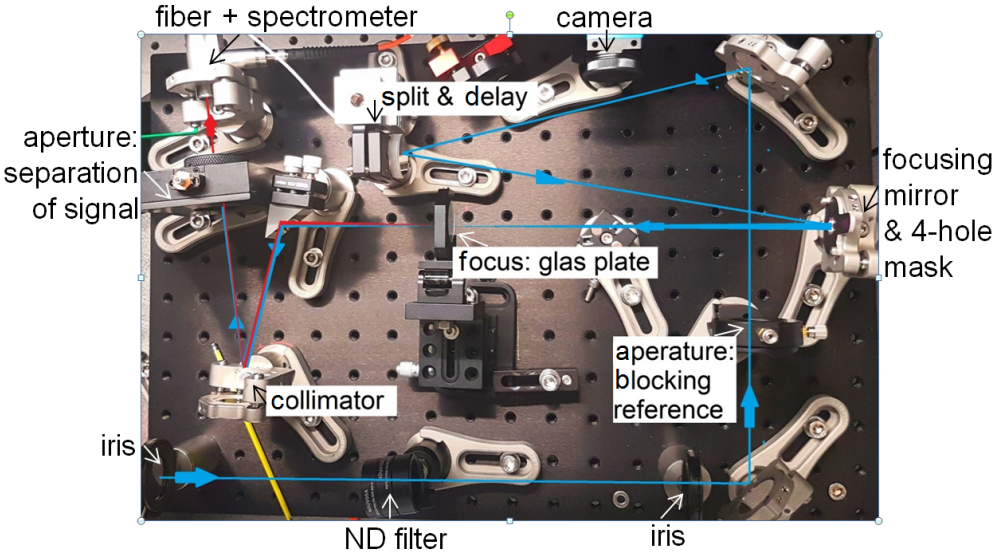

Figure 3.1.: **TG-FROG setup**
The beam path of the pulse to be characterized by the TG-FROG setup is depicted in blue, entering at the lower left corner. The optical elements are mostly labelled in the picture. The three without labels are simple deflection mirrors. The generated signal beam is coloured in red. A detailed explanation of this setup can be found in the text.

to a universal pulse-measurement apparatus, capable of characterizing all the different pulses (varying in pulse duration and spectral region over orders of magnitude) produced by the laser system (sec.(2.1)). Additional, only a thin glass target is inserted as optically transmitting element, distorting the pulses during the characterization as least as possible.

3.2. Ti:Sa Pulse Measurement and Comparison to SPIDER

First, the characterizations of the two Ti:Sa output pulses, HE and LE (see section (2.1)), are presented in this section. Both of them have been characterized with the homebuilt TG-FROG setup as well as with a commercial SPIDER-measuring device, provided by the laser installing company. As the SPIDER measurement was not part of this thesis project, only the results in form of the retrieved temporal pulse and the in-situ measured FT-limited pulses (by FT of the spectrum) shall be presented here for comparison.

Before the FROG data can be retrieved, a proper noise filter has to be em-

ployed, following the steps of [51]:

- First, a 100×100 pixel square in the corner of the raw 2D data set is defined as background. The mean value is subtracted from the whole image.
- A corner suppression is carried out by multiplying the spectrogram with a radial symmetric two-dimensional super-Gaussian.
- After employing a 2D-FT of the data set, multiplication with a Fourier-filter and back FFT eliminates the high-frequency noise.
- The prepared trace is loaded into the commercial FROG retrieval algorithm software *Frog3* by *Femtosoft Technologies*, where the central part of the spectrogram is cut out and binned on a 256×256 grid.
- Last, the time axis is interpolated to a larger time step (mostly 2 fs), to keep the Fourier-relation between the time and frequency axis valid. The new time step is chosen to achieve a equally sized spectrogram in both dimensions (see [51] for further information).

The results of the retrieval are plotted in fig.(3.2) and (3.3) for the HE and LE pulse, respectively. In general, the retrieval is seen to be successful, when for the *FROG G-error*, the rms error between experimental and retrieved 2D data set: $G \leq 1\%$ holds. With values of $G_{HE} = 0.82\%$ and $G_{LE} = 0.93\%$, and a qualitatively good agreement between experimental and retrieved FROG trace in a) and b) of fig.(3.2),(3.3), respectively, the pulses of the HE and LE output were retrieved with an excellent quality.
Both pulses exhibit a circular maximum in their spectrogram, which is surrounded by more complex substructures. The retrieved temporal amplitudes thus look Gaussian-like in fig.(3.2),(3.3) c), respectively, with some additional pre- and post-pulses on the order of $\leq 10\%$ intensity-wise. The temporal phases of both pulses in fig.(3.2),(3.3) c), respectively, are therefore mostly flat around the main pulse and more complicated further outside.
For the comparison to the SPIDER measurement, the temporal retrieved intensities of the FROG and SPIDER measurement as well as the FT-limited pulse are plotted in d) of fig.(3.2),(3.3), respectively for the HE and LE pulse. The FROG retrieved amplitude is in excellent agreement with the SPIDER measurement for the HE pulse and reasonably well around the main peak for the LE pulse. All three amplitudes in both figures d) are fitted with a Gaussian envelope to determine the FWHM of the temporal profiles, converting the standard deviation of the Gauss-fit with help of eq.(1.8). The results are summarized in tab.(3.1).

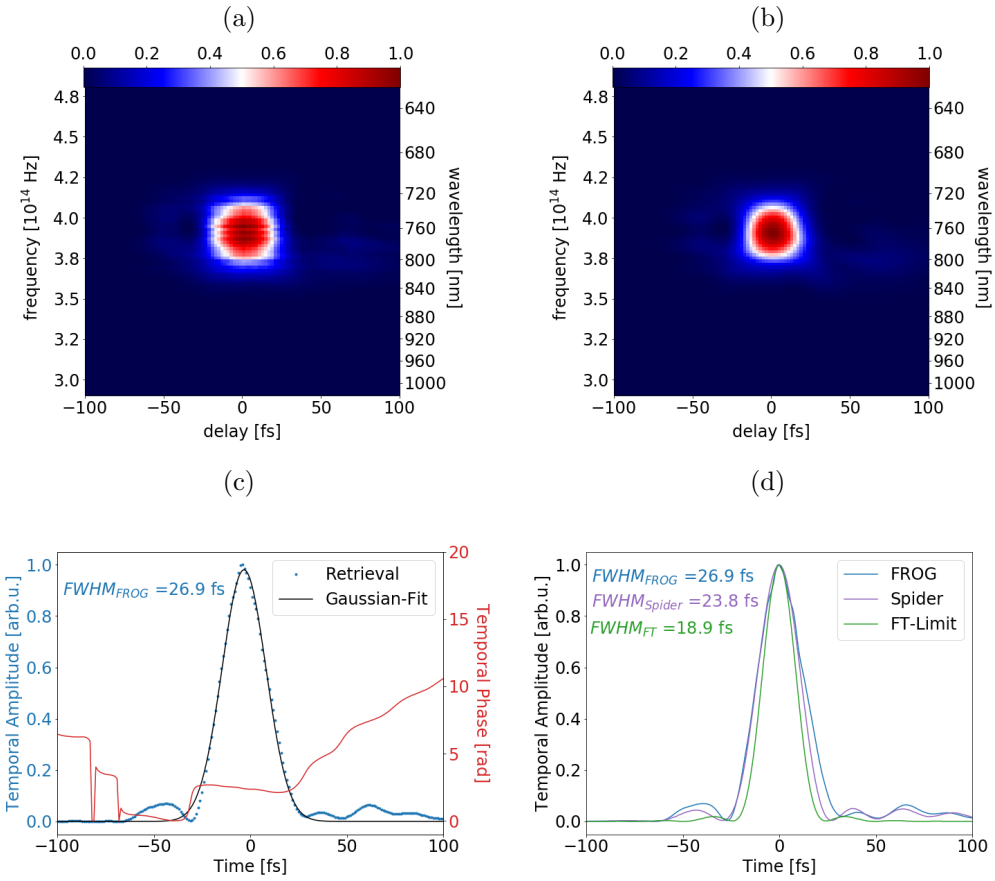

Figure 3.2.: **Retrieved FROG measurement of the HE pulse**

The figure shows: (a) Noise-filtered cut-out of the experimental trace. (b) retrieved trace. (c) temporal amplitude (blue) and phase (red), as well as Gaussian-fit of the amplitude for determining the pulse duration. (d) Comparison of the FROG (blue) and SPIDER retrieved (violet) temporal amplitudes to the FT-limit (green).

pulse	$\mathrm{FWHM_{FROG}}$ [fs]	$\mathrm{FWHM_{SPIDER}}$ [fs]	$\mathrm{FWHM_{FT\text{-}limit}}$ [fs]
HE	26.9	23.8	18.9
LE	26.1	23.4	18.2

Table 3.1.: FWHM of FROG vs. SPIDER measurements and Fourier-limits

Additionally, plots of the FROG retrieved spectra as well as the full temporal pulse characterizations of the SPIDER measurements are plotted in fig.(B.1),(B.2) in the appendix. Several conclusions can be drawn with the help of the comparison in tab.(3.1): As the HE and LE outputs should be

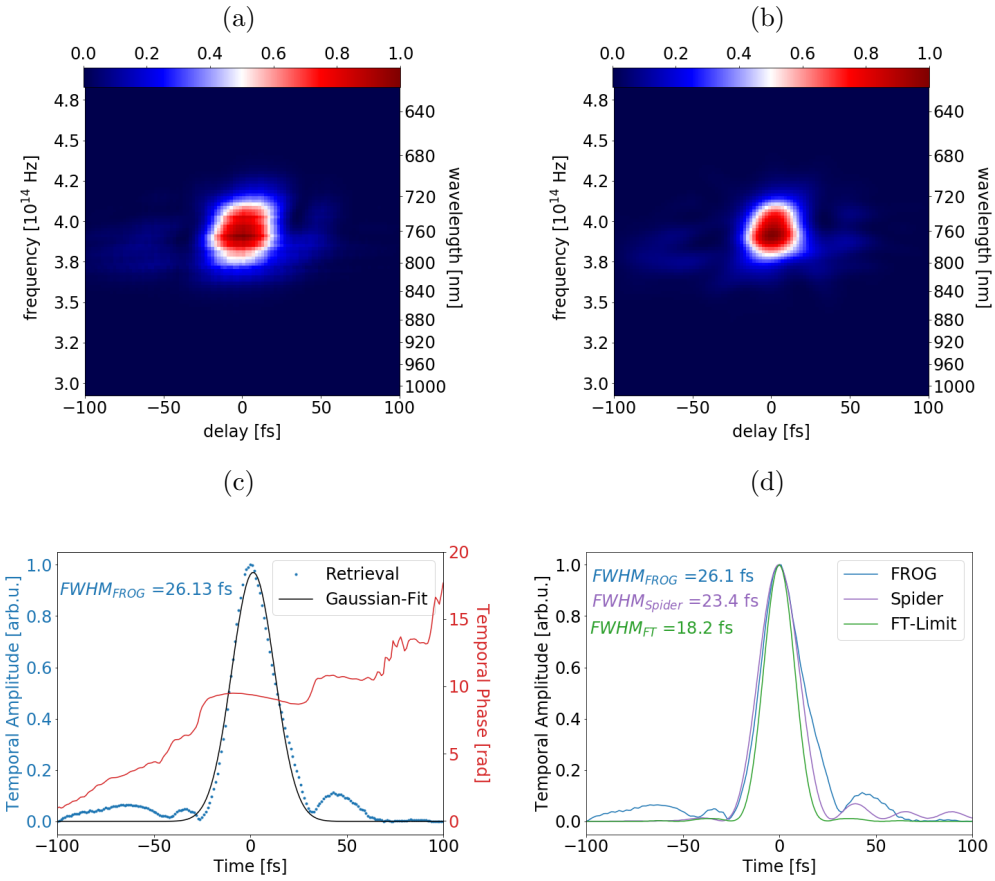

Figure 3.3.: **Retrieved FROG measurement of the LE pulse**

The figure is structured in the same manner as fig.(3.2), but contains the data of the LE pulse measurement.

identical copies of each others, disturbed by different compressors, collimated beam sizes and beam paths, it is reasonable, that the results in fig.(3.2) compared to fig.(3.3) as well as the estimated FWHM of the first row of tab.(3.1) in comparison to the second one are close to identical. Furthermore, both FROG and SPIDER retrievals yield values for the pulse duration larger than the FT-limit, which is also expectable as the pulses are not perfectly isolated, but contain pre- and post-structures. In addition, the FWHM values of the SPIDER measurements are slightly smaller than the FROG results, but a concrete comparison lacks a precise determination of the errors. By repeating the FROG algorithm on the same data set and additionally varying the retrieval input parameters slightly (e.g. noise filtering and cut-out region), the main numerical error for $\mathrm{FWHM_{FROG}}$ can be estimated to $\sim 10\,\%$. As the SPIDER error can be guessed to be on the few-percent level as well [9], the results of

the two different characterization methods agree well to each other within their error margins.

3.3. Pulses from the Optical Parametric Amplifier

In analogy to the procedure for the Ti:Sa pulses in the previous section, the TOPAS pulses were characterized as well. For that purpose, the *Ocean Optics FX* spectrometer is exchanged with an InGaAs based *Ocean Optics NIR Quest* spectrometer to measure in the SWIR region (1200 nm - 2000 nm). As the current setup, described in section (2.2), is used for experiments with the signal output of the TOPAS, a set of three signal pulses were characterized, with central wavelengths: $\lambda_c \sim 1300$ nm, $\lambda_c \sim 1400$ nm and $\lambda_c \sim 1500$ nm. The intrinsic TOPAS settings for maximized output power at this wavelengths can be found in tab.(B.1) in the appendix. Besides the FROG measurements of those pulses, independent spectra were recorded to estimate the FT-limit. As the comparison of the Ti:Sa pulses to their corresponding SPIDER measurement already exhibits reasonably well results, no further SPIDER characterisation was carried out.
The retrieval results are presented in fig.(3.4), whereas the experimental and retrieved FROG traces can be found in the appendix, in fig.(B.3). The G-errors, $G_{1300nm} = 1.5\%$, $G_{1400nm} = 1.1\%$, $G_{1500nm} = 0.95\%$, are acceptable, yet improvable. As presented in the right column of fig.(3.4), the spectra recorded with the independent reference differ from the spectra measured with the FROG apparatus. Note, that this spectral shifts can already be found in the experimental traces (in fig.(B.3)). Therefore, the spectral changes have to be connected to the spatial chirp of the pulses manifesting in the FROG measurement due to the use of the four-hole mask (see sec.(3.1)). The inhomogeneous beam mode discussed in chapter (2.1) can be regarded as cause for this outcome. An expected improvement of the TOPAS performance should overcome this problem. Despite that, the spectral changes manifest mostly in a shifted central wavelength λ_c, and somewhat in the shape of the spectrum. But as table (3.2) shows, the spectral FWHM, obtained by Gaussian fits, are varied just a few percent:

Position & FWHM	$\lambda_c \sim 1300$ nm	$\lambda_c \sim 1400$ nm	$\lambda_c \sim 1500$ nm
$\lambda_{c,\,\mathrm{FROG}}$ [nm]	1321	1446	1470
$\lambda_{c,\,\mathrm{reference}}$ [nm]	1304	1417	1498
$\mathrm{FWHM}_{\mathrm{FROG}}$ [nm]	100.1	96.5	81.7
$\mathrm{FWHM}_{\mathrm{reference}}$ [nm]	114.6	95.2	85.0

Table 3.2.: Spectral properties of the three TOPAS signal pulses

The larger deviation for the 1300 nm FWHM is due to the spectral 'shoulder' leading to different Gaussian fits. Nevertheless, the corresponding temporal retrievals should not be affected heavily by a spectral shift. Again, the temporal intensities and the FT-limited envelopes were Gaussian-fitted to obtain the temporal FWHM, presented in tab.(3.3):

FWHM	$\lambda_c \sim 1300$ nm	$\lambda_c \sim 1400$ nm	$\lambda_c \sim 1500$ nm
$\text{FWHM}_{\text{FROG}}$ [fs]	34.0	33.3	35.6
$\text{FWHM}_{\text{FT-limit}}$ [fs]	28.5	28.2	30.6

Table 3.3.: FWHM of three TOPAS signal pulses compared to their FT-limits

The three values of the FWHM of the FROG retrievals in tab.(3.3) match each other within a $< 10\%$ tolerance. The temporal intensities of these pulses in fig.(3.4) are comparable to each other in terms of their main pulse shape, but show different pre- and post-pulse behaviours. As these surrounding temporal substructures are relatively smooth, the presented results are fine for a first characterization measurement without TOPAS performance optimization.
A comparison of the FT-limits proves that the pulse durations are $\sim 20\%$ longer than the FT-minima. This goes together with the spectral phase behaviour presented in fig.(3.4), as none of the pulses is completely flat in phase. The $\lambda_c \sim 1300$ nm - pulse is clearly linearly chirped, which also leads to a tilted peak in the spectrogram in fig.(B.3) (compare theory chapter, fig.(1.3)) and the most pronounced temporal 'shoulder'. Note, that the temporal and spectral phases far away form the centres, where the intensities vanish, are not well defined and are thus meaningless.
On top, reference values for the TOPAS pulse durations are estimated by the TOPAS manufacturer to be around $\sim 50\%$ higher than the driving Ti:Sa pulses, what is supported by the TOPAS FT-limits being nearly that amount larger than the driving pulses. The OPA pulse durations can be expected to be around $(26 - 27)$ fs $\times$ 1.5 $\approx$ 40 fs (compare tab.(3.1) to tab.(3.3)). As all of the measured FWHM are smaller than this benchmark, the temporal properties of the TOPAS pulses met within their specifications. Yet, it should be noted, that these values are not completely precise, as the temporal pre- and post-structures are not encountered in the FWHM calculations.

Overall, the FROG retrievals of all the measured pulses are judged to be fine with respect to the expectations. In particular, as the TOPAS pulse characterization was carried out after a beam path of ~ 10 m, these results are excellent and good enough for conducting first experiments, which are presented in chapter (5).

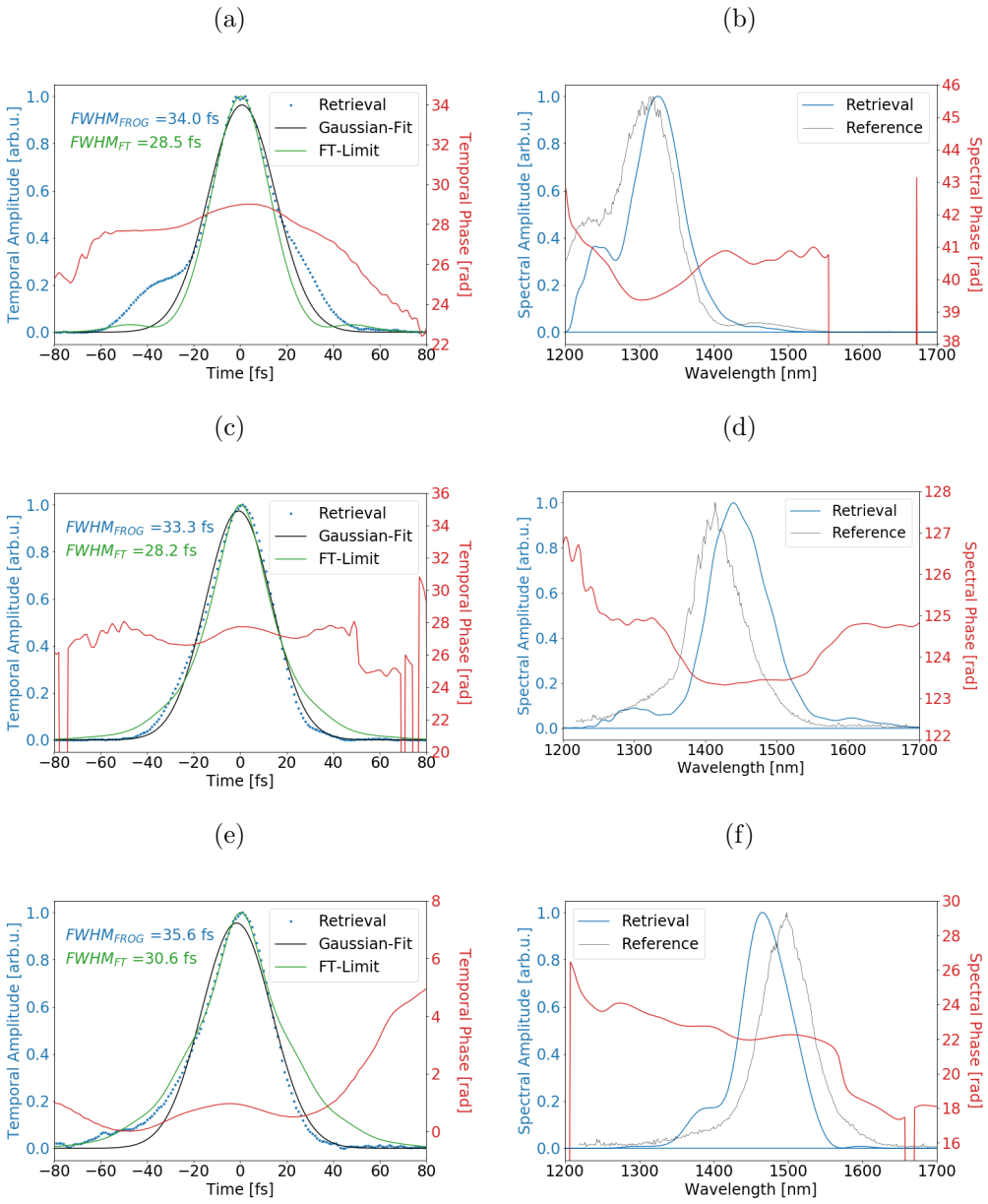

Figure 3.4.: **Retrieved temporal and spectral profiles for three different TOPAS signal pulses**
In the figure are plotted: left: temporal pulse profile and FT-limit, right: spectral pulse profile for a TOPAS pulse centred around:
(a),(b): $\lambda_c \sim 1300$ nm, (c),(d): $\lambda_c \sim 1400$ nm, (d),(e): $\lambda_c \sim 1500$ nm.

4. Numerical Analysis

4.1. Simulation Methods

4.1.1. Few-Level Model

For a complete understanding of the quantum dynamics under investigation a theoretical model is essential. As an analytical description is most often not available, numerical approaches are necessary. In this work, a numerical *few-level model* is employed which includes all relevant coupling pathways of the helium atom driven by near infrared and extreme ultraviolet laser fields. It is formulated in time and energy domain without detailed knowledge about the spatial degrees of freedom within the analysed helium atom.
For the few-level model to be implemented, it is necessary to have a given set of N eigenenergies and the corresponding couplings between them, which are sufficient to describe all the involved dynamics driven by a light field with classical electric field amplitude $\mathscr{E}(t)$. If this is the case, the Hamiltonian $\mathscr{H}$ of the system can be formulated as presented in chapter (1.4) in form of an N×N-matrix. Its diagonal contains the eigenenergies and the off-diagonals the couplings (in dipole approximation: $d \cdot \mathscr{E}(t)$, compare eq.(1.4.4)). The SEQ, eq.(1.22), can then be formulated on a discrete time grid (with size M). The resulting eigenvalue problem is solved to obtain the time propagation of the system for every time step Δt. It is propagated in its diagonalized Hilbert space, by applying the unitary transform matrices U and $U^T = U^{-1}$ to obtain the diagonalized Hamiltonian $\mathscr{H}_D$:

$$\mathscr{H}_D = U^T \mathscr{H}\ U. \tag{4.1}$$

The diagonal of $\mathscr{H}_D$ corresponds to the set of eigenvalues $\left\{E_n^D\right\}_{n\in N}$, whereas the columns of U are the eigenstates $\left\{|\Psi_n^D\rangle\right\}_{n\in N}$. If $|\Psi\rangle = [c_1, c_2, .., c_N]$ constitutes the initial state of the system, it can be transformed into the diagonalized Hilbert space via:

$$|\Psi_D\rangle = U|\Psi\rangle = \sum_n c_n^D\ |\Psi_n^D\rangle = \left[c_1^D, c_2^D, .., c_N^D\right]. \tag{4.2}$$

There, the time propagation of the eigenstates is given in terms of a phase evolution (as in eq.(1.23)):

$$|\Psi_n^D(x, \Delta t)\rangle = e^{-iE_n^D \Delta t/\hbar} \cdot |\Psi_n^D(x)\rangle. \tag{4.3}$$

Applying U^T leads to the solution propagated in time by Δt in the original Hilbert space:

$$|\Psi(\Delta t)\rangle = U^T |\Psi^D(\Delta t)\rangle. \tag{4.4}$$

This state is used as the starting point for the next time-propagation step. According to this scheme, the process is sequentially applied for every time step: $t_{i+1} = t_i + \Delta t$. For the initial state $|\Psi(t = 0)\rangle$ only the ground state of the system is populated.
For eq.(4.3) to be accurate, the assumption of a constant Hamiltonian on the time interval Δt has to be made. Hence, the error of this method is determined by the choice of the time step, which has to be small enough to sample the oscillations of the used light field with respect to the Nyquist limit. For the chosen value of 2.42 as (0.1 a.u.), the above mentioned discretization error is acceptably small.
To make this numerical model comparable to an experiment, the dipole response $d(t)$ of the system is calculated. For a given time step t_i $(0 \leq i \leq M)$ the expectation value of the dipole operator $\hat{d}$ is given as:

$$\langle \hat{d}(t_i) \rangle = \int d^3x \ \langle \Psi(x, t_i) | \hat{d}(x, t_i) | \Psi^*(x, t_i) \rangle \tag{4.5}$$

$$= \sum_{n,m \in N} \langle c_n(t_i) | c_m^*(t_i) \rangle \int d^3x \ \langle \Psi_n(x) | \hat{d}_{nm}(x) | \Psi_m^*(x) \rangle + c.c., \tag{4.6}$$

where for the second equation the dependencies of $|\Psi(x, t)\rangle$ are separated into the temporal and spatial part and $c.c$ stands for the complex conjugate of the previous term. The dipole expectation values for dipole forbidden transitions as for all cases $n = m$ vanishes. The integration over the spatial part of the equation leads to temporal constants d_{nm} for all dipole-allowed transitions, respectively, which can be found in literature. Equation (4.6) simplifies then to a linear sum of state coefficients:

$$\langle \hat{d}(t_i) \rangle = \sum_{n,m \in N} d_{nm} \langle c_n(t_i) | c_m^*(t_i) \rangle + c.c. \tag{4.7}$$

This demonstrates as mentioned previously, that further spatial information about the investigated states are not necessary, if their eigenenergies and dipole moments are known.
The resulting temporal dipole moment $d(t)$ and its spectrum $d(\omega)$ can be used

together with the spectral electric field $\mathscr{E}(\omega)$ to compute the absorption (or the OD, see eq.(1.55)) of the investigated system following eq.(1.56), which than can be compared to experimental data.
The simulations use the *atomic units system*, explained in appendix (C).

4.1.2. Simulated Free-Electron Laser Pulses

The recent advent of XUV free-electron lasers (FELs) [52] provides the opportunity to perform experiments with intense ($I \leq 10^{16}$ W/cm^2) and short (≤ 100 fs) laser pulses in the XUV to X-ray regime (see sec.(1.1)). Their properties are excellent for studying quantum dynamics, which has been accomplished with recent benchmark SFS-experiments at the Free-Electron Laser in Hamburg (FLASH) [46, 47, 53, 54]. A key feature for understanding these experiments is the temporal structure of such pulses. Since single-shot temporal FEL pulse characterizations are only recently available [55], these first experiments were carried out with partial knowledge of the pulse structures. Hence, numerical methods were developed [56, 57] varying in computational cost and resulting precision. Here, the partial-coherence method [58] has been implemented due to fast computing time and will be presented briefly (compare to fig.(4.1)):

As a starting point, the knowledge about the experimental envelope of averaged FEL-pulse spectra is necessary (fig.(4.1) A). It can be assumed to be of a certain type, e.g. a Gaussian function, or be measured during FEL experiments. In this thesis, the average of FEL-pulse spectra obtained in experiments in 2016, which are spectrally centred near the helium 2s2p resonance (~ 60 eV), is fitted with a Gaussian envelope. The additional fitting is necessary, as not enough reference spectra were recorded for a smooth average. Nevertheless, this procedure allows to determine two important pulse properties, the carrier frequency and the spectral width with help of the experimental data. The noise-like behaviour of the pulses is included in the spectral phase, which is chosen randomly between 0 and 2π.
An FT of such a pulse leads to a non-coherent temporal behaviour evoked by the spectral phase randomness (B). Afterwards, the multiplication with a Gaussian function, with maximum value set to equal one, leads to partial coherence of the pulses (C), as an inverse FT can prove:
The resulting spectrum is perturbed compared to the Gaussian input envelope (D), but on the other hand, the spectral noise is reduced as partial structures occur compared to the starting white noise. Averaging over pulses produced in this manner leads to the spectral input envelope.

Note, that the width of the temporal Gaussian function can be adjusted to match experimental expectations. For this thesis, values for the assumed averaged Gaussian pulse durations are in between $(10 - 100)$ fs.

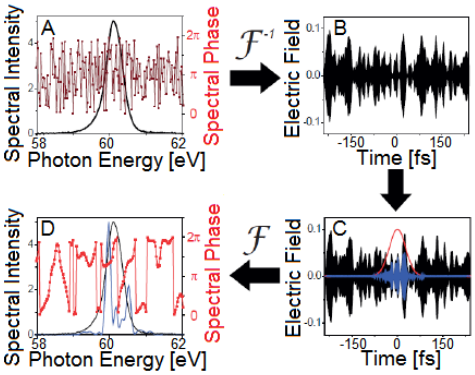

Figure 4.1.: **Numerical approximation of FEL pulses**
A random phase set (A, red) is added to the input spectrum (A, black). FT leads to temporal noise (B), of which a pulse (C, blue) is cut out with a Gaussian envelope (C, red). Its spectrum is plotted in (D). Fig. taken from [58].

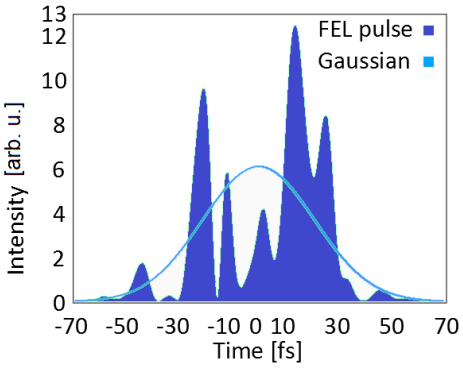

Figure 4.2.: **Simulated FEL pulse**
Exemplary FEL pulse (dark blue) simulated with the method presented in fig.(4.1) and with the same fluence as the Gaussian envelope (light blue). Temporal structures can vary for individual FEL pulses and therefore the peak intensity changes as well.

With this, three out of the four necessary parameters (carrier frequency, spectral width corresponding to coherence time and pulse duration) are defined. Yet undetermined is the amplitude of such a pulse. As fig.(4.2) shows, it is not a well defined quantity anymore, because the temporal structure fluctuates from pulse to pulse. Hence, the fluence F instead of a the peak intensity I_0 is the quantity chosen for characterizing the pulse strength. It is connected to the experimentally accessible pulse energy E_{pulse} via the focus area A_f by:

$$E_{pulse} \approx F \cdot A_f = A_f \cdot \int_{-\infty}^{+\infty} I(t)\ dt\ . \tag{4.8}$$

As the pulse structure has been completely determined by the procedure before, its fluence can be calculated and compared to a desired value. The electric field amplitude is multiplied with the square root of the fraction of the desired and calculated fluencies resulting in the correct fluence of the pulse.
The computed FEL pulses are spectrally broad enough to cover an autoionizing state. Yet, they can contain roots within the resonance width leading to numerical errors while calculating the OD manifesting in undesired noise-like behaviour on top of the absorption signal. This is compensated by an averaging procedure imitating the experimental approach of recording absorption spectra:

A set of 10,000 FEL pulses is simulated and sorted by their fluence. The average fluence of these pulses is calculated and a set of 200 pulses with fluencies closest to the average is chosen. The variation of the fluencies among them is smaller than 1% and therefore their amplitude is scaled with the same factor for all pulses determined with their average fluence in the way explained beforehand. This allows for a linear scaling of fluence scans, as the ones presented in the following section.
The spectral dipole response is calculated with every pulse individually for a given fluence step. The OD is determined following eq.(1.56), but the nominator (signal) and denominator (reference) of the included fraction are replaced by the corresponding average over the 200 pulses:

$$\mathrm{OD}(\omega) = \log_{10}\left(\frac{<|E(\omega) + i\eta\ d(\omega)|^2>}{<|E(\omega)|^2>}\right). \tag{4.9}$$

Averaging over the two quantities before dividing them leads to reduced noise in the optical density and corresponds to the experimental procedure.

4.2. Numerical Results of the 2s2p Resonance in Helium Strongly Driven by XUV Pulses

The few-level model is used to investigate numerically the interaction of intense XUV laser pulses with the 2s2p autoionizing resonance in helium, which can be regarded as the benchmark system for electron-electron correlations. The autoionizating properties and strong-field coulings manifesting in a changed absorption profile have been studied in many puplications: Fano's original work in 1961 [26], the strong-field coupling of autoionizing states by Lambropoulos in 1981 [59], recent experiments, e.g. the line-shape change with an FEL XUV pulse [47, 54], and latest theoretical considerations as Demekhin et al. in 2017 [60] and Mouloudakis et al. in 2018 [61].
Here, the technique of SFS in the few-level framework is utilized to investigate a line shape change of the 2s2p resonance as shown in fig. (4.3). Such line shape changes have been reported in [26], where they are explained with an impulsive ponderomotive energy shift of the eigenstates, leading to a phase-offset of the dipole moment, which changes the line shape following eq.(1.58):

$$\text{states: } \Delta E \xrightarrow{\int ..dt} \text{ dipole phase: } \Delta\phi \xrightarrow{q(\phi)} \text{ line shape: } \Delta q\ . \tag{4.10}$$

But in the XUV regime the ponderomotive energy becomes very small due to the quadratic wavelength dependence of U_p in eq.(1.16). Also, the ponderomotive phase shift should be always positive and thus making the line shape more symmetric, which is not the case in fig.(4.3).

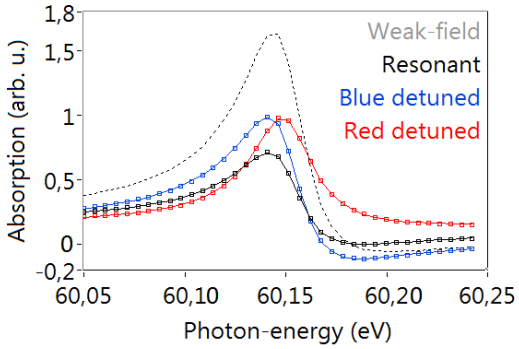

Figure 4.3.: **Strong-driven 2s2p resonance**
The 2s2p resonance is driven by a FT-limited Gaussian pulse of 5 fs duration and 5 $^{J}/_{cm^2}$ fluence. The central photon energy of the pulse is varied from the resonant case to $^{\Delta}/_{E_{2s2p}} = \pm 0.5\%$, corresponding to $E_{red} \approx 59.85$ eV ($\Delta < 0$) and $E_{blue} \approx 60.45$ eV ($\Delta > 0$). The line shapes exhibit a clear symmetry change compared to unperturbed line shape ($q \approx -2.75$) in the weak-field limit (grey). In the resonant (black) and blue detuned case (blue), the line shapes are of asymmetric nature, whereas for the red detuned case (red), it becomes nearly symmetric.

To understand this behaviour, following questions are adressed: Can Rabi-coupling or AC-Stark shifts of the ground state with a non-autoionzing excited state change the line-shape profile in general? If yes, can this effects occur in an autoionizing state as well? Furthermore, can the results be used to explain the experiments performed at the free-electron laser in Hamburg (FLASH) [47, 54].

4.2.1. Line-Shape Changes of a Two-Level System

The spectral line shape due to the resonant transition between two discrete states of a two-level system is known to be Lorentzian in the weak field case [27]. But driven by strong fields, effects as Rabi-coupling and AC-Stark shifts occur as presented in sec.(1.4.4). If they are assumed to be present only during the pulse duration T, the phase of the dipole emission changes due to the energy difference ΔE between the upper-lying dressed state, depending on the detuning: $E_{|\phi_2,n\rangle}$ or $E_{|\phi_1,n+1\rangle}$, and the unperturbed excited state E_2:

$$\Delta\phi \sim \Delta E \cdot T \approx (\pm|\Delta| \mp \sqrt{\Delta^2 + |\Omega'_R|^2}\ )\ T\ . \tag{4.11}$$

The change of sign accounts for the different mapping of the states due to the detuning explained above: (+,-) for $\Delta < 0$ and (-,+) for $\Delta > 0$. This

description is not analytically appropriate, as the formulas are defined under a monochromatic field assumption, which would make this effects last infinity long. Therefore, the simple non-autoionizing two-level system is solved numerically for intense and coherent Gaussian pulses with electric field $\mathscr{E}(t)$:

$$\mathscr{H}(t) = \begin{pmatrix} E_g & d_{ge} \cdot \mathscr{E}(t) \\ d_{ge} \cdot \mathscr{E}(t) & E_e + i\ \Gamma_{lit}/2 \end{pmatrix} , \tag{4.12}$$

where $E_g = 0$ eV, $E_e = 60.15$ eV, $\Gamma_{lit} = 37$ meV and $d_{ge} = -0.035$ a.u. [62]. The coupling of the ground state to the discrete excited state is written in the dipole approximation for electronic transitions. Subsequently the autoionizing process and partially coherent FEL pulses will be added in the following sections.
The absorption profile is calculated and fitted with Fano lines to obtain the Fano q parameter. For a systematic investigation, the pulse detuning and fluence are varied leading to two-dimensional data sets of q and the corresponding phase. In fig.(4.4), the resulting 2D data sets are presented for three different pulse durations: 1 fs, 3 fs, and 5 fs. They are chosen to be smaller than the life time of the resonance ($\sim$ 17 fs as for the $2s2p$ state). As only a single pulse is present, its spectrum has to be broader than the resonance to calculate absorption spectra, which is given with these pulse durations. Also, the strong field effects occur impulsively: The emitted dipole radiation is only manipulated when the pulse is present. Otherwise it is unperturbed leaving its carrier frequency nearly unchanged, thus not shifting the resonance position

The phase plots of fig.(4.4) can be directly compared to eq.(4.11) and shall be discussed first:
• In all weak field cases (fluence $\to 0$), the phase is supposed to equal zero ($\phi(q \to \pm\infty) \to 0$) as the line shape for a non-autoionizing state is Lorentzian. Yet, a phase offset of ~ 0.11 rad is present as a result of the numerical error due to the time discretization which produces a slight artificial asymmetry across the Lorentzian line shape.

• Despite the offset, the plots clearly show how the phase changes with fluence and detuning. In all three cases, an increasing fluence leaves the line unchanged in the resonant case, but otherwise leads to a monotone change of the phase, which is anti-mirror symmetric around the resonance and increasing for blue detuning and decreasing for red detuning. These agrees with a qualitative comparison to eq.(4.11), as higher fluencies of a pulse for fixed duration and shape also lead to larger intensities. The AC-Stark shift of a Rabi-coupled system changes its direction with the pulses detuning, whereas a ponderomotive shift increases monotone with the central wavelength of the driving field. Therefore, the Stark shift is a more suitable explanation for the simulated line shape changes.

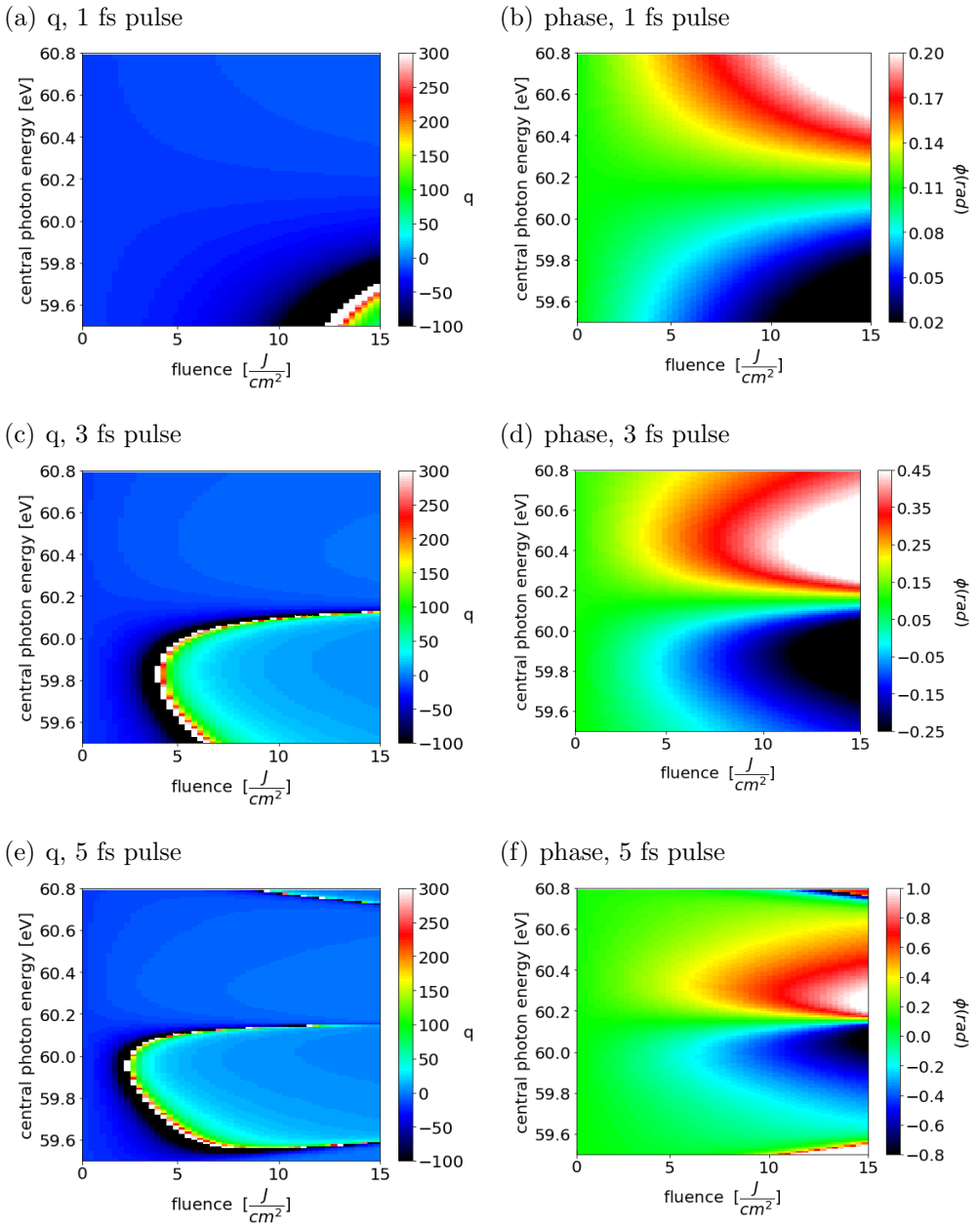

Figure 4.4.: **2D plots of q parameter and phase for a two-level system** The absorption of a simple two-level system is strongly perturbed by an intense driver pulse. The changed line shape is quantified with the Fano q-parameter (left column) and can be read as a corresponding phase (right column). The system is driven with a pulse of duration:
a),b) 1 fs, c),d) 3 fs and e),f) 5 fs.

• Yet not discussed is the behaviour for the resonant case and the dependence on the different pulse durations. Both can be explained as follows: Since in the simulations the pulses have a certain spectral width, they shift the discrete atomic states to energetically distributed dressed states by absorbing/emitting photons with different energies. The probability for an interacting photon of certain energy follows the pulse spectrum. The arising energy shifts of the dressed states are hence to be seen as an averaged value over this distribution, the same holds for the phase shifts. Therefore, a pulse with resonant central photon energy averages over the effects occurring for red- and blue-detuned photons, which are equal in amplitude but with different signs, leading to an average phase shift of zero for an exactly resonant pulse.
Near the resonance, this averaging effect vanishes with increasing detuning, leading to a increased phase shift for blue detuning and a decreasing one for red detuning.
For even larger detunings, the phase shifts change direction. For blue detuned photons, the shifts are decreasing instead of increasing as for small detunings and vice versa for the red detuned case. In between, there is a maximum (white)/minimum (black) for blue/red detuning, respectively. This behaviour occurs, when the pulse spectra are not broad enough to cover both detuning effects and the averaging appears only over red or blue detuned photons, respectively. Note, that it then agree with the trend of the first term in eq.(4.11), as the second one is still small enough to be disregarded (for $\Omega_R^{'} \gg \Delta$).

• Furthermore, the spectral width of a pulse decreases with its temporal duration according to the Fourier-relation. The 5 fs pulse thus has the smallest spectral width and the 1 fs pulse the largest one. This leads to the largest spectral range of the phase averaging effect for the 1 fs pulse. Therefore, its maximum/minimum of the phase shift in the blue/red detuned case, respectively, appears further away from the resonance position (even outside of the detuning range) than for the 3 fs pulse and even further than for the 5 fs pulse. Extrapolating this behaviour towards the c.w. laser, the maximum and minimum for the two detuning regimes meet each other right next to the resonance position. Again, this agrees with eq.(4.11), as for nearly vanishing detuning the phase shift performs a jump from its maximum $\approx +|\Omega_R^{'}|$ (slightly blue detuned) to its minimum $\approx -|\Omega_R^{'}|$ (slightly red detuned).

After this detailed study of the phase behaviour for the two level system, the corresponding q-parameter plots can be understood as a changed Fano-profile induced by the internal Rabi-coupling-like behaviour. The asymmetry between red and blue detuned behaviour comes from the above mentioned numerical phase offset and the non-linear phase-dependence of the q parameter. For shorter pulses, the phase shifts are less pronounced (note, that the

magnitude scale of the phases is different) and thus the line shapes are less modified along the fluence axis. This is reasonable, because the fluence for all three pulses is kept to be the same. Therefore the peak intensity of the pulses has to increase corresponding to the inverse ratio of their durations. Yet, the discussed phase shifts dependent on the Rabi-frequency, which is proportional to the electric field amplitude and not to the intensity.

4.2.2. Manipulating the Fano Line Shape of an Autoionizing State

In the following, the investigation of laser-pulse-induced line-shape changes will be extended to the autoionizing 2s2p resonance of helium, which already poses a modified absorption profile due to the intrinsic electron configuration interaction [26]. Following the model based on [63], the autoionizing $2s2p$ resonance can be modelled as an excited state (e) interacting with a 'continuum state' (c), i.e. the one electron ionization continuum is treated as a fast decaying state with a broad spectral 'line' width Γ. The ground state (g) and the excited state (e) are chosen as in the two-level case. With the continuum state at $E_e = E_c = 60.15$ eV and a width of $\Gamma = 26$ eV, the Hamiltonian of the system can be written as:

$$\mathscr{H}(t) = \begin{pmatrix} E_g & d_{ge} \cdot \mathscr{E}(t) & d_{gc} \cdot \mathscr{E}(t) \\ d_{ge} \cdot \mathscr{E}(t) & E_e & V_{CI} \\ d_{gc} \cdot \mathscr{E}(t) & V_{CI} & E_c + i\ \Gamma/2 \end{pmatrix} . \tag{4.13}$$

The dipole moments $d_{ge} = -0.035$ a.u. and $d_{gc} = 0.28$ a.u. are in accordance with synchrotron measurements [62]. The configuration interaction $V_{CI} = 0.01801$ is chosen together with the value for Γ to match the literature values of the 2s2p resonance in the weak-field case (see tab. (1.3)). The two-dimensional plots of the q parameter and the dipole phase depending on fluence and detuning are compared in fig.(4.5) for the three different pulse durations as in the two-level case.
Comparing fig.(4.5) to fig.(4.4), two key features for the three-level case are apparent: First and most obvious, the phase and the q parameter do both change on the same order of magnitude as in the two-level case for each pulse duration, respectively. Hence, the beforehand mentioned coupling mechanism between the discrete ground and excited state and the resulting energy shift seems to persist the presence of the interfering autoionization decay. This is explained by the short few fs interaction time scale of the pulse compared to the natural 17 fs autoionization decay time of the $2s2p$ state.

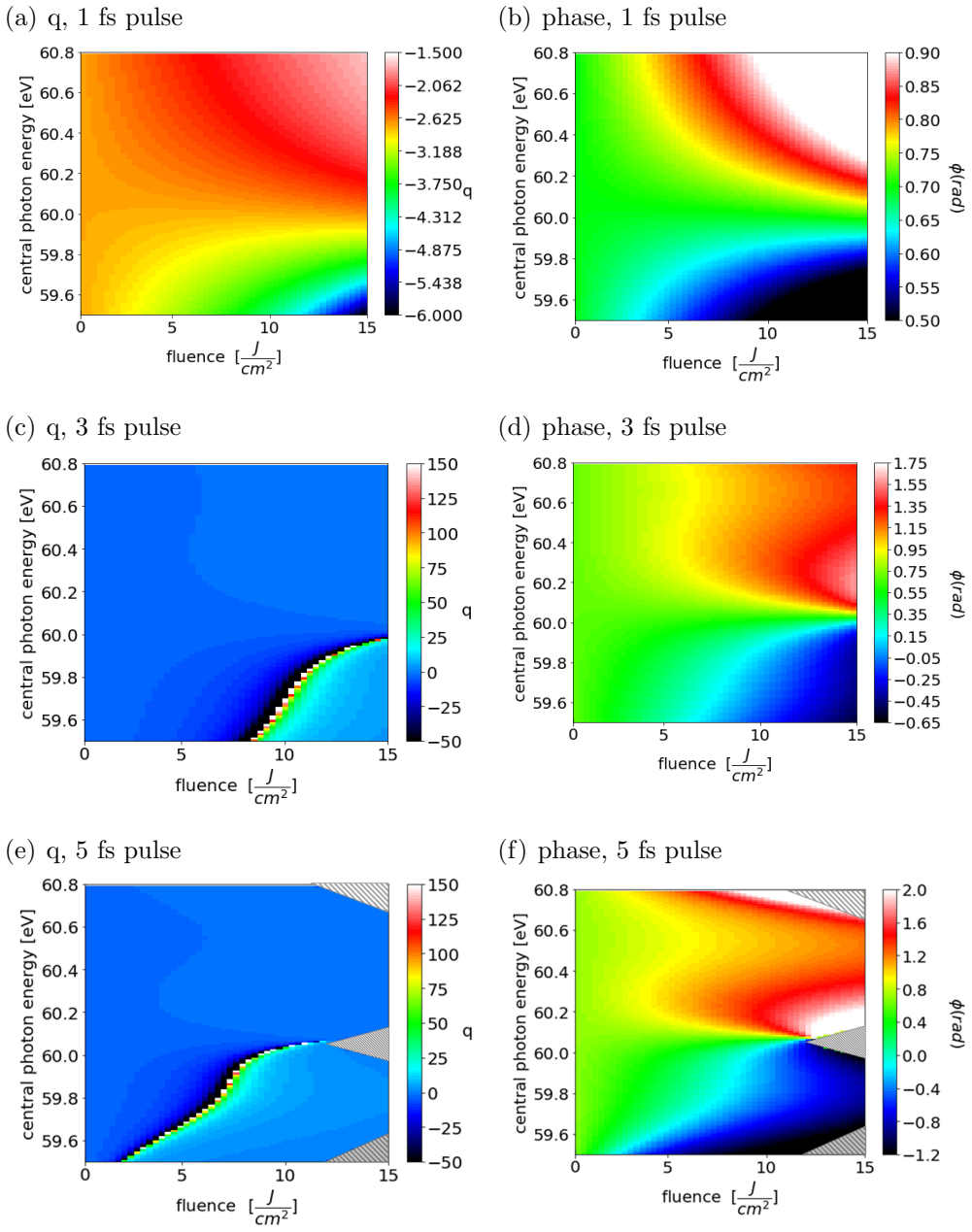

Figure 4.5.: **2D plots of q parameter and phase for three-level system** The figure is structured as fig.(4.4), but contains the data for the three-level system (eq. (4.13)). The grey shaded areas in e), f) do not contain data as the Fano-fits of the line shape did not converge there due to numerical reasons.

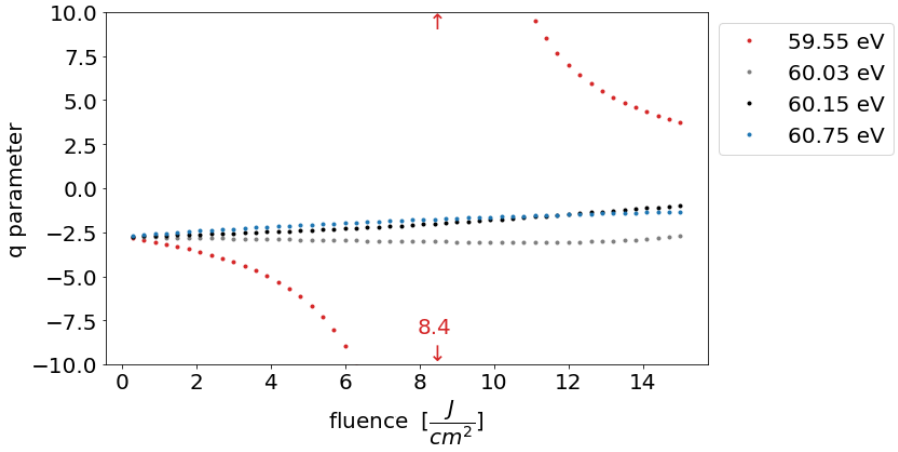

Figure 4.6.: **q-parameter lineouts for 3fs-pulse driven 3-level system** The q parameter is plotted vs. fluence for four different detunings depicted in the legend. The different behaviours of the curves are described in the text.

In addition, the symmetry properties of the two-level phase plots are distorted by including the third continuum state. The energy position, at which the line shape is unchanged, $\phi(q = -2.75) \approx 0.698$ rad, as in the weak-field limit, is moved from the resonance position to a red-detuned value around ~ 60 eV. Due to the presence of the continuum state and the configuration interaction to the excited state, the shifted position for the unchanged line shape can be comprehended, although not exactly explained.
In general, central photon energies higher than ~ 60 eV lead to positive phase shifts, whereas for lower photon energies the opposite is the case, similar to the behaviour in fig.(4.4) around the resonance. As a consequence of this disturbed phase-change symmetry, the behaviour of the q parameter is altered compared to the two-level case.

For comparison to sec.(4.2.3), lineouts of the q parameter vs. the fluence for the 3 fs driving pulse at photon energies of: ~ 59.55 eV (red), ~ 60.03 eV (grey), ~ 60.15 eV (black), ~ 60.75 eV (blue) are plotted in fig.(4.6). Besides the resonant case, the highest and lowest detuning correspond to $\Delta/E_{2s2p} = \pm 1\%$. whereas the choice of ~ 60.03 eV becomes evident with the results of sec.(4.2.3) and will be discussed there. Here, some more detailed features of fig.(4.6) shall be presented:

- For red enough detuning (red line) the q parameter decreases to an Lorentzian line shape at nearly ~ 8.4 J/cm² (marked with red arrows). There, the q parameter changes sign in the infinite and moves towards smaller (positive) values, manifesting in Fano lines of opposite symmetry.

- The lineout for the $E_{ph} \approx 60.0$ eV case shows more evident than the 2D colour plot, that the q parameter does change slightly there, decreasing first for lower and intermediate fluencies but increasing afterwards for highest fluencies.

- The blue detuned and resonant case exhibit a similar change in form of a slight increase of the q parameter. For a fluence of ~ 12 $^{\mathrm{J}}/_{\mathrm{cm}^2}$ the blue and black curve even cross, leading to the same Fano-absorption profile for differently centred photon energies.

4.2.3. 2s2p Resonance Interacting with Free-Electron Laser Pulses

To compare the simulation results with experimental measurements, the utilized pulses have to exhibit partially coherent temporal structures as FEL pulses do. Since the FEL pulses based simulations are far more computationally expensive than short coherent pulses, due to their sorting and averaging procedure, no complete two-dimensional data sets of the q-parameter are calculated. Instead, the fluence dependency of q is investigated for four different central photon energies. The Gaussian fitted envelope of the experimentally averaged FEL spectra, centred at ~ 59.9 eV, is therefore shifted to the resonance position, 60.15 eV and to the detuning values ~ 59.55 eV and ~ 60.75 eV corresponding to $^{\Delta}/_{E_{2s2p}} = \pm 1\%$. The averaged spectra exhibit a spectral FWHM of ~ 0.7 eV corresponding to a reciprocal coherence time of ~ 2.1 fs. This value is in the same regime as the the pulse durations of the previous section and is unchanged while shifting the spectral position.
Furthermore, the average temporal durations of the FEL pulses is varied from 10 fs over 40 fs to 75 fs. The durations are chosen to be larger than the coherence time as well as smaller than the experimentally determined electron bunch duration of ~ 100 fs, which in general is overestimating the laser pulse duration [64]. The resulting q-parameter plots are presented in fig. (4.7).

To understand the effects occurring in these plots, the following picture of the temporal FEL-pulse structure is found to be helpful:
Instead of taking an FEL pulse as one complete pulse with partially coherent substructures, alternatively several coherence spikes within a certain time window (the total pulse duration) might be a less precise, but more illustrative description. The coherence spikes have a duration of at least the coherence time ~ 2.1 fs, but can be longer (≤ 10 fs), because the pulse spikes can be chirped. On top, not only the spike duration can change from sub-pulse to sub-pulse, but also their peak intensities (compare to fig.(4.2)) and their central frequency can vary within the complete FEL pulse spectrum.
Increasing the overall time window/FEL-pulse duration, while keeping the co-

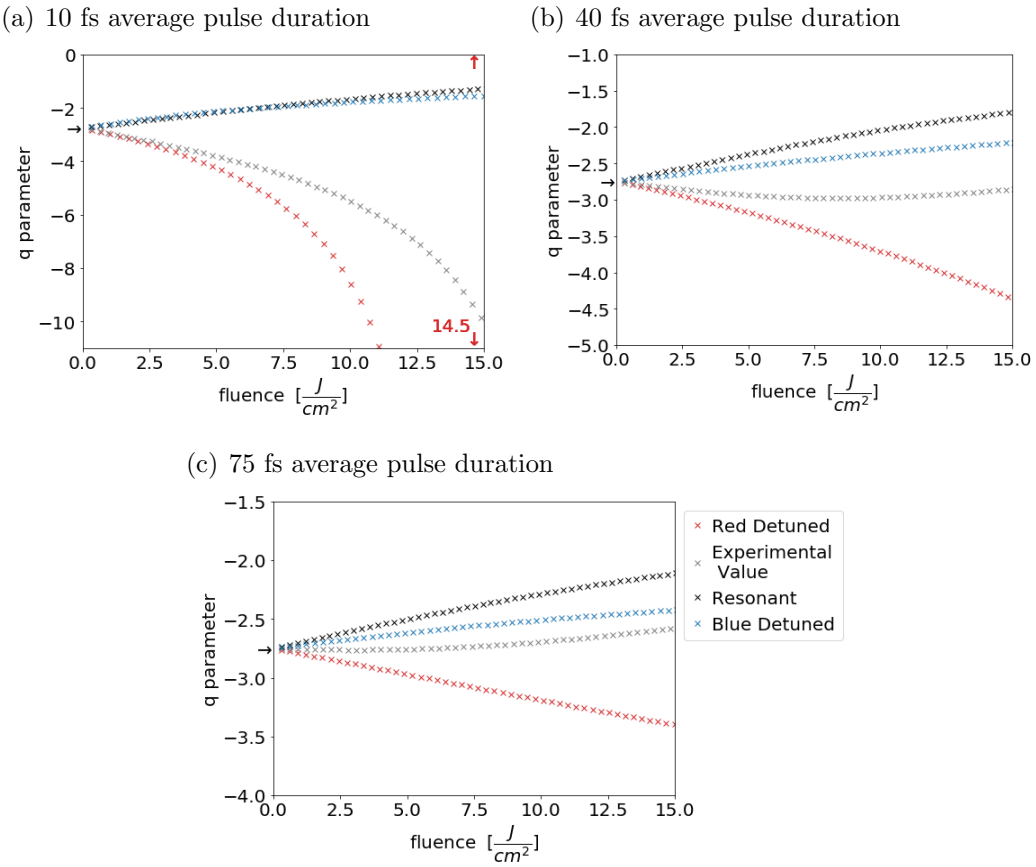

Figure 4.7.: **Fano-q-parameter of 2s2p resonance for different FEL pulse durations and detunings**
FEL pulses of different durations: (a) 10 fs, (b) 40 fs, (c) 75 fs, and detunings (see legend) change the line-shape of the 2s2p resonance in different manners, what is quantified with the presented Fano-q-parameter. The weak-field limit: $q = -2.75$ is depicted with black arrows at the y-axis.

herence time constant, leads than to a larger amount of coherent (sub-)pulses within the full FEL-pulse time window, with different spectro-temporal properties. Therefore, the choice of a 10 fs temporal envelope results in only very few sub-spikes, down to the possibility of even one, which leads to a high coherence of the total FEL pulse. With this picture in mind, the variation of the line shape in fig.(4.7) can be understood. The most coherent, 10 fs FEL pulses (a) evokes changes of the Fano-q-parameter, which are comparable with the ones for the coherent 3 fs pulses in fig.(4.6) for the different detunings, respectively: In the blue-detuned (blue curve) and resonant case (black), the q-parameter increases with rising fluence. The increase in the blue-detuned case is slightly faster for lower fluencies, but is overtaken by the resonant case

for higher ones, crossing at ~ 6 $^{\mathrm{J}}/_{\mathrm{cm}^2}$. For the red detuning (red curve), the q parameter decreases rapidly with rising fluence. At $F \approx 14.5$ $^{\mathrm{J}}/_{\mathrm{cm}^2}$, the $\lim q \to \pm\infty$ is reached corresponding to a Lorentzian line shape, depicted in the plot with the red arrows. In the case of the experimental position of the spectrum (grey), the q behaviour is similar as for the red curve, but not as pronounced, only decreasing to a minimum of $q \approx -10$. Note, that this is not directly comparable with the plot of the coherent 3 fs pulse in fig.(4.6), because there, the grey curve shows the case of another detuning, 60.03 eV, than the ~ 59.9 eV central photon energy as chosen in fig.(4.7).
Looking at plot (b), in which an FEL pulse of average 40 fs pulse duration is utilized, several differences can be found compared to plot (a): The resonant case exhibits the most significant increase of the q parameter, whereas for the blue-detuned pulses the q parameter is still increasing, though at a lower rate. The red curve is again decreasing, but less pronounced than in (a) reaching a minimum of $q \approx -4.4$ at highest fluencies. The grey curve shows the most drastic difference compared to (a). It is not monotonously decreasing anymore, but changes from a decreasing behaviour for lower fluencies to an increasing one for higher fluencies. This is similar to the grey curve in fig.(4.6) for the coherent pulse, but occurs for another detuning. All of these effects are comprehensible with the temporal FEL-pulse-structure picture: Going from a 10 fs temporal envelope to a 40 fs one, multiple coherence spikes can occur within a single FEL pulse. Therefore, a single FEL pulse averages over a broader selection of different effects induced by different sub-pulses. Hence, the resulting effects, e.g. the behaviour of the red- and blue-detuned case, are less pronounced than for the more coherent 10-fs FEL pulse. Furthermore, a 40-fs pulse duration is near to experimental available FEL pulses durations. This implies, that approximating an FEL pulse to a train of coherent spikes becomes a less precise description and the more complicated behaviour of a partially coherent pulse has to be considered. In general, the decreased coherence of FEL pulses for longer pulse durations is hard to describe or illustrate. Therefore, it hast to be assumed, that the detuning of FEL pulses can effect several pulse properties in a non-trivial way. Thus, the found deviations are still comprehensible.
Increasing the FEL-pulse duration even more to 75 fs, the resulting plots of the q-parameter (c) confirm the beforehand given explanation: As the step from the coherent-spike-train picture to the description of the partially coherent FEL pulse is already realized while going from a 10-fs to a 40-fs pulse duration, the further increase to 75 fs should not give rise to further deviations. As the comparison between (b) and (c) of fig.(4.7) shows, the four curves of the q-parameter vs. fluence do look alike qualitatively for the different detuning values, respectively. Again, the change of the q-parameter is in (c) for every curve individually less pronounced than for the shorter pulse duration in (b), which matches the expectations as even more counteracting process are initi-

ated by a larger number of sub-pulses within a single FEL pulse.

In conclusion, it could be demonstrated that employing numerically generated FEL pulses can lead to changed Fano profiles evident by a manipulated Fano-q-parameter of the perturbed 2s2p resonance. The changes are comparable to the scenario in which the system is driven with short, coherent pulses of the same fluence. There, the changed absorption profiles can be explained by a AC-Stark shifts due to a Rabi-like coupling mechanism via comparing to a simplified two-level model.
To make this findings comparable to the corresponding experimental data [47], the absorption profile of the 2s2p resonance for different pulse fluencies is plotted in fig.(4.8) as an two-dimensional colour plot in a), whereas in b) lineouts of the 2D plot for three fluence values are presented. The data set for the red-detuned pulses of 40 fs duration is found to fit best to the experimental results, for which pulse durations of $(50-70)$ fs and a central photon energy of ~ 59.9 eV is assumed. The plots are similar to the experimental data presented in the same manner as the simulations in fig.(4.7(c)), although the agreement of the pulse parameters is not yet perfect. Since the exploited numerical FEL pulse generation procedure as well as the few-level simulations are simplified models, a quantitative comparison to the experiment is not presented here. Yet, the utilized numerical framework supports the experiment results and the idea of Rabi-coupling/Stark-shift induced line-shape changes.

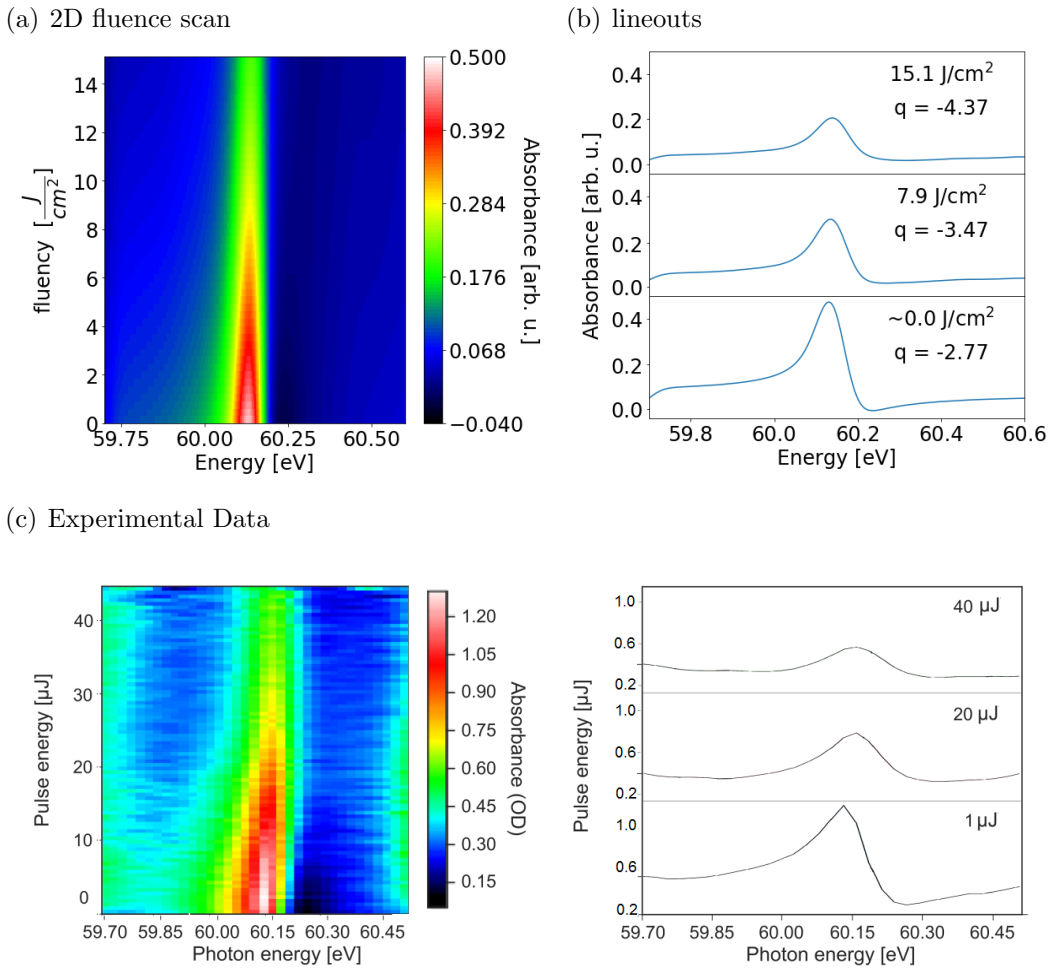

Figure 4.8.: **OD of 2s2p resonance strongly driven by FEL pulses** The OD of the $2s2p$ resonance driven by FEL pulses of 40-fs average pulse duration and centred around 59.9 eV is manipulated by varying the pulses fluence. In (a) the simulated 2D absorption is plotted vs. photon energy and fluence, whereas in (b) lineouts of (a) are presented for the three shown fluence values. The resulting changed Fano line shape is quantified by the given q-parameters. (c) Comparison to the experimentally measured 2D plot and lineouts of the OD for the $2s2p$ resonance. (c) is adapted from [47].

5. Experimental Results

After investigating numerically the strong-field interaction of helium with short wavelength XUV pulses, in this chapter first experimental results of the interaction with intense long wavelength SWIR pulses will be presented. Due to the much smaller photon energy of these pulses, strong-field effects between excited states rather than between the ground state and an excited state can be studied. As the energy differences of the DES of helium to its ground state are nevertheless in the XUV regime, an additional weak XUV pulse is mandatory to perform SFS. Hence, the process of HHG is exploited to upconvert one part of the utilized OPA signal pulses into probing XUV pulses. The results for experimentally generated high harmonics spectra are presented in the next section, followed up by the intensity dependent and time resolved investigation of the DES in helium.

5.1. High Harmonic Generation

To perform wavelength tunable experiments in the SWIR, the OPA signal output is tuned to three different wavelenghts: 1300nm, 1413nm and 1500nm. For the same pulses, the FROG pulse characterization is carried out and presented in chapter (3). The corresponding spectra of high harmonics are shown in fig.(5.1). To find optimized phase matching criteria (eq.(1.21)), the utilized noble gas, its backing pressure p and the pulse energy E_{pulse} has to be adapted to the focal length f and the central OPA wavelength. As a starting point, references [65, 66] were considered, before manually varying the different parameters. Due to pointing fluctuations of the laser system, the HHG spectra are fluctuating on a shot-to-shot basis, hence a systematic quantification of the best phase matching parameters has not been carried out. The following settings were found for optimal XUV flux around ~ 60 eV:

λ_c [nm],	E_{photon} [eV]	E_{pulse} [μJ]	gas	p [mbar]	f [m]
1300	0.95	360	Ar	380	0.50
1413	0.88	370	Ar	385	0.50
1500	0.83	600	Ar	390	0.50

Table 5.1.: Phase matching optimized HHG settings

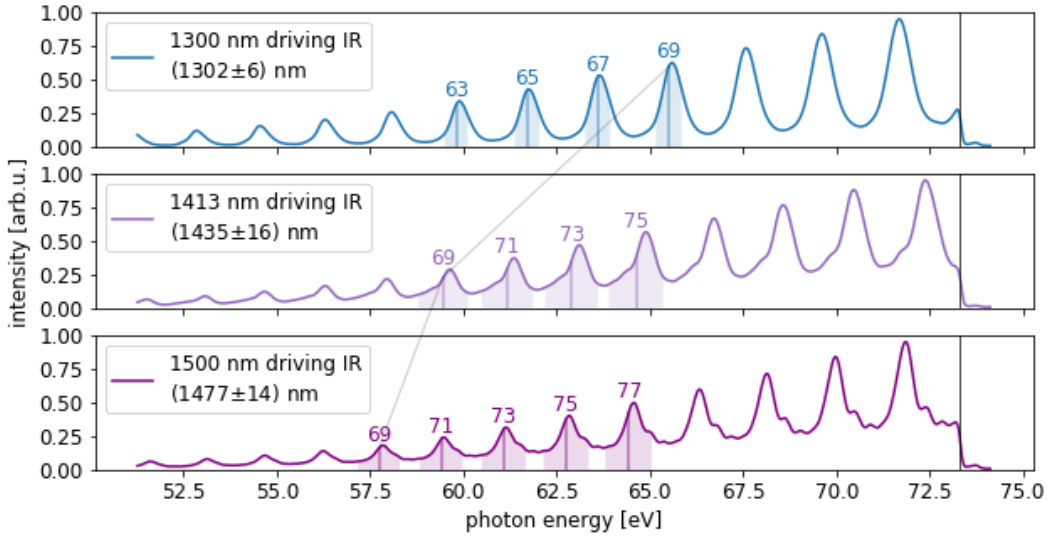

Figure 5.1.: **Measured high-harmonic spectra**
For the three different driving IR wavelengths the corresponding normalized HHG spectra are presented. The high harmonic peaks, for which the spectrometer is calibrated, are marked with vertical lines and the resulting average driving wavelength is shown with error bars below the measured central IR wavelength. Further explanations are given in the text. As a guidance for the eye, the 69th harmonics of the different spectra are connected with a gray line, showing how the position of the same harmonic order shifts towards higher photon energies for smaller driver wavelengths.

The FROG characterizations of the driving pulses yield pulse durations of around 35 fs (see tab.(3.3)). Thus, the measured HHG spectra are supposed to be discrete as the few-cycle regime [67] is not yet reached. As fig.(5.1) shows, the background corrected spectra contain discrete peaks but are continuous enough to not reach zero amplitude at any wavelength. This behaviour may be explained with nonlinear effects, e.g. third harmonics may already be generated within the outer parts of the Ar gas volume and then generate high harmonics on their own, filling up the spectral gaps. Additionally, spatially chirped high harmonics are evident on full chip images of the spectra, leading to continuous spectra due to the employed spatial averaging. As a result, the obtained XUV spectra are continuous enough to illuminate the complete spectral region at which the to be measured helium states are located.
For further analysis of the HHG spectra, an energy calibration has been carried out. Spectra of the XUV pulse interacting with helium gas while blocking the IR pulse with an aluminium filter are recorded and used to determine the positions of the helium resonances (presented in the next section, fig.(5.3 a1)).

With their help, the spectrometer is calibrated in the region of $(60 - 65)$ eV by a quadratic fit of the helium literature absorption line wavelengths to the pixel positions determined by Fano-fits. The position of the aluminium filter edge is evident in fig.(5.1) as a sharp cutoff of spectral intensity and is marked with a black vertical line. Its position is expected to be at 72.7 eV [68] but is found around 73.3 eV, showing that the photon-energy calibration is not valid there anymore.
Therefore, the determination of the HHG peak position is restricted to the calibrated region, in which four to five harmonic peak positions are determined by a peak finder routine. With the difference between two neighbouring harmonics, the average IR photon energy is calculated, as the harmonics are separated by twice this energy. The found harmonic position are divided by the IR photon energy to determine the harmonics order n. This harmonic order, rounded to an integer, is used to draw the vertical lines in fig.(5.1) marking the harmonics' positions. The shaded area represents n times the statistical error of the IR photon energy. Furthermore, the corresponding central IR wavelengths are compared to the independently measured spectral IR positions:

measured:	1300 nm	1413 nm	1500 nm
HHG spectra:	(1302 ± 6) nm	(1435 ± 16) nm	(1477 ± 14) nm

Table 5.2.: Comparison of central wavelengths of driving SWIR pulses

For the 1300 nm IR pulse, the two wavelength values agree with each other within the error. For the other two wavelengths the agreement is only within twice the error margins. Yet, there is no error estimate given for the independently measured value, which is determined by a peak finder routine without an error output. But as the *Ocean Optics NIR Quest* spectrometer has an average resolution of 8 nm/pixel, the error is expected to be larger than that. Taking this into consideration, the wavelength values already are in agreement to each other. It should be noted that the central IR wavelengths determined from the HHG spectra are shifted to values similar to the ones found by the FROG characterization. Hence, the spectral shift could also be explained by spatial, intensity dependent effects not evident in a linearly averaged spectrometer measurement. To finally evaluate, whether these discrepancies are of statistical or physical nature, further measurements are necessary.
As a final remark it shall be added, that for all three harmonics spectra the intensities increase with higher photon energy below the aluminium edge. Thus, the harmonic cutoff energy has to lie at higher photon energies, which proves the potential of this setup to reach photon energies well beyond ~ 100 eV.

5.2. Multicolour Strong Field Spectroscopy Results

With SWIR and XUV pulses, SFS of helium can be carried out in an intensity dependent manner like in [33] and time resolved like in [69]. In addition, the OPA allows to add wavelength tunability as another degree of freedom.

To perform any kind of absorption spectroscopy following Lambert-Beer law (eq.(1.50)), reference spectra are mandatory. The HHG spectra presented in the previous section would meet this purpose in principle, but due to the large fluctuations of the driving pulses, subsequently measured spectra are only partly reliable. Another solution is the calculation of reference spectra via FT filtering as utilized in [30, 69]. With its help, the measured signal spectrum is filtered for higher frequency components in the FT domain, leaving only the lower frequency components of the harmonics as a reference. Yet, for the measurements with the XUV spectra presented before, this method does not work well, as the signal and harmonic components are partially overlapping in the Fourier domain as they are equally broad and cannot be separated easily with a single filter (see fig.(5.2 F)).
Therefore, the method is expanded by utilizing a short-time Fourier transformation (STFT), also known as windowed FT. An example for a measurement with a 1240 nm OPA pulse discussed in sec.(5.2.2) is presented in fig.(5.2). For the STFT, a certain part of the measured spectrum containing the helium absorption lines is cut out by a Hann window ($\sim \sin^2$) function of 50 pixel width (slightly larger than a harmonic peak width) and Fourier transformed after zero-padding. The window function is subsequently shifted by one pixel to scan over the spectrum generating a two dimensional STFT spectrogram of the 'signal' spectrum (fig.(5.2 A)). The transformation is carried out for a reference scan without the helium absorption lines as well, shown in fig.(5.2 B). On the lower end of the Fourier axis (y axis), the harmonics of the spectrum are visible in A and B. Higher Fourier frequencies do not contribute to the harmonics signal anymore, as evident in B. Thus, the (column like) peaks only present in A have to come from the measured helium absorption lines. Also, the two most evident lines in A match with the resonance positions of the 2s2p and 2s3p state, respectively. Other lines are barely visible by eye in the 2D plots. Therefore, the STFT is a helpful tool to understand which frequencies in the FT domain contribute to the measured spectrum at a given spectral position. As fig.(5.2 C) shows, the lowest part of the Fourier axis includes mainly harmonics contribution (green), the intermediate one is generated by helium absorption signal (red) and the highest Fourier frequencies contain the residual noise (blue). The Fourier frequency range for the helium signal is chosen larger for photon energies over 55 eV than for lower photon energies,

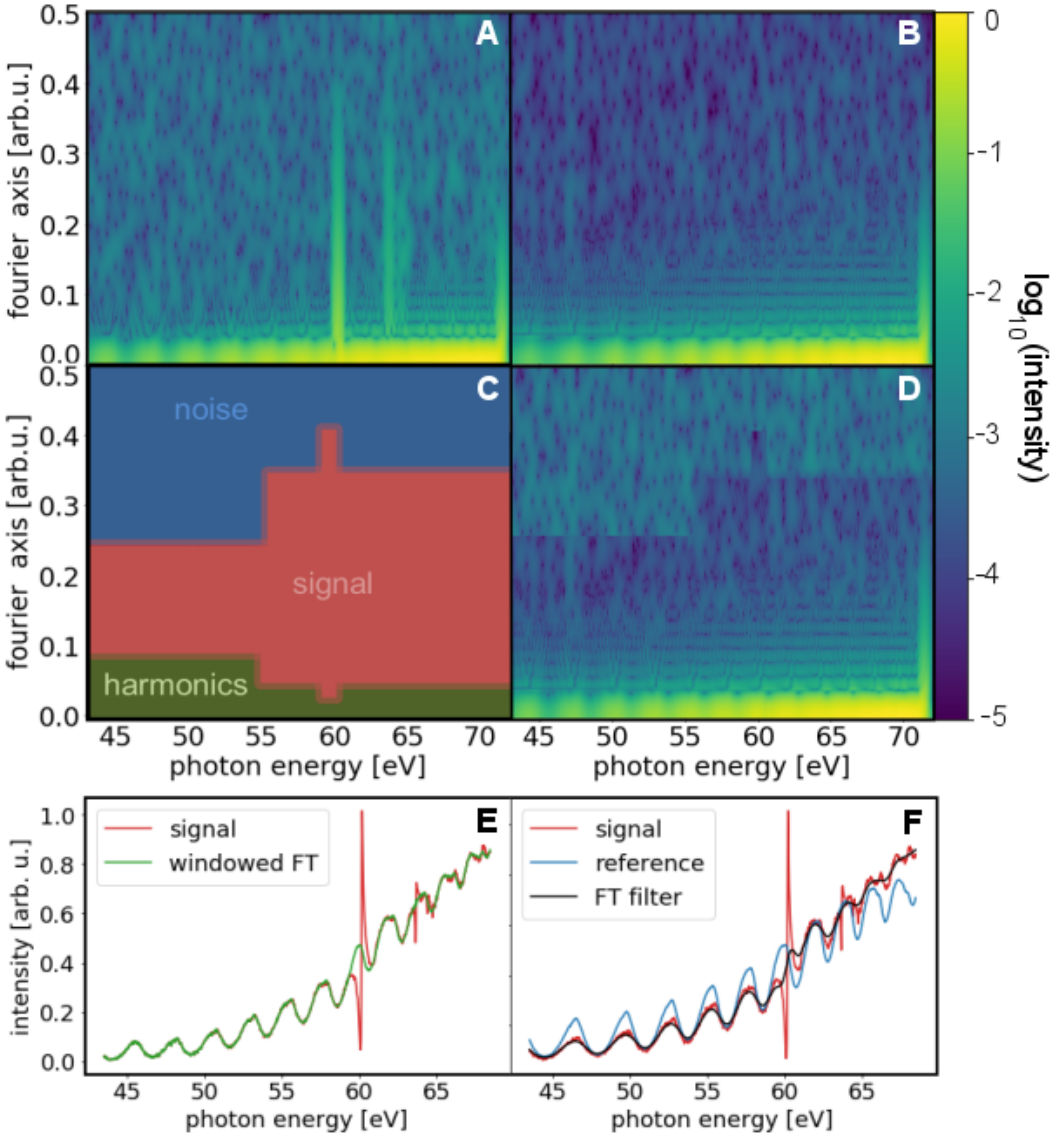

Figure 5.2.: **STFT retrieved high-harmonic reference spectrum**
A The STFT of a measured signal spectrum. **B** A corresponding reference measurement is STFT and adjusted in position and intensity trend to the signal spectrum. **C** Different Fourier frequency components are found to correspond to different kinds of signals: harmonics are generated by low FT frequencies, the helium signal by intermediate FT frequencies and noise by highest FT frequencies. **D** The area of A marked as signal in C is replaced by the same area of the reference STFT (B). **E** Inverse STFT and signal spectrum compared to **F** independent reference spectrum and FT filtered reference.
The 2D STFTs are plotted with a logarithmic intensity scale.

as the resonances are known to be located there. For the strongest absorption line, the 2s2p resonance, even more Fourier frequencies are included.
Further, the red coloured area in C is replaced by the corresponding area of the STFT of the reference spectrum in B. For that purpose, the STFT of the reference is adjusted beforehand to better match the signal data by comparing the harmonic contribution in the STFT of the reference to the signal: First the STFT reference is shifted by a few pixel corresponding to the mean difference between the individual harmonic peaks of signal and reference data. Afterwards, a cubic fit of the harmonic peaks is utilized to adjust the intensity trend of the reference harmonics to the one of the signal data. The resulting replaced STFT is shown in fig.(5.2 D). The edges between the two data sets are smoothed by applying a weighting function of 10 pixel width between the reference and signal data, linearly increasing from 0% to 100% of the replaced data. Note, that edges at high Fourier frequencies are still noticeable in D, because the STFT amplitudes are in the order of the noise, which is in a slightly different magnitude scale due to different integration times. More importantly, the transition is smooth at the low frequency edge avoiding numerical errors for retrieving the harmonics spectrum.
Finally, an inverse STFT is applied on the replaced data set to obtain the reference harmonic spectrum, which is plotted in fig.(5.2 E) in green. The input signal spectrum is shown in red. For a comparison, the measured reference spectrum and the FT filtered reference are presented in fig.(5.2 F). The STFT retrieved reference fits best to the harmonics of the signal spectrum.
It should be added, that the plots contain the amplitude of the complex STFT, as it is most clear to understand, which frequencies contribute to which signal. Nevertheless, the full complex numbers of the STFT are manipulated by filtering the real and imaginary part of the STFT individually. In total, the procedure of the STFT filtering can be optimized further, but is an important tool for a first evaluation of the SFS data, presented in the following subsections.

5.2.1. Doubly-Excited Helium Driven by Pulses of Different Intensities

The very first SFS experiments performed with the OPA laser system are an intesity depdent study of the DESs in helium as in [33], but with a different central wavelength of the perturbative IR pulse than the previously used 800 nm. The same OPA signal pulses as characterized in chapter (3), centered around 1300 nm, 1413 nm and 1500 nm are utilized for this study. Their corresponding high harmonic spectra were presented in section (5.1).

(a) 1300 nm: (a1) without IR, (a2) weak IR, (a3) intermediate IR, (a4) intense IR

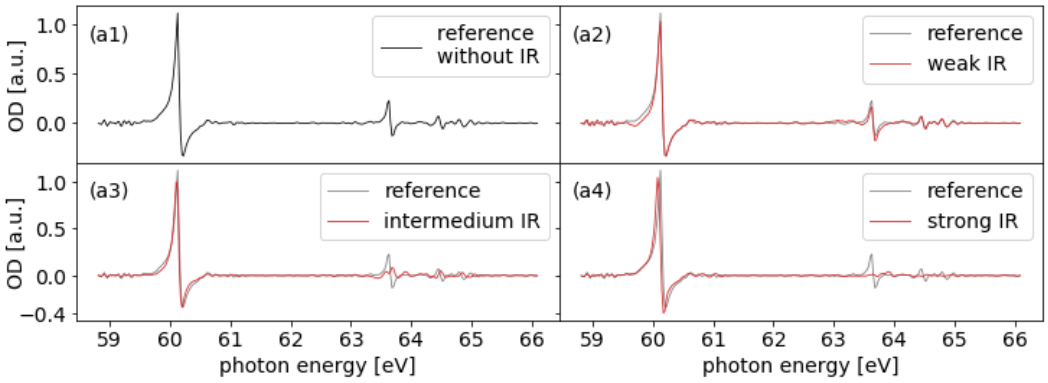

(b) 1413 nm: (b1) weak IR, (b2) low-medium IR, (b3) high-medium IR, (b4) intense IR

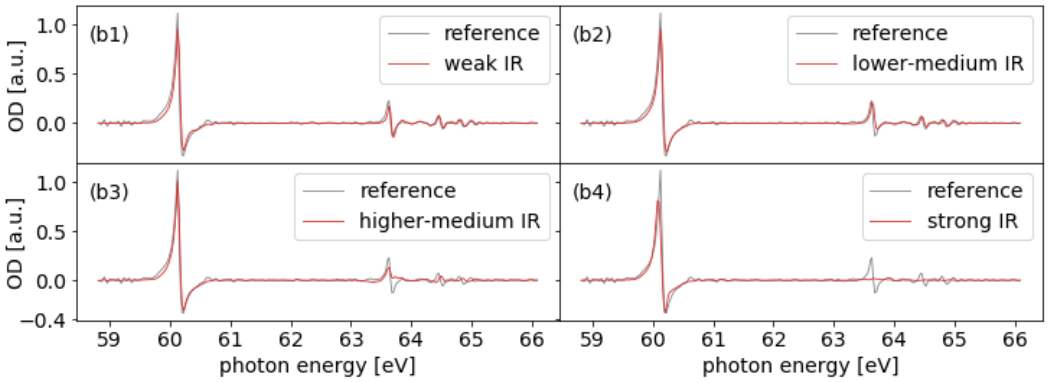

(c) 1500 nm: (c1) weak IR, (c2) low-medium IR, (c3) high-medium IR, (c4) intense IR

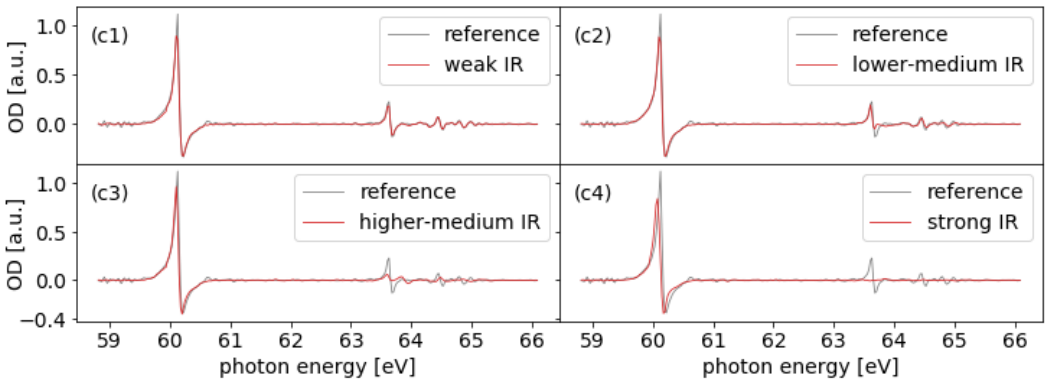

Figure 5.3.: **Intensity-dependent DES absorption line modification** The modified OD (red) of the $n_1 = 2$ DES in helium depends on the central wavelength and intensity of the perturbative IR pulse. The central wavelength is tuned from (a) 1300 nm over (b) 1413 nm to (c) 1500 nm. The intensity has not been quantified and thus is given in terms of 'weak', 'intermediate' and 'strong'. Note, that the reference OD without IR pulse (a1) is shown in grey in all plots. For (b) and (c) two different intermediate intensities are presented, the 'higher-medium' settings correspond to the 'intermediate' case of (a).

The intensity of the SWIR pulses is not measured directly in the target region. Thus, their intensity can only be varied qualitatively in relative terms. An aperture is used for that purpose, gradually decreasing the pulse intensity upon closure. The completely open aperture will be referred to as 'strong', the nearly closed as 'weak'. For the 1413 nm and 1500 nm IR pulses, two different settings for intermediate intensities are recorded as 'higher- and lower-medium'. With the 1300 nm SWIR pulse, only the higher-medium (depicted as 'intermediate') setting is measured, but additionally a reference measurement with the 1300 nm harmonics is carried out by blocking the perturbative IR pulse with an aluminium filter. The results for the intensity dependent DES absorption lines for the three different perturbation pulse wavelengths are shown in fig.(5.3).
In the reference absorption spectrum (fig.(5.3 a1)), the absorption lines of the $2s2p$, $sp_{2,\{3,4,..\}+}$ states are visible, whereas the corresponding '-' manifold is too low in amplitude to be noticeable. With the plus manifold upto the $sp_{2,5+}$ resonance, the beforehand mentioned spectrometer pixel to photon-energy calibration is carried out. Furthermore, the width of the measured $2s2p$ Fano resonance is used to determine the resolution of the spectrometer with the inserted 200 µm spectrometer slit mentioned in sec.(2.2). The measured $2s2p$ resonance is fitted with a Fano profile to obtain the experimental value of the line width $\Gamma \approx 81$ meV instead of the literature value $\Gamma_{lit} \approx 37$ meV. With a Gaussian window the literature Fano line shape is convoluted to match the experimental line width. This is achieved with a FWHM = $\Delta E \approx 62$ meV for the Gaussian window. Thus, the energy resolution of the spectrometer is calculated to be $E_{2s2p}/\Delta E \approx 970$, which is in good agreement with previous measurements carried out with the setup [30, 33].
The weak-field cases (fig.(5.3 a2,b1,c1)) show as expected that the DES line shapes are nearly unperturbed compared to the reference measurement. In contrast, the strong SWIR pulses modify the absorption line most drastically (fig.(5.3 a4,b4,c4)): For all three wavelengths, all lines starting from the $sp_{2,3+}$ resonance going to higher photon energies are (nearly) not present anymore. This behaviour can be explained with strong-field ionization of these resonances as described in section (1.3). Due to a lack of an absolute intensity calibration in the target, the SFI cannot be classified. In the time-resolved study of the following subsection, multi-photon ionization (MPI) will be discussed to be the most likely mechanism. Interestingly, the $2s2p$ resonance is nearly unperturbed for all thee wavelengths. This indicates, that the MPI is not capable of ionizing this state. Taking into consideration that 6-7 photons are required for ionization using the longer wavelength driver, this is comprehensible. Furthermore, the three different photon energies are not resonant for coupling the $2s2p$ resonance to any other state (compare to tab.(1.3)) also suppressing a possible resonance enhanced MPI channel.
For the two intermediate intensities, two wavelength dependent features can be

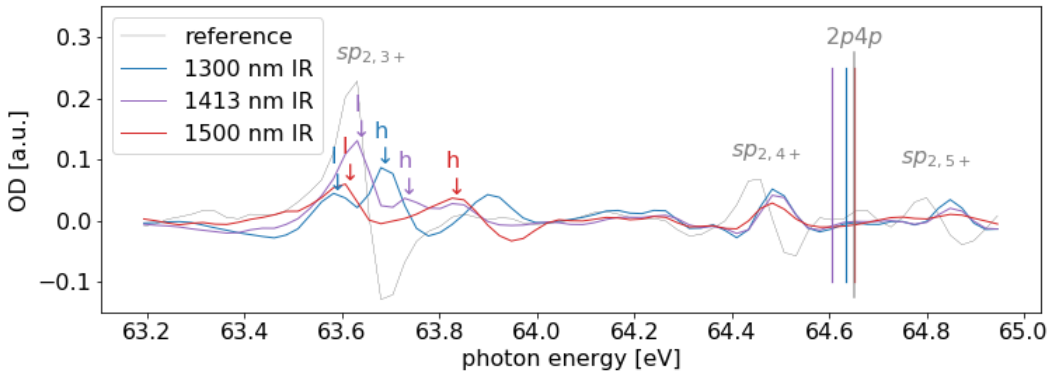

Figure 5.4.: **The $sp_{2,\{3,5,..\}+}$ states for intermediate intensity**
A detailed view of the OD of fig.(5.3) is presented for the DES lying above 63 eV for the intermediate case of the 1300 nm perturbative IR (blue) as well as for the higher-mediate cases of the 1413 nm IR (violet) and 1500 nm IR (red). The vertical lines represent the (estimated) position of the $2p4p$ 'dark' state, which is spectroscopically not visible. The $sp_{2,3+}$ state undergoes an Autler-Towns splitting for the (nearly) resonant IR wavelength of 1300 nm. The energetically lower lying peaks of this splitting are depicted as 'l', the higher lying ones as 'h'. Further explanations are given in the text.

found in the absorption spectra before the intensity is too large and completely ionizes these states. First, the lower-medium intensity case is considered. As (fig.(5.3 b2,c2)) show, the $sp_{2,3+}$ line shape is modified towards a more symmetrical line. This behaviour is known from the previous measurement utilizing a 800 nm IR pulse [33]. There, the line shape change is explained with an impulsive, intensity dependent energy shift leading to an shifted dipole phase and thus manipulated Fano q parameter, similar to the numerical analysis chapter (eq.(4.10)). But in the IR regime, rather a (offresonant) ponderomotive shift is the source of this manipulated line shape than a resonant coupling mechanism as discussed for the XUV pulses. Following eq.(1.16), this energy shift increases with the laser pulses central wavelength. Therefore, the $sp_{2,3+}$ profile is stronger manipulated for the 1500 nm driving SWIR than for the 1400 nm pulse (under the assumption that the intensity stays constant) and appears more symmetric in fig.(5.3 c2) than in fig.(5.3 b2)). In comparison to [33], the IR pulse duration is much longer and especially too long for the $2s2p$ resonance (decaying within $\sim$ 17 fs) to impulsively manipulate it.

In addition, the upper lying states $sp_{2,\{4,5,..\}+}$ are manipulated in a similar manner for the higher-medium intensity case. All of their line shapes appear symmetric (Lorentzian-like) for the three different IR wavelengths as a detailed view in fig.(5.4) shows. Since their amplitudes are close to vanish, they are not

investigated in more detail. Instead, another interesting feature seems to appear looking more closely at the $sp_{2,3+}$ resonance. For all three IR wavelengths, a kind of double structure is evident at the $sp_{2,3+}$ resonance position. The left peak, located at lower photon energies and depicted with an 'l', coincides with the unperturbed Fano line peak (grey) and is not shifted with the IR wavelength significantly. In contrast, the second peak at higher photon energies ('h') is located close to the first peak for the 1300 nm IR (blue) and moves towards higher photon energies with increasing IR wavelength (1413 nm: violet, 1500 nm: red). These features can be understood looking at tab.(1.3): The $^1D^e$ $2p4p$ 'dark' state is nearly in resonance to the $sp_{2,3+}$ state for the 1300 nm IR. They can be coupled, as such a coupling would fulfill the change of angular momentum $\Delta L = \pm 1$ and a change of parity as mandatory for an optical dipole transition. From the $2p4p$ state, located at $\sim$ 64.65 eV a spectroscopically visible $|2p4p, -1\rangle$ light-induced state (LIS) can be generated by stimulated emission of an IR photon as described in the theory chapter (sec.(1.4.4)). Since the $2p4p$ state lies energetically above the $sp_{2,3+}$ state, this LIS is located in agreement with the experiment at highest photon energies for the largest IR wavelength corresponding to the smallest IR photon energy (given in tab.(5.1)). Hence, for the 1500 nm IR pulse, the LIS is off-resonant with the $sp_{2,3+}$ state, whereas in the case of the 1300 nm IR pulse, the LIS becomes nearly resonant with the $sp_{2,3+}$ (with a detuning $\Delta = 30$ meV) and therefore leads to an Autler-Townes splitting of that state. For the 1413 nm pulse, the intermediate state in form of a detuned coupling seems to be the case. To support this assumption, the position of the $2p4p$ state is determined from the measurement. To achieve this, the positions of the LIS are defined to be at the 'h'-peak maxima. The corresponding IR photon energy is added to these positions and the resulting positions of the $2p4p$ state is marked in fig.(5.4) as a vertical line in the corresponding colour. The literature value of the $2p4p$ resonance is added as a grey vertical line. For a quantitative comparison, the three experimentally determined values for the $2p4p$ resonance position E_{2p4p} as well as their average and the literature value are summarized in the following table:

	1300 nm	1413 nm	1500 nm	average	literature
E_{2p4p}	64.63 eV	64.61 eV	64.65 eV	64.63 ± 0.02 eV	64.65 eV

Table 5.3.: Estimated 2p4p resonance position compared to literature value

All of the determined resonance positions for the three independent measurements at different OPA wavelengths agree to the average value within 20 meV, which is determined as the average's error, because a statistical error for three values is not meaningful. Taking into account these uncertainty, it is remark-

able to observe the averaged resonance position in good agreement to the literature value. Therefore, this first analysis supports the idea of a LIS generated from the $2p4p$ dark state leading to an Autler-Towns splitting for the resonant case.
In summary, the IR intensity dependent study of the DES has expanded the measurments in [33]. The ponderomotive shifts introduced in that study are supported to be wavelength dependent. Furthermore, the increased IR wavelength allows for coupling between states other than the $2s2p$ resonance, which is kept nearly unperturbed. The transition of an offresonant LIS from the $2p4p$ state to a resonant Autler-Townes splitting of the $sp_{2,3+}$ resonance was measured by increasing the IR photon energy by ~ 100 meV. With this, IR wavelength specific manipulations of the DES in helium are proven to be possible with the OPA laser system.

5.2.2. Time-Resolved Study of Doubly-Excited Helium

To further increase the insight into the electron dynamics taking place within the helium atom, a time delay between the XUV pulse and the SWIR pulse is introduced as described in chapter (2.2). This allows for a time-delay scan (TDS) of the DES, which has been carried out for two central wavelengths of the SWIR pulses: 1240 nm and 1413 nm. The results for the measured time-resolved spectral OD are presented in fig.(5.5(a1)) and fig.(5.5(b1)), respectively for the two wavelengths. They are compared to few-level simulations introduced in section (4.1.1), which are shown in fig.(5.5(a2),(b2)).
For the discussion of results, the features of the measured TDS for the 1240 nm IR will be considered first. Thereafter, the results will be compared to the experimental 1413 nm perturbation pulse TDS, before both measurements will be compared to the simulations.

Looking at the experimental 1240 nm TDS in fig.(5.5(a1)), several physical features for the visible $2s2p$, $sp_{2,\{3,4,5,6\}+}$ states are evident. First, the $2s2p$ resonance located at 60.15 eV is manipulated significantly less compared to the predecessor measurement carried out with a 800 nm IR pulse in [69]. In latter case, a strong manipulation of the $2s2p$ resonance was achieved by a two-photon coupling to the $sp_{2,3+}$ state enhanced by the energetically intermediate and spectroscopically dark $2p^2$ state. Here, the IR wavelength is tuned to be offresonant for this coupling, and to any other state, thus leaving the $2s2p$ state less modified. Yet, a small perturbation is nevertheless noticeable, which can be explained with a residual, detuned coupling to the $2p^2$ resonance. It becomes spectroscopically visible in form of the $|2p^2, -1\rangle$ light-induced state (LIS) located one IR photon energy ($E_{IR} = 1$ eV) lower than the $2p^2$ resonance position ($E_{2p^2} = 62.09$ eV) at ~ 61.1 eV. Despite the detuning, this LIS is clearly visible due to a large dipole moment between the $2s2p$ and $2p^2$ states:

(a) 1240 nm IR perturbation pulse

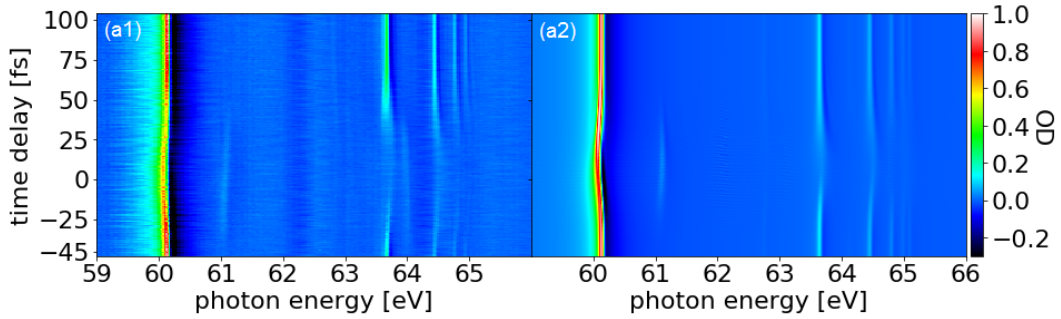

(b) 1413 nm IR perturbation pulse

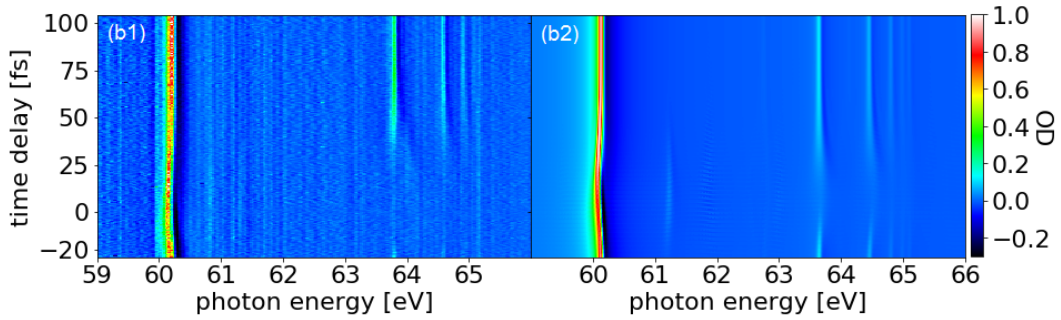

Figure 5.5.: **Time-delay scans of the spectral OD for two different IR perturbation pulse wavelengths**
The spectral OD is measured depending on the time-delay between IR and XUV pulse for a IR pulse of $\lambda_c = 1240$ nm, shown in (a) and for $\lambda_c = 1413$ nm in (b). The experimental data in (a1) and (b1) is compared to few-level simulations presented in (a2), (b2), respectively. The physical effects occurring in the plots are discussed in the text.

$d = 2.17$ a.u. [70]. In temporal overlap of the XUV and IR pulses, the LIS shifts slightly towards higher photon energies, whereas the $2s2p$ state moves slightly into the other direction, the result of a (far-)detuned Stark-shift. In addition, a second LIS is evident located at ~ 64 eV. Its origin is yet to be determined, because it lies one photon energy lower than many of the $n_1 = 2$ Rydberg states, so that it cannot be distinguished easily from which state it is generated. Furthermore, the $sp_{2,\{3,4,5,6\}+}$ states are manipulated stronger than the $2s2p$ state. All of them shift towards higher photon energies, what is most pronounced in temporal overlap. Additionally, the amplitudes of the resonances are decreased within the same temporal window, a strong-field ionization (SFI) effect occurring when the intense IR pulse is present. To evaluate what kind of SFI is observed, the simulations discussed below will be used as a comparison. Eventually, it should be noted that two faint lines just above the

noise threshold are visible for positive time delays at ~ 62.8 eV and ~ 64.1 eV, where the $sp_{2,3-}$ and $sp_{2,4-}$ states of the weaker '-' manifold are possible candidates.

In comparison to these findings, the experimental results for the 1413 nm IR TDS shown in fig.(5.5(b1)) present a slightly different picture: The $sp_{2,\{3,..\}+}$ states seem to vanish completely around zero time delay. Therefore, a shift of the states cannot be observed. Yet, looking at the line shapes at the transition between unperturbed and vanished resonances, a first sign of such shifts is present. Also, the two LIS evident in the case of a 1240 nm perturbation pulse are not clearly visible anymore. Although, the LIS near to the $2s2p$ resonance is expected to be around $(61.2 - 61.3)$ eV, where a signature of it might be present. Yet, the general noise floor of the 1413 nm TDS, which was measured first under likely not perfect conditions, is much larger than for the previously discussed TDS. Hence, for features as the line shifts and LIS, which are low in amplitude, it cannot be clarified, whether they are not present or just not visible due to the noise.

For a comparison to a theoretical model, the few-level framework presented in sec.(4.1.1) is utilized including all the resonances listed in tab.(1.3). As the computing time is much larger for the 22 states than for the simple two- and three-level systems discussed in sec.(4.2), a ionization continuum is not included implicitly, putting the focus of the numerical approach on the couplings between DESs instead of the continuum interaction. The autoionizing properties of the DES are included in a simplified manner: Their fast decay times are included within the spectral line width, which is added in the imaginary part of the states eigenenergies. The absorption Fano profiles are included in the phase shifts connected to the Fano q-parameters (eq.(1.58)) introduced as an initial phase offset of the temporal state coefficients. The dipole moments from the ground state to the $^1P^e$ states are adjusted manually to match the experimental resonance amplitudes. The weak XUV pulse is treated as initial excitation process described by perturbation theory and is disregarded afterwards. Therefore, a single Gaussian pulse of 0.25 fs duration is chosen instead of the more complex HHG pulse train, to cover the complete spectral region of the DESs. The couplings between the DESs are in contrast to that calculated within the few-level framework. For that purpose, the IR pulses are modelled as Gaussian pulses centred at the corresponding central wavelength. Their durations are set to be 40 fs, an upper estimation of the durations found within the FROG measurements of similar OPA pulses (see tab.(3.3)). The estimation of all involved dipole moments between the DESs is yet connected to the largest uncertainties of the simulation. Although it is possible to calculate them with atomic structure theory, this would go beyond the scope of this thesis. Thus, they can be regarded as free parameters of the

system to be adjusted to match the experimental data. The values utilized in this simulation are included in tab.(D.1) presented in the appendix. Note that the dipole moments between the $2p^2$ state to the $2s2p$ and $sp_{2,3+}$ states are taken from [70]. With this given value for $d_{2s2p,2p^2}$, the peak intensity of the IR pulses is set to $2 \cdot 10^{12}$ $^{\mathrm{W}}/_{\mathrm{cm}^2}$ to agree with the measured modification of the $2s2p$ resonance as well as the intensity of the $|2p^2, -1\rangle$ LIS. Furthermore, with this intensity estimation, the Keldysh parameter introduced in eq.(1.15) is calculated to be ~ 1 for the peak intensity, increasing with the decreasing pulse envelope. Thus, the MPI is assumed to be the SFI process taking place in the experiments. To include it in the simulations, the eigenstate coefficients are damped following first order rate equation (see [45] for further information) with the factor: $\exp\left(-\sigma^{(n)}(I(t)/\omega_c)^n\right)$, where n stands for the number of photons necessary, $\sigma^{(n)}$ for the n-photon ionization cross section, $I(t)$ for the time dependent intensity of the pulse (in a.u.) and ω_c for the central photon frequency (in a.u.). The ionization cross sections are set to the values given in tab.(D.2) in the appendix up to $n = 3$. Larger number photon ionization processes are highly unlikely and thus disregarded. Last, the convolution of the spectrometer is taken into account by convolving the simulated spectral OD with a Gaussian function of 62 meV FWHM, as found in the intensity dependent measurements for the unchanged spectrometer slit of 200 μm width.

The simulation results for the 1240 nm pulse shown in fig.(5.5(b2)) are in good agreement with its experimental counterpart. With the choice of dipole moments as in tab.(D.1) the couplings between the DESs can be adjusted to match the experimentally measured shift towards higher photon energies in temporal overlap, most evident for the $sp_{2,\{3,4\}+}$ states. Also, the MPI depletes the energetically higher lying states around time delay zero again agreeing with the experiment. Furthermore, the LIS around 61.1 eV is clearly visible, whereas the second one measured at ~ 64 eV, is absent. This is most likely connected to a wrong choice of dipole moments between the near lying states. The two weak '-' states, $sp_{2,\{3,4\}-}$, are as faint noticeable as in the experiment. Note, that the IR dependent features, e.g. the depletion of resonances and the LIS at 61.1 eV appear in a slightly smaller time window as in the experiment. An underestimation of the IR pulse duration would explain this, as the pulse duration was not insitu characterized.
For the 1413 nm IR pulse simulation in fig.(5.5(b2)), the previously discussed features are similar, yet not identical to the 1240 nm case. The one evident LIS is shifted slightly towards higher photon energies, supporting the statement that it is generated from the energetically higher lying $2p^2$ state. Furthermore, the effects of the MPI occur more pronounced than for the 1240 nm pulse. Also, the $sp_{2,3}+$ state appears less shifted in temporal overlap, whereas the $sp_{2,4}+$ state is shifted to even higher photon energies. A comparison to the

experiment is hard to make, again because of the higher noise level of the measured TDS plot. Nevertheless, the main trends of the simulation and experiment are in agreement with each other.

Although the few-level simulations are a simplified numerical framework, its high degree of control over the input parameters helps to adjust strong field effects of any kind. For example, the MPI can be included and adjusted by varying the ionization cross sections. Thus, its effects on the simulated TDS can be pointed out simply by comparing simulations with and without the MPI. Such a comparison is shown in fig.(D.1) in the appendix. In fig.(D.1 b) the case without MPI is presented, clearly showing that the states of the '+' manifold do not decrease when the MPI effects are absent.
The same kind of comparison is carried out for the spectral convolution. The simulation results without the convolution are presented in c) of fig.(D.1), showing that several minor spectral details of the line shape modifications cannot be measured with this resolution and thus will not be discussed further.
As mentioned beforehand, the choice of the dipole moments between the DES is crucial for the correct simulation results. For the two measured TDS, the degrees of freedom are too large to estimate all of the dipole moments. Nevertheless, the simulated TDS prove that the exploited numerical framework is capable to reproduce the experimental data and furthermore to point out which of the dipole moments play a central role for a given measurement. The dipole moments in tab.(D.1) at the order of ~ 1 a.u. are necessary to describe the experiments, whereas dipoles values ≈ 0.01 a.u. indicate that these couplings can be neglected. In general, experiments which systematically vary the IR wavelength and intensity, should generate a data set large enough to determine a larger set of dipole moments with greater precision by comparing to theoretical predictions.

In total, the here presented measurements show a first prospect of the OPA laser system's capabilities. With the IR perturbation pulse wavelength shifting to the SWIR region, different manipulations of the $n_1 = 2$ DES manifold were measured: A shift of the resonance positions of the $sp_{2,\{3,4,..\}+}$ state is evident while the $2s2p$ state is nearly unperturbed. Also, the effects of MPI on these states was presented. Maybe most interestingly, the generation of an offresonant and thus unperturbed LIS was achieved and supported with simulations. Investigating the properties of LISs will be the aim of further studies.

6. Conclusion and Outlook

The goal of this scientific work has been the investigation of electron-electron correlations and light-matter interaction, which are fundamental for chemical bounds and solid state properties. Therefore, the benchmark system of helium was chosen to be investigated in the strong-field regime of light-matter interaction – experimentally as well as numerically. For that purpose, ultrafast and -strong laser pulses were utilized. The focus was thereby the variation of the pulses' central wavelength, both in the XUV and IR regime.

The technical part was a key task of this thesis project. A Ti:Sa based laser system was installed including the final OPA stage, which allows for the laser pulse wavelength tunability in the short-wavelength infrared (SWIR). In near future it should be possible to generate high harmonics with this system in the 'water-window' (280 eV - 530 eV) [71]. The can be used in further studies of biochemical relevant atoms and molecules. Also combinations of the Ti:Sa output and the signal and idler OPA outputs can be used to generate high harmonics independently from an externally coupled-in IR perturbation pulse. The two main HE and LE outputs of the Ti:Sa and a choice of OPA outputs were characterized by the in this project build FROG setup. The pulse characterization was carried out successfully, proving the capabilities of the FROG setup as well as confirming the expected pulse properties. A beam stabilization is yet recommended for reduction of the beam pointing fluctuations. For the future, the FROG characterization could be carried out in situ to experiments, as a low intensity reflection or transmission of the utilized pulses from a mirror as close as possible to the vacuum chamber entrance can be used for the pulse characterization.

From the scientific point of view, the interaction of ultrashort and -strong laser pulses with the helium atom was investigated with the help of strong field spectroscopy (SFS) in two different wavelength regimes.
First, the coupling of the ground to an autoionizing excited state was studied with pulses in the XUV spectral regime. The numerical analysis has pointed out, that the absorption line of a simple two-level systems can be manipulated to become Fano-like. This is found as a result of Rabi-like coupling inducing a Stark shift. These shifts are anti-symmetric with the pulse detuning, whereas the autoionizing properties of doubly-excited states break this symmetry. This model was expanded with partially coherent FEL pulses to be capable of de-

scribing the line-shape change of the $2s2p$ resonance in helium measured with first SFS experiments at FLASH.
Additionally, a combination of intense OPA SWIR pulses and their high harmonics were utilized to investigate the couplings between doubly-excited states of helium expanding previous measurements with a 800 nm IR perturbation pulse. The tunability of the SWIR pulses allows for switching from the resonant coupling of the $2s2p$ state to the $sp_{2,3+}$, evident in form of an Autler-Townes splitting, to the generation of an offresonant LIS. Additionally, within an intensity dependent measurement, the line shapes of the DES were successfully manipulated to become Lorentzian-like. Furthermore, a time-delay scan allows to make LIS visible within a window of several fs corresponding to the pulse duration. This can be regarded as prove-of-principle starting point for further investigations, asking: Do the LIS encode the properties of the generating spectroscopic dark states? How does their time evolution change under the detuning of the IR pulses? For optimal investigations of this questions, a better spectral resolution and the use of few-cycle OPA pulses are regarded to be helpful improvements.

In summary, strong field effects in both wavelength regimes, XUV and IR, were measured and explained supported by simulations. Especially the variation of the laser pulses' intensity was essential for the presented scientific output. The time resolved study combining SWIR pulses and high harmonics can be regarded as prove-of-principle measurements. More systematic experiments by variation of the IR pulses' intensity and wavelength could answer questions about LISs and dipole couplings of the DESs in helium. Furthermore, time resolved studies with FEL XUV pulses were carried out just recently. Their evaluation is supposed to give further insight into the electron-correlations, eventually leading in (near) future to a description of the helium atom as close as possible to an analytical one. Overall, the work presented in this thesis helped to develop the tools and mechanisms to gain deeper insights into the electron correlations within helium. This is expected to smooth the way for prospective electron-correlation studies in more complex systems.

Bibliography

1. Diels, J.-C. & Rudolph, W. *Ultrashort laser pulse phenomena* (Elsevier/Academic Press, 2006).
2. Goodman, J. W. *Introduction to Fourier optics* (McGraw-Hill, 1968).
3. Assefa, S., Xia, F. & Vlasov, Y. A. Reinventing germanium avalanche photodetector for nanophotonic on-chip optical interconnects. *Nature* **464** (2010).
4. Armstrong, J. A. MEASUREMENT OF PICOSECOND LASER PULSE WIDTHS. *Applied Physics Letters* **10,** 16–18 (1967).
5. Trebino, R. *et al.* Measuring ultrashort laser pulses in the time-frequency domain using frequency-resolved optical gating. *Review of Scientific Instruments* **68,** 3277–3295 (1997).
6. Trebino, R. & Kane, D. J. Using phase retrieval to measure the intensity and phase of ultrashort pulses: frequency-resolved optical gating. *J. Opt. Soc. Am. A* **10,** 1101–1111 (May 1993).
7. Kane, D. J. & Trebino, R. Characterization of arbitrary femtosecond pulses using frequency- resolved optical gating. *IEEE Journal of Quantum Electronics* **29,** 571–579 (Feb. 1993).
8. Iaconis, C. & Walmsley, I. A. *Spectral phase interferometry for direct electric-field reconstruction of ultrashort optical pulses* in *Technical Digest. Summaries of Papers Presented at the Conference on Lasers and Electro-Optics. Conference Edition. 1998 Technical Digest Series, Vol.6 (IEEE Cat. No.98CH36178)* (May 1998), 518–.
9. Iaconis, C. & Walmsley, I. A. Self-referencing spectral interferometry for measuring ultrashort optical pulses. *IEEE Journal of Quantum Electronics* **35,** 501–509 (Apr. 1999).
10. Miranda, M., Fordell, T., Arnold, C. & and Helder Crespo, A. L. Simultaneous compression and characterization of ultrashort laser pulses using chirped mirrors and glass wedges. *Opt. Express* **20,** 688–697 (Jan. 2012).
11. Boyd, R. W. *Nonlinear optics* (Academic Press, 2008).
12. Keldysh, L. V. Ionization in the field of astrong electromagnetic wave. *Soviet Physics JETP* **20** (1307 1965).

13. Popov, V. S. Tunnel and multiphoton ionization of atoms and ions in a strong laser field (Keldysh theory). *Physics-Uspekhi* **47,** 855 (2004).

14. Corkum, P. B. Plasma perspective on strong field multiphoton ionization. *Phys. Rev. Lett.* **71,** 1994–1997 (13 Sept. 1993).

15. Paul, P. M. *et al.* Observation of a Train of Attosecond Pulses from High Harmonic Generation. *Science* **292,** 1689–1692 (2001).

16. Lewenstein, M., Balcou, P., Ivanov, M. Y., L'Huillier, A. & Corkum, P. B. Theory of high-harmonic generation by low-frequency laser fields. *Phys. Rev. A* **49,** 2117–2132 (3 Mar. 1994).

17. Sakurai, J. J. & Commins, E. D. Modern Quantum Mechanics, Revised Edition. *American Journal of Physics* **63,** 93–95 (1995).

18. Lefebvre, R. & Smeyers, Y. G. Extended Hartree–Fock calculations for the helium ground state. *International Journal of Quantum Chemistry* **1,** 403–419.

19. Herrick, D. R. & Sinano ğlu, O. Comparison of doubly-excited helium energy levels, isoelectronic series, autoionization lifetimes, and group-theoretical configuration-mixing predictions with large-configuration-interaction calculations and experimental spectra. *Phys. Rev. A* **11,** 97–110 (1 Jan. 1975).

20. Janzen, A. R. & Aziz, R. A. An accurate potential energy curve for helium based on ab initio calculations. *The Journal of Chemical Physics* **107,** 914–919 (1997).

21. Burgers, A., Wintgen, D. & Rest, J. .-.-M. Highly doubly excited S states of the helium atom. *Journal of Physics B: Atomic, Molecular and Optical Physics* **28,** 3163 (1995).

22. Rost, J. M., Schulz, K., Domke, M. & Kaindl, G. Resonance parameters of photo doubly excited helium. *Journal of Physics B: Atomic, Molecular and Optical Physics* **30,** 4663 (1997).

23. Sanchez, I., Bachau, H. & Cormier, E. Theory of two-photon spectroscopy of autoionizing states in helium and beryllium. *Journal of Physics B: Atomic, Molecular and Optical Physics* **28,** 2367 (1995).

24. Hicks, P. J. & Comer, J. Ejected electron spectroscopy of autoionizing states excited by low energy electron impact. *Journal of Physics B: Atomic and Molecular Physics* **8,** 1866 (1975).

25. NIST-ASD-Team. *NIST Atmoic Spectra Database* `https://www.nist.gov/pml/atomic-spectra-database` (2018).

26. Fano, U. Effects of Configuration Interaction on Intensities and Phase Shifts. *Phys. Rev.* **124,** 1866–1878 (6 Dec. 1961).

27. Steck, D. A. *Quantum and Atom Optics* (available online at http://steck.us/teaching (revision 0.8.3), 2012).

28. Rabi, I. I. Space Quantization in a Gyrating Magnetic Field. *Phys. Rev.* **51,** 652–654 (8 Apr. 1937).

29. Autler, S. H. & Townes, C. H. Stark Effect in Rapidly Varying Fields. *Phys. Rev.* **100,** 703–722 (2 Oct. 1955).

30. Ott, C. *Attosecond multidimensional interferometry of single and two correlated electrons in atoms* Dissertation (2012).

31. Bransden, B. & Joachain, C. *Physics of atoms and molecules* (Prentice Hall, Harlow, Munich, 2003).

32. R. Feynman, R. L. & Sands, M. *The Feynman Lectures on Physics* (Addison-Wesley, 1963).

33. Ott, C. *et al.* Lorentz Meets Fano in Spectral Line Shapes: A Universal Phase and Its Laser Control. *Science* **340,** 716–720 (May 2013).

34. Schawlow, A. L. & Townes, C. H. Infrared and Optical Masers. *Phys. Rev.* **112,** 1940–1949 (6 Dec. 1958).

35. Maiman, T. H. Stimulated Optical Radiation in Ruby. *Nature* **187,** 493 (1960).

36. Giordmaine, J. A. & Miller, R. C. Tunable Coherent Parametric Oscillation in $LiNbO_3$ at Optical Frequencies. *Phys. Rev. Lett.* **14,** 973–976 (24 June 1965).

37. Akhmanov, S. A., Kovrigin, A. I., Piskarskas, A. S., Fadeev, V. V. & Khokhlov, R. V. Observation of Parametric Amplification in the Optical Range. *JETP Letters* **2,** 191 (1965).

38. Strickland, D. & Mourou, G. Compression of amplified chirped optical pulses. *Optics Communications* **55,** 447–449. ISSN: 0030-4018 (1985).

39. Spence, D. E., Kean, P. N. & Sibbett, W. 60-fsec pulse generation from a self-mode-locked Ti:sapphire laser. *Opt. Lett.* **16,** 42–44 (Jan. 1991).

40. *Coherent webpage* `https://www.coherent.com/`.

41. *Light Conversion webpage* `http://lightcon.com/`.

42. Brabec, T. & Krausz, F. Intense few-cycle laser fields: Frontiers of nonlinear optics. *Rev. Mod. Phys.* **72,** 545–591 (2 Apr. 2000).

43. Jones, D. J. *et al.* Carrier-Envelope Phase Control of Femtosecond Mode-Locked Lasers and Direct Optical Frequency Synthesis. *Science* **288,** 635–639. ISSN: 0036-8075 (2000).

44. Baumgartner, R. & Byer, R. Optical parametric amplification. *IEEE Journal of Quantum Electronics* **15,** 432–444 (June 1979).

45. Ding, T. *Quantum dynamics in weak and strong fields measured by XUV nonlinear spectroscopy* Dissertation (2018).

46. Rebholz, M. *Design and construction of an experimental setup for multi-dimensional spectroscopy in the XUV/ soft-X-ray spectral region* Master thesis (2016).

47. Aufleger, L. *Measurement of electron dynamics in atoms and molecules with intense XUV FEL radiation* Master thesis (2016).

48. *Princeton Instruments webpage* `https://www.princetoninstruments.com/index.cfm`.

49. Rupprecht, P. *Optical Laser Source Development at the X-ray Free-Electron Laser LCLS* master thesis (2016).

50. *SmarAct/Technology webpage* `http://www.smaract.com/technology/`.

51. Fittinghoff, D. N., DeLong, K. W., Trebino, R. & Ladera, C. Noise sensitivity in frequency-resolved optical-gating measurements of ultrashort pulses. *J. Opt. Soc. Am. B* **12,** 1955 (1995).

52. Ackermann, W. *et al.* Operation of a free-electron laser from the extreme ultraviolet to the water window. *Nature Photonics* **1.** Article, 336 EP - (June 2007).

53. Ding, T. *et al.* Nonlinear coherence effects in transient-absorption ion spectroscopy with stochastic extreme-ultraviolet free-electron-laser pulses. *submitted at PRL* (2018).

54. Ott, C. *et al.* First transient absorption spectroscopy experiments in Helium at FLASH. *in preparation* (2016).

55. Hartmann, N. *et al.* Attosecond time-energy structure of X-ray free-electron laser pulses. *Nature Photonics* **12,** 215–220. ISSN: 1749-4893 (2018).

56. Reiche, S. GENESIS 1.3: a fully 3D time-dependent FEL simulation code. *Nuclear Instruments and Methods in Physics Research Section A: Accelerators, Spectrometers, Detectors and Associated Equipment* **429,** 243–248. ISSN: 0168-9002 (1999).

57. Tanaka, T. Numerical methods for free electron laser simulations. *Journal of Electromagnetic Waves and Applications* **32,** 371–401 (2018).

58. Pfeifer, T., Jiang, Y., Düsterer, S., Moshammer, R. & Ullrich, J. Partial-coherence method to model experimental free-electron laser pulse statistics. *Opt. Lett.* **35,** 3441–3443 (Oct. 2010).

59. Lambropoulos, P. & Zoller, P. Autoionizing states in strong laser fields. *Phys. Rev. A* **24,** 379–397 (1 July 1981).

60. Artemyev, A. N., Cederbaum, L. S. & Demekhin, P. V. Impact of intense laser pulses on the autoionization dynamics of the $2s2p$ doubly excited state of He. *Phys. Rev. A* **96,** 033410 (3 Sept. 2017).

61. Mouloudakis, G. & Lambropoulos, P. Autoionizing states driven by stochastic electromagnetic fields. *Journal of Physics B: Atomic, Molecular and Optical Physics* **51,** 01LT01 (2018).

62. Domke, M., Schulz, K., Remmers, G., Kaindl, G. & Wintgen, D. High-resolution study of $^1P^o$ double-excitation states in helium. *Phys. Rev. A* **53,** 1424–1438 (3 Mar. 1996).

63. Magunia, A. *Elektronen-Korrelation in Helium unter Einfluss intensiver XUV-Felder* Bachelor thesis (2016).

64. Röhrs, M., Gerth, C., Schlarb, H., Schmidt, B. & Schmüser, P. Time-resolved electron beam phase space tomography at a soft x-ray free-electron laser. *Phys. Rev. ST Accel. Beams* **12,** 050704 (5 May 2009).

65. Driever, S. *et al.* Near infrared few-cycle pulses for high harmonic generation. *Journal of Physics B: Atomic, Molecular and Optical Physics* **47,** 204013 (2014).

66. Midorikawa, K. High-Order Harmonic Generation and Attosecond Science. *Japanese Journal of Applied Physics* **50,** 090001 (2011).

67. Christov, I. P., Murnane, M. M. & Kapteyn, H. C. High-Harmonic Generation of Attosecond Pulses in the "Single-Cycle" Regime. *Phys. Rev. Lett.* **78,** 1251–1254 (7 Feb. 1997).

68. *CXRO wbpage: X-Ray Interactions With Matter* `http://henke.lbl.gov/optical_constants/filter2.html`.

69. Ott, C. *et al.* Reconstruction and control of a time-dependent two-electron wave packet. *Nature* **516,** 374 EP - (Dec. 2014).

70. Loh, Z.-H., Greene, C. H. & Leone, S. R. Femtosecond induced transparency and absorption in the extreme ultraviolet by coherent coupling of the He 2s2p (1Po) and 2p2 (1Se) double excitation states with 800nm light. *Chemical Physics* **350,** 7–13 (2008).

71. Takahashi, E. J., Kanai, T., Ishikawa, K. L., Nabekawa, Y. & Midorikawa, K. Coherent Water Window X Ray by Phase-Matched High-Order Harmonic Generation in Neutral Media. *Phys. Rev. Lett.* **101,** 253901 (25 Dec. 2008).

72. *The NIST References on Constants, Units and Uncertainty* `https://www.nist.gov/cuu/Constants/` (2018).

A. Detailed Scheme of the Laser System

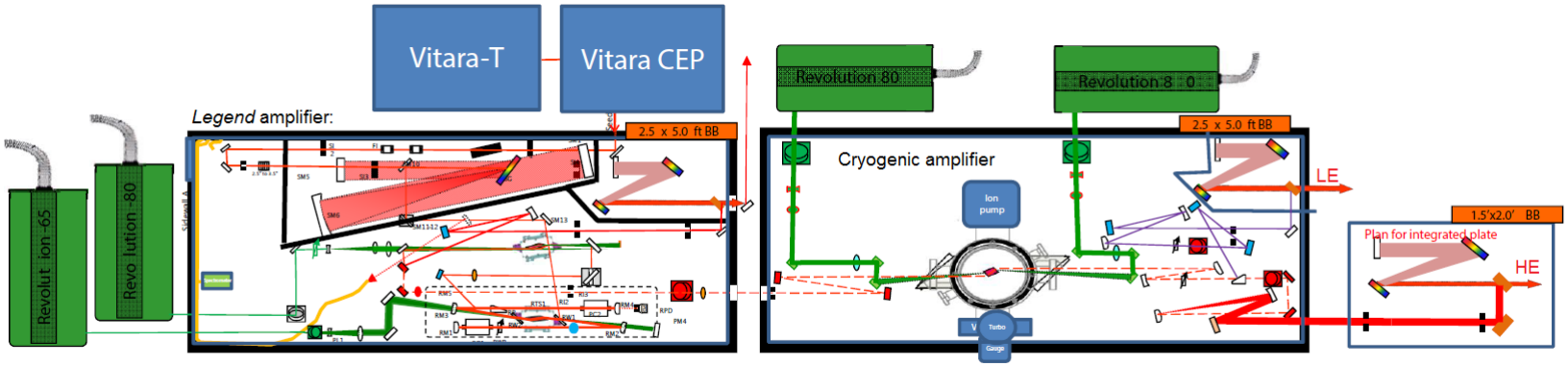

Figure A.1.: **Laser system - detailed scheme**

In comparison to fig.(2.1), the insides of the *Legend* and *Cryo* amplifier are shown, including the beam path. *Vitara-T*,*Vitara-CEP* and *Revolution* are the *Coherent* product names of the oscillator, CEP-stabilization and pump lasers, respectively.

B. Additional FROG Data

B.1. Spectra and SPIDER Measurements of the HE and LE Pulses

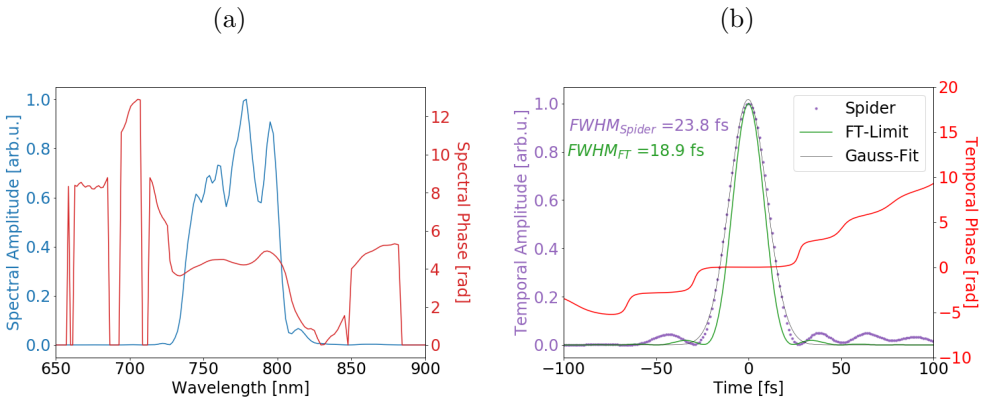

Figure B.1.: **Spectral FROG-retrieval (a) and full temporal SPIDER-characterization (b) for the HE pulse in section (3.2).**

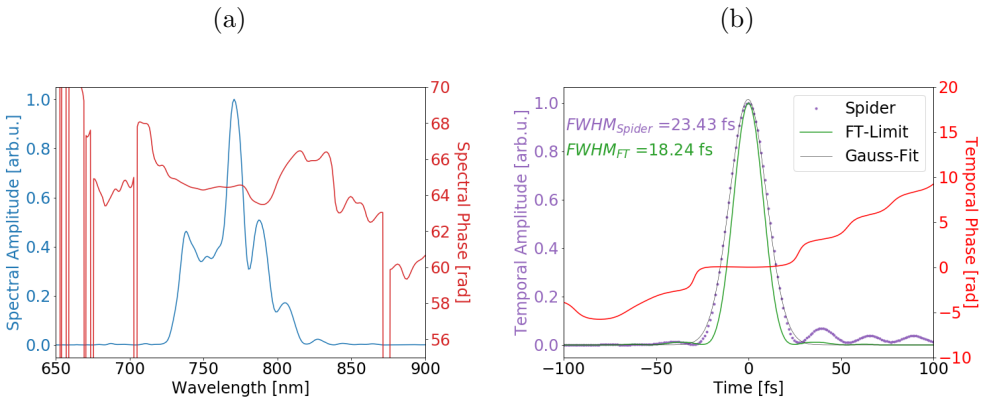

Figure B.2.: **Spectral FROG-retrieval (a) and full temporal SPIDER-characterization (b) for the LE pulse in section (3.2).**

B.2. FROG Traces of the OPA Signal Pulses

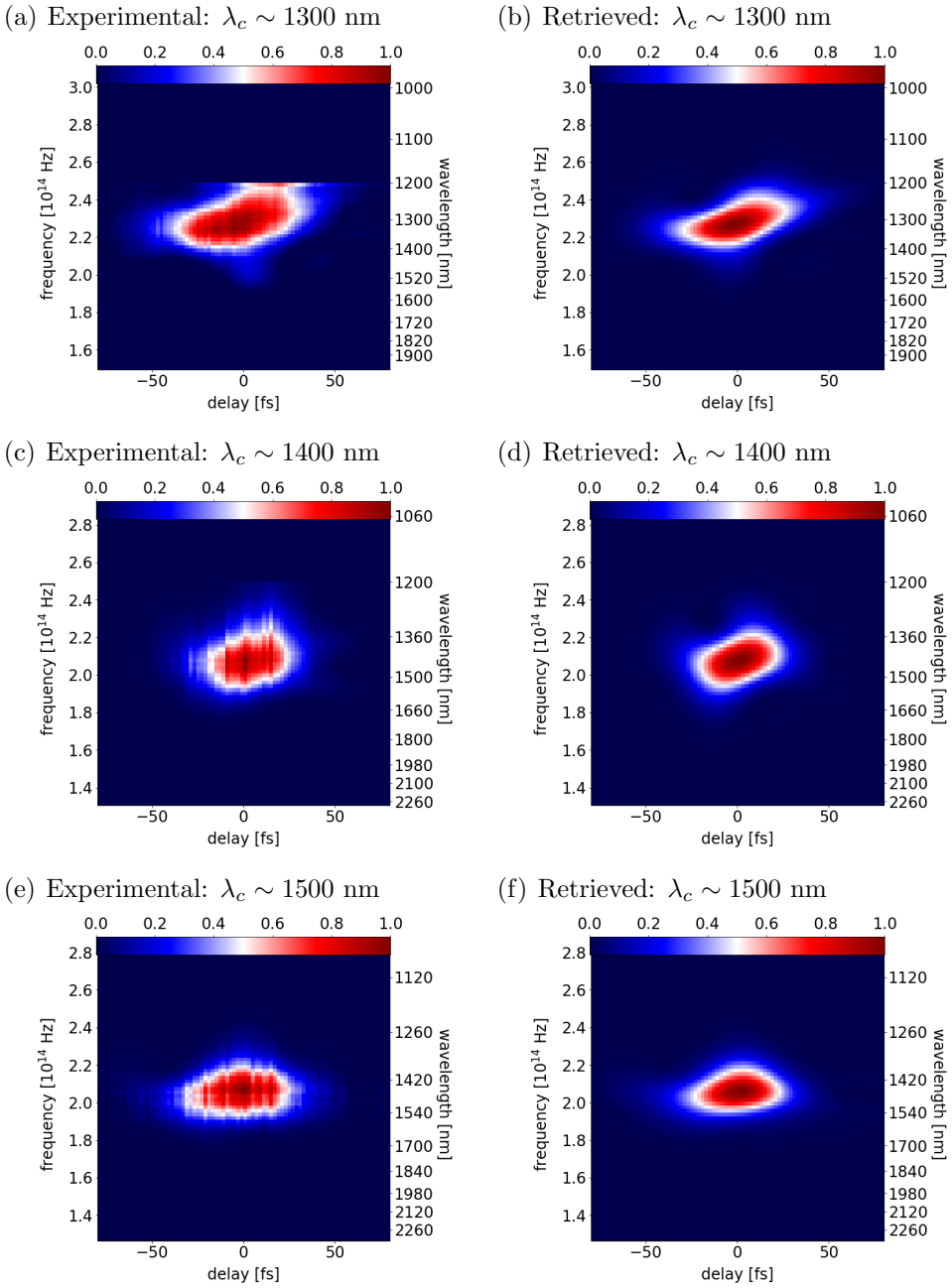

Figure B.3.: **Experimental and retrieved FROG traces of the three OPA signal pulses presented in section (3.3).**

B.3. TOPAS calibration settings for presented output pulses

Settings	$\lambda_c \sim 1300$ nm	$\lambda_c \sim 1400$ nm	$\lambda_c \sim 1500$ nm
Power [W] (signal & idler)	6.6	6.1	$5.6 - 5.7$
c_1	9420	9887	10368
d_1	8090	7860	7761
c_2	15315	15859	16468
d_2	27782	27926	27946
c_3	15363	15997	16504
d_3	5437	5430	54350

Table B.1.: TOPAS settings for the signal pulses discussed in section (3.3)

B.4. FROG Measurement of TOPAS Idler Output

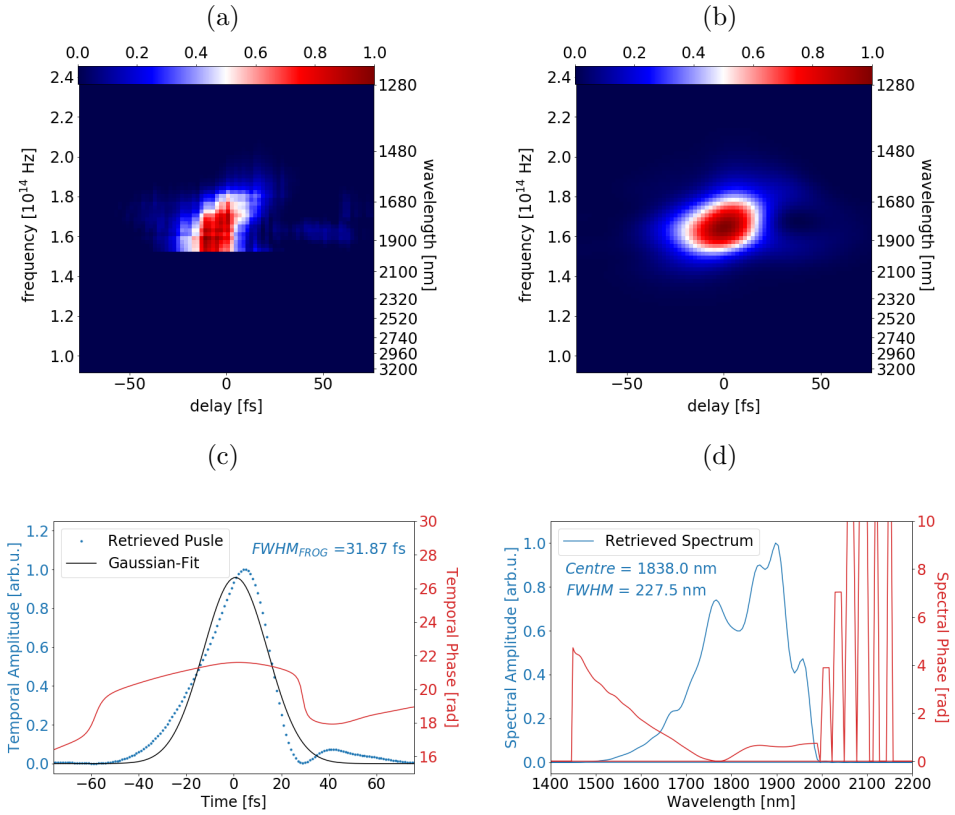

Figure B.4.: **Retrieved FROG characterization of a OPA idler pulse**

(a) experimental trace. (b) retrieved trace. (c) temporal amplitude (blue) and phase (red). (d) spectral amplitude (blue) and phase (red).

For a complete temporal characterization of the laser system, a FROG measurement of a TOPAS idler pulse centered around $\lambda_c = 1838$ nm was additionally carried out. As the idler output was not used for further experiments, the data is presented here in the appendix. The retrieval results are shown in fig.(B.4). Since the idler beam profile is much more inhomogeneous than the signal one, this manifest in a noisy FROG trace (fig.(B.4(a)). Although the retrieval converges to a FROG error of $G_{\text{idler}} = 1.5\%$, the retrieved trace (fig.(B.4(b)) do not match the input one reasonably well. Thus, the resulting temporal and spectral profiles are only partly capable of characterizing the pulse and shall therefore not be discussed further.

C. Atomic Units

The system of atomic units is used in this thesis. They are used often in atomic and molecular physics, as they scale properties to the 'natural' scale of the hydrogen atom. For that purpose, following quantities are set to equal one:

$$e = m_e = \hbar = a_0 = \frac{1}{4\pi\epsilon_0} = 1, \tag{C.1}$$

where e is the elementary charge, m_e the electron mass, $\hbar$ the Planck's reduced constant, a_0 the Bohr radius and $\frac{1}{4\pi\epsilon_0}$ the Coulomb's constant. With the convention in eq.(C.1), a selection of physical quantities is presented in tab.(C) with their corresponding SI values.
Note, that the intensity is not defined as energy per time and area, but is directly linked to the electric field strength $\mathscr{E}_{au}$:

$$I_{au} = \frac{1}{2} c_0 \epsilon_0 \mathscr{E}_{au}^2. \tag{C.2}$$

The quantities in atmoic units, defined in tab.(C), are used in the simulations of chapter (4) due to simplified unit conversion.

quantity (in a.u.)	corresponding SI value
mass	$9.109 \cdot 10^{-31}$ kg
length	0.529 Å
time	0.0242 fs
energy	27.21 eV
electric field strength	$5.142 \cdot 10^{9}$ V/cm
(light) intensity	$3.509 \cdot 10^{16}$ W/cm^2

Table C.1.: Physical quantities defined in atomic units. Data taken from [72]
.

D. Supplementary Material to the Time-Delay Scan Simulations

D.1. Dipole Moments between DES in Helium

states	$2s2p$	$sp_{2,3+}$	$sp_{2,4+}$	$sp_{2,5+}$	$sp_{2,6+}$	$sp_{2,7+}$	$sp_{2,3-}$	$sp_{2,4-}$	$sp_{2,5-}$	$sp_{2,6-}$
$2s^2$	0.1	2	0.01	0.01	0.01	0.01	0.01	0.01	0.01	0.01
$2s3s$	0.1	0.1	1.3	0.01	0.01	0.01	0.01	0.8	0.01	0.01
$2s4s$	0.1	0.1	0.01	0.01	0.01	0.4	0.01	0.01	0.01	0.3
$2s5s$	0.1	0.01	0.01	0.01	0.01	0.01	0.01	0.01	0.01	0.01
$2s6s$	0.1	0.1	1.3	0.01	0.01	0.01	0.01	0.8	0.01	0.01
$2p2p$	2.17	0.82	0.01	0.01	0.01	0.01	0.01	0.01	0.01	0.01
$2p3p$	0.1	0.1	0.01	0.01	0.01	0.4	0.01	0.01	0.01	0.3
$2p4p$	0.1	0.01	0.01	0.01	0.01	0.01	0.01	0.01	0.01	0.01
$2p5p$	0.1	0.1	1.3	0.01	0.01	0.01	0.01	0.8	0.01	0.01
$2p2p$	0.1	2	0.01	0.01	0.01	0.01	0.01	0.01	0.01	0.01
$2p3p$	0.1	0.01	0.01	1	1	0.6	1.5	0.01	0.6	0.4
$2p4p$	0.1	0.1	0.01	0.01	0.01	0.01	0.01	0.01	0.01	0.01

Table D.1.: Dipole moments between DES in helium
For all presented dipole moments d_{ij} the corresponding dipole moment d_{ji} is set to the same value. The dipole moments between two spectroscopically bright and between two spectroscopically dark states are set to equal zero.

D.2. Multi-Photon Ionization Cross Sections

n	1	2	3	4,...
$\sigma^{(n)}$ $[(10^{-22}$ m$^2)^n]$	13	10^5	10^8	0

Table D.2.: For all DES of helium the MPI cross sections $\sigma^{(n)}$ are used depending on the number of photons n necessary for the MPI process

D.3. Time-Delay Scans for the 1240 nm IR pulse

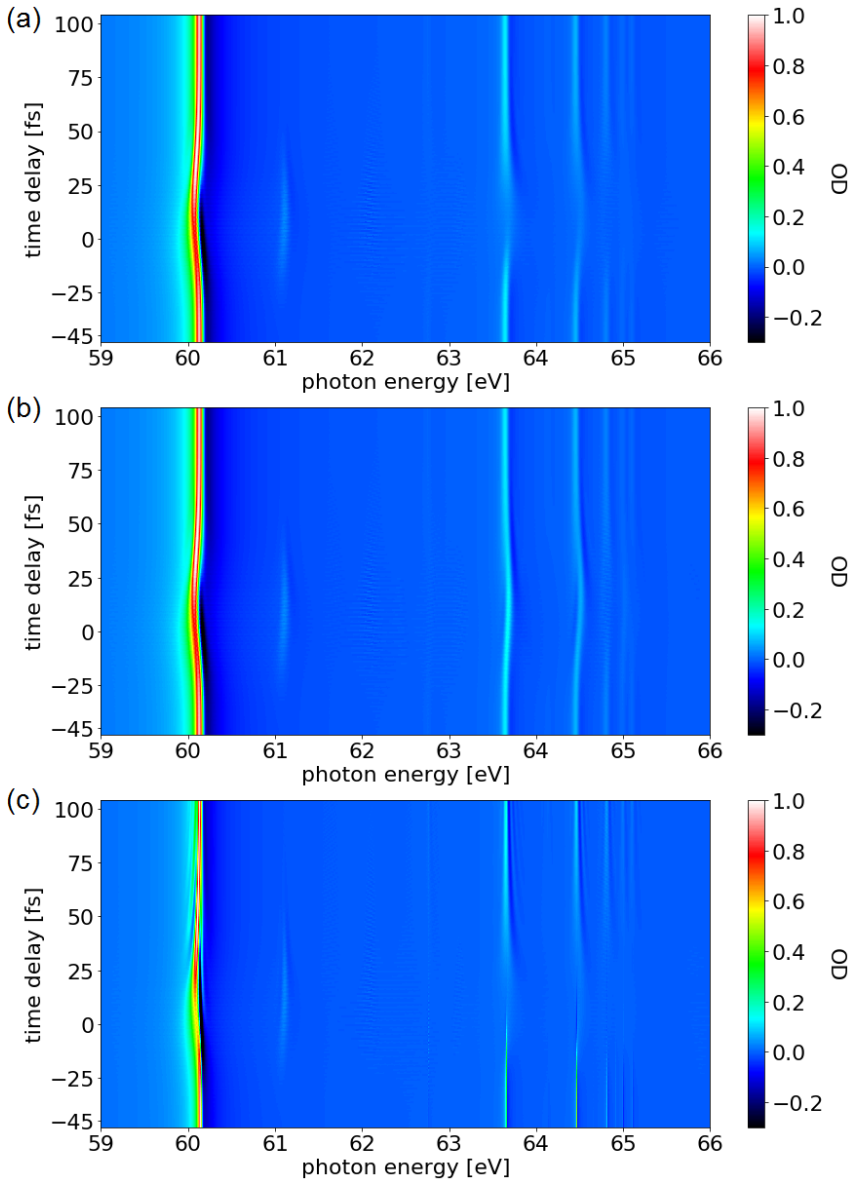

Figure D.1.: **Additional simulated helium TDS for the 1240 nm pulse** The TDS of the spectral OD is shown for different simulations settings. (a) The complete model as shown in fig.(5.5(b2)). (b) The same simulation as in (a), but without the MPI. Hence, the states do not decrease in amplitude around temporal overlap anymore. (c) The same simulation as in (a), but without the additional spectrometer convolution. Thus, the resonances appear less broad and more spectral details are evident.

E. Lists

List of Figures

List of Tables

F. Acknowledgment

Zum Ende dieser Arbeit möchte ich mich gerne bei all denjenigen bedanken, die bei dem Erstellen dieser Arbeit mitgeholfen haben. Mein besonderer Dank geht an:

- **Thomas Pfeifer**, sowohl für die Möglichkeit, in seiner Abteilung diese Arbeit zu erstellen als auch für die stets hilfreichen und motivierenden Unterhaltungen zu jeglichen Fragestellungen meinerseits.
- **Robert Moshammner**, für die Übernahme der Zweitkorrektur dieser Arbeit.
- **Christian Ott**, in dessen Gruppe ich diese Arbeit anfertigen konnte. Danke für die viele Physik, die ich in unseren Gesprächen gelernt habe.
- **Patrick Rupprecht**, für das Betreuen meiner Arbeit. Die Zeit war sowohl intensiv also auch lehrreich und wird mir positiv in Erinnerung bleiben.
- **Alisa Danilenko**, **Yoonsoo Kim** und insbesondere **Lennart Aufleger**, für die erfolgreiche Zeit im Labor und beim Durchführen der Experimente.
- **Thomas Ding**, für die zahlreichen Diskussionen und schönen Unterhaltungen.
- Dem gesamten **X-music**- und **Interatto-team** (neben oben genannten: Marc Rebholz, Maximilian Hartmann, Carina da Costa Castanheira, Gergana Borisiva, Veit Stooß, Martin Laux, Lukas Endres, Paul Birk, Patrick Friebel, Tobias Heldt, Shuyuan Hu). Die Zeit am Insitut und abseits davon bleibt mir sicherlich genauso gut in Erinnerung wie die Arbeit als solche.
- Allen MPIK Technikern und Mitarbeitern, insbesondere **Nikola Molov**. Du bist und bleibst Teil unseres Teams.
- Allen meinen Freunden und Bekannten. Es gab, gibt und wird weiterhin viel zu erleben geben, manchmal trotz und manchmal gerade wegen solcher langen Arbeits- und Pausenphasen
- Und zu guter Letzt meinen **Eltern**. Danke für Eure stetige Unterstützung.

Erklärung:

Ich versichere, dass ich diese Arbeit selbstständig verfasst habe und keine anderen als die angegebenen Quellen und Hilfsmittel benutzt habe.

Heidelberg, den 20.12.2018 .....

(Alexander Magunia)